ABSTRACT

Title of Dissertation: ELECTRON BEAM INDUCED CURRENT IN WIDE BANDGAP SEMICONDUCTORS USING SCANNING TRANSMISSION ELECTRON MICROSCOPY

Zoey Warecki, Doctor of Philosophy, 2020

Dissertation Directed by: Associate Professor John Cumings
Department of Materials Science and Engineering

Wide bandgap semiconductors are those with a larger bandgap than silicon; this property allows them to operate at higher voltages, higher driving frequencies, and higher operating temperatures. Gallium nitride (GaN) in particular is attractive for its high critical electric field and thus high breakdown strength allowing for the design of a thinner drift region for a given blocking voltage. It is for these same reasons that GaN is also more radiation resistant than Si, and thus is attractive for satellite or space applications. With the recent commercial availability of free standing GaN substrates, there are many fundamental properties of GaN-on-GaN devices that are still not understood. One of the main characterization techniques used to classify GaN device quality is the measurement of the minority carrier diffusion length via electron beam induced current (EBIC). One of the main limitations of the traditional scanning electron microscopy (SEM) EBIC technique is due to the size of the electron beam/specimen interaction volume at > 5 kV, as well as large collection losses due to carrier recombination at the surface at < 5 kV.

This dissertation addresses the previous issues of SEM EBIC with a non-traditional bulk scanning transmission electron microscopy (STEM) EBIC technique which allows for high resolution measurements of the hole diffusion length in n-GaN/Ni Schottky diodes. A reproducible, non-invasive bulk STEM sample preparation technique for n-GaN/Ni Schottky diodes is developed for the use of collecting bulk STEM EBIC micrographs. Despite the large interaction volume in this system at 100-200 kV, quantitative bulk STEM EBIC imaging is possible due to the small STEM probe beam diameter and sustained collimation of the incident electron beam in the sample. Using a combination of experimental bulk STEM EBIC measurements, Monte Carlo simulations, and numerical simulations, a hole diffusion length of 250 $\pm$ 15 nm was determined for homoepitaxial n-GaN samples with a threading dislocation of approximately 10^6 cm^{-2}. In-situ reverse biasing measurements allowed for the measurement of depletion region growth with increasing bias. Furthermore, accumulated electron irradiation damage was studied at 200 kV. An accumulated dose of 24 x 10^{16} electrons cm^{-2} caused a 35 % reduction in the minority carrier diffusion length which is attributed to knock-on damage of the N sublattice.

Additionally, the design and development of a custom STEM holder for in-situ liquid cell electrochemical microscopy is discussed.

ELECTRON BEAM INDUCED CURRENT IN WIDE BANDGAP SEMICONDUCTORS USING SCANNING TRANSMISSION ELECTRON MICROSCOPY

by

Zoey Warecki

Dissertation submitted to the Faculty of the Graduate School of the
University of Maryland, College Park in partial fulfillment
of the requirements for the degree of
Doctor of Philosophy
2020

Advisory Committee:
Associate Professor John Cumings, *Chair/Advisor*
Professor Chunsheng Wang, *Deans Representative*
Professor Lourdes Salamanca-Riba
Associate Professor Yifei Mo
Dr. Katherine Jungjohann

© Copyright by
Zoey Warecki
2020

Dedication

To my mom and dad, Erika and Jack Warecki. Thank you for everything.

Acknowledgments

This dissertation is based upon work supported by the National Science Foundation Graduate Research Fellowship Program under Grant No. DGE 1840340. I would like to acknowledge support from the Nanostructures for Electrical Energy Storage (NEES), an Energy Frontier Research Center funded by the U.S. Department of Energy, Office of Science, and support from NIST Grant No. 70NANB15H218. The work at SNL was funded in part by the Advanced Research Projects Agency – Energy (ARPA-E), U.S. Department of Energy, under the PNDIODES program, award 16-CJ000-10-04. Sandia National Laboratories is a multimission laboratory managed and operated by the National Technology and Engineering Solutions of Sandia, LLC., a wholly owned subsidiary of Honeywell International, Inc., for the U.S. Department of Energy's National Nuclear Security Administration under Contract DE-NA-0003525.

First I would like to thank my advisor, John Cumings for being a great teacher, mentor, and friend. Your support, both intellectually and beyond, have help me immeasurably. I would also like to acknowledge the Cumings Lab, including Joy Chao, Kyle Sendigoski, Kayla Calloway, Dr. Jeremy Ticey, Dr. Hanna Nilsson, and Dr. Jasper Drisko. I'd especially like to thank my committee members: Professor Salamanca-Riba, Professor Chunsheng Wang, Associate Professor Yifei Mo, and Dr.

Katherine Jungjohann. I'd also like to acknowledge and thank Alec Talin, Andrew Armstrong, Kimberlee C. Collins, and Andrew Allerman from Sandia National Laboratory (CA and NM) for providing GaN samples, expertise, and advice. I would like to acknowledge Katherine Jungjohann and Subrahmanyam Goriparti from Sandia National Laboratory, NM for their collaboration on the electrochemical liquid cell work and Vladimir Oleshko, NIST, for his help with STEM and CASINO.

I'd like to thank the many professors and staff members in the Materials Science & Enginnering Department and at the UMD Nanocenter. I'd like to thank Dr. Wen-An Chiou, Dr. Sz-Chian Liu, and Dr. Jiancun Rao in the AIMLab as well as John Abrahams, Thomas Loughran, John Hummel, and Mark Lecates in the FabLab. I'd also like to thank the TEM Joint Research Group, including Professor Taylor Woehl, Mei Wang, Umesha Dissanayake, Dr. Xiaoxaio Ge, Madeline Morales, and Dr. Hua Xie. I'd like to give a special shout-out to Christopher Klingshirn for being my sounding board many times through out the years.

I'd also like to give a huge thank you to Bruce Rowley in the UMD Physics Machine Shop and to Jack Touart in the Electronics Group for helping me build the custom holder. I'd also like to thank Loan Truong, who helped me finish the holder. Thank you to everyone in NEES II, but especially to Dr. Elizabeth Lathrop and to Dr. Emily Sahadeo.

I want to thank my friends and family who have supported me through these years. Thank you to my mom and dad, Erika and Jack Warecki, and to my siblings Mickey, Brian, and Jane. Thank you to my grandparents, Edward and Joyce Sobanski, Teresa and John Olszower. Thank you to the rest of my family, especially

John and Erin Sobanski and Anthony, Lia, and Oscar. Thank you to Evelyn Sobanski, Jessika Sobanski, Jade Dadiz, and Athena and Luis Valdovinos. Thank you to my uncle Rich Olszower. Thank you to my UMD friends, including Dr. Miriam Hiebert, Dr. Lisa Krayer, Francesca Roth, Elizabeth Robinson, Charlee Bezilla, Allie Le Moine, Brianna Montoya, and many more I have not mentioned. Thank you to Samantha Andujar, Melinda Knebel, Mary-Anne Nelligan, Lynda Hyunh, Hongdao Ngyuen, Dana Molloy, and Benjamin Ladney. A huge thank you to everyone in the Towson University Physics Department, especially Professor Rajeswari Kolagani, who supported me and encouraged me to pursue my PhD. Thank you to my high school mathematics teachers Sue Cuzzo and Hal Holt and my physics teacher Cristina Brazelli.

A huge thank you to my best friend at UMD, Naila Al Hasan - we did it Naila! And lastly, thank you to my partner, Justin Baumgartner, and to our bearded dragon, Stitch. I would not be here without you both.

Thank you to the countless others I have not mentioned here. The majority of this research was performed at the University of Maryland, College Park in the Materials Science and Engineering Department and the NanoCenter Facilities. I would like to acknowledge that my research at UMD was conducted on land which originally belonged to the Piscataway People. This land was stolen from the Piscataway People by European colonists in the seventeenth century. I believe the first step in making reparations to the Piscataway people is to acknowledge the history of this campus.

Table of Contents

Abstract ii

Dedication ii

Acknowledgements iii

Table of Contents vi

List of Tables viii

List of Figures ix

List of Abbreviations xi

Chapter 1: Introduction 1
- 1.1 Introduction to gallium nitride . . . 2
  - 1.1.1 Wide bandgap semiconductors . . . 2
  - 1.1.2 Materials Properties of GaN . . . 8
  - 1.1.3 Goal of this work . . . 9
- 1.2 Lithium Ion Batteries . . . 10
  - 1.2.1 LIB Anode Materials . . . 12
  - 1.2.2 Nanostructured Sn Anodes . . . 13
  - 1.2.3 Goal of this work . . . 15
- 1.3 Introduction to Experimental Methodologies . . . 16
  - 1.3.1 TEM, STEM and SEM . . . 16
  - 1.3.2 In-situ Holders . . . 20
  - 1.3.3 Electron Beam Induced Current . . . 23
  - 1.3.4 Quantitative EBIC Resolution . . . 27
  - 1.3.5 CASINO . . . 30

Chapter 2: Bulk STEM EBIC 35
- 2.1 Preliminary Hypothesis . . . 35
- 2.2 Experimental Methods . . . 37
  - 2.2.1 Sample Preparation . . . 37
  - 2.2.2 EBIC Collection . . . 39
- 2.3 Data Processing . . . 42
  - 2.3.1 LM STEM Magnification Calibration . . . 42

2.3.2 Image Resolution Estimate 44
2.3.3 EBIC Linescan Selection 45
2.3.4 EBIC Current Calibration 47
2.4 Long Range Background Subtraction 49
2.4.1 Electron Penetration Depth Theory 52
2.4.2 CASINO Simulations of Long Range Scattering in GaN 54
2.5 Modeling Bulk STEM EBIC 56
2.5.1 Diffusion Equation Solution 57
2.5.2 Generation Volume Equation 58
2.5.3 Integration Limits 65
2.5.4 Numerical Simulation Results 66
2.6 Experimental bulk STEM EBIC results 72

Chapter 3: In-situ Bulk EBIC 74
3.1 Electron Beam Irradiation of GaN 74
3.1.1 Evidence of electron irradiation damage to GaN 74
3.1.2 Beam Current Measurements 76
3.1.3 Electron Irradiation Data Collection 79
3.1.4 Electron Damage Results 82
3.2 In-situ Reverse Biasing 85
3.2.1 Data Analysis and Results 87
3.3 Thinned GaN EBIC 92
3.3.1 Data Analysis and Results 94

Chapter 4: Custom STEM Holder for In-situ Liquid Cell Electrochemistry 97
4.1 Liquid Cell Electron Microscopy 97
4.1.1 CINT Electrochemical Liquid Cells 99
4.2 UMD Custom In-situ Holder 101

Chapter 5: Conclusions and Future Work 108
5.1 Bulk STEM EBIC 108
5.2 Custom In-situ Holder 110

Appendix A: Bulk STEM Sample Preparation S.O.P. 112

Appendix B: Bulk STEM EBIC Matlab Code 118

Appendix C: Custom Holder CAD Drawings 121

Bibliography 138

List of Tables

1.1 Wide bandgap table . . . 3
1.2 LIB Anode Materials . . . 13

2.1 Long Range Background . . . 51
2.2 Minority Carrier Diffusion Length Results . . . 73

List of Figures

1.1 Wide bandgap semiconductors . . . 5
1.2 Radiation hardness of WBG . . . 7
1.3 Lithium Ion Batteries . . . 11
1.4 TEM/STEM Block Diagram . . . 18
1.5 Nanofactory holder . . . 22
1.6 Experimental EBIC . . . 25
1.7 EBIC planar geometry . . . 27
1.8 CASINO Electron Scattering Trajectories . . . 33
1.9 CASINO Electron Energy Distributions . . . 34

2.1 Size of Interaction Volumes . . . 36
2.2 Bulk STEM EBIC Setup . . . 38
2.3 Ni/GaN Characteristic EBIC Profile . . . 41
2.4 JEOL 2100 FEG LM Calibration . . . 43
2.5 JEOL 2100 FEG LM Resolution Estimate . . . 45
2.6 EBIC Linescan Selection . . . 46
2.7 EBIC Current Calibration . . . 48
2.8 EBIC Background Subtraction . . . 50
2.9 Penetration Depth of High Energy Electrons . . . 53
2.10 Surface Radius Distribution of BSE . . . 55
2.11 CASINO Beam Spread . . . 60
2.12 CASINO Electron Beam Spread 200 kV . . . 62
2.13 CASINO Beam Spread 100 kV . . . 63
2.14 Beam Spread Approximation . . . 64
2.15 M-S Energy band diagram . . . 66
2.16 Numerical Simulation Methods . . . 67
2.17 Simualted EBIC data . . . 69
2.18 Effect of changing L_p and α . . . 70
2.19 Effect of changing d_beam and W_{dep} . . . 71
2.20 Experimental EBIC linescan with fit . . . 73

3.1 Evidence for beam damage . . . 75
3.2 STEM Beam Current Measurements . . . 77
3.3 EBIC Micrographs of Accumulated Damage . . . 80
3.4 Beam Damage . . . 81
3.5 Beam Damage Results . . . 84

3.6 Ni/GaN Junction under reverse bias 86
3.7 Reverse Biasing at 100 kV 88
3.8 EBIC Linescans of Reverse Biasing at 100 kV 89
3.9 Reverse Biasing at 200 kV 90
3.10 EBIC Linescans of Reverse Biasing at 200 kV 91
3.11 Example of thin STEM EBIC in p-type Si 93
3.12 Thinned GaN EBIC Schematic 95
3.13 Thinned GaN STEM and Specimen Current Micrographs 96

4.1 Liquid Cell Microscopy 98
4.2 CINT Electrochemical Discovery Platform 100
4.3 Custom Holder Exploded View 102
4.4 Front of holder assembly 104
4.5 Holder 106

5.1 Lithiation of Sn Anodes 111

A.1 Sample Prep Images 117

Frequently used Abbreviations and Symbols

α	Beam spread coefficient
BSE	Back scattered electrons
E_b	Electron beam energy (kV)
E_d	Atomic displacement energy (eV)
ϵ_0	Permitivitty of space (F/cm)
EBIC	Electron beam induced current
EHP	Electron hole pair
FSE	Forward scattered electrons
g	Generation volume of carriers
HVPE	Hydride vapor phase epitaxy
d_{beam}	STEM probe beam diameter
DF	Dark Field STEM
I_{EBIC}	Collected EBIC current
IV	Interaction volume
IV Curve	Current - Voltage Curve
LIB	Lithium Ion Battery
LM	Low magnification
L_p	Minority carrier (hole) diffusion length
L_{LR}	Long range scattering
N_D	Dopant concentration
Δp	Minority carrier (hole) distribution
$\Phi_{M,S}$	Work function (metal, semiconductor)
q	Charge of an electron (C)
R	Penetration depth of electrons
SE	Secondary electrons
SEM	Scanning electron microscope
SR	Short Range Scattering
STEM	Scanning transmission electron microscope
τ_p	Minority carrier (hole) lifetime
TEM	Transmission electron microscope
TDD	Threading dislocation density
V_{bi}	Built-in potential
WBG	Wide bandgap
W_{dep}	Depletion region (space charge region)

Chapter 1: Introduction

This dissertation will explore in-situ electron microscopy techniques for studying wide bandgap semiconductors and lithium ion battery electrodes. The first portion of this work (Chapters 2) investigates fundamental properties of GaN for power electronics and radiation-hardened devices. The electronic properties of homoepitaxial n-type GaN/Ni Schottky diodes were studied using a high energy electron beam induced current (EBIC) technique, specifically measuring the minority carrier diffusion length of this material. Monte Carlo simulations of electron trajectories in GaN were used to build a numerical simulation model of the collected currents. The usefulness of this technique is demonstrated in Chapter 3, which investigates the collected current dependence on electron beam irradiation as well as applied biasing. Chapter 3 also includes preliminary work on the application of STEM EBIC on thinned GaN diodes. The second portion of this work (Chapter 4) focuses on the design and development of a custom TEM/STEM holder to be used for in-situ liquid cell microscopy studies of lithium ion battery anodes. Chapter 5 summaries the result and discusses potential avenues for future research.

1.1 Introduction to gallium nitride

1.1.1 Wide bandgap semiconductors

We are at a pivotal moment in human history – advances in medicine, technology, industrialization, and globalization have allowed us to live longer and more connected lives than ever before. However, many of these same technological advances have come or will come at a great environmental and human costs. Decisions made right now will affect our future in profound ways. For example, the Intergovernmental Panel on Climate Change (ICPP) has targeted a $1.5 - 2^{\circ}$ C rise in the average global temperature as an acceptable level of warming by 2100. [1] This 2° C rise, which itself will have serious consequences on agriculture, coastal regions, and extreme weather events, is going to be difficult to meet. These serious challenges must be met with innovative solutions focused on renewable energy sources, practical energy storage, and efficient delivery and consumption of energy.

Power electronics is the branch of engineering which refers to the conversion, delivery, and transportation of energy. For a long time, silicon-based devices have been the work-horse of these integrated circuits, making up about 87% of the power electronics devices market. [2] While Si will likely remain the dominant material in the semiconductor market, there are other electronic materials which offer substantial benefits over Si. For example, GaAs has a slightly larger bandgap and a much higher electron mobility than Si, and has been commonly used in radio frequency (RF) applications. However, worldwide energy and power demands have driven the

Property	Si	GaAs	GaN	4H-SiC
Bandgap, E_g (eV)	1.1	1.4	3.4	3.3
Critical electric field, $\xi_c(MV/cm)$	0.3	0.4	5.0	3.0
Electron Mobility, $\mu_e(cm^2/Vs)$	1400	8500	2000	1000
Dielectric constant*, ε	11.7	12.9/10.9	8.9/5.4	9.6/6.5
Thermal conductivity (W/cmK)	1.5	0.5	2.0	3

Table 1.1: Electronic Properties of GaN compared to Si, SiC, and GaAs. Properties are reported for room temperature. Data collected from [3, 4]. *Dielectric constant for static/high frequency operation.

need for power electronics beyond Si or GaAs to wide bandgap (WBG) materials, such as gallium nitride (GaN) and silicon carbide (SiC). A comparison of relevant electronic properties of these materials is shown in Table 1.1.

WBG semiconductors can handle higher operating voltages, higher driving frequencies, more efficient AC-to-DC and DC-to-AC conversion, and higher operating temperatures. For example, the naturally wider bandgaps of these materials makes them less susceptible to thermal runaway. This can be seen immediately if one considers the intrinsic carrier (i.e. thermal carrier) concentration of a semiconductor, given by [5]:

$$n_i = \sqrt{N_C N_V} e^{-E_g/2kT} \tag{1.1}$$

where N_C and N_V are the density of states in the conduction and valence band, respectively. Device engineering and operation typically depends on the ratio of the dopant concentration to this intrinsic concentration. For example, the intrinsic concentration of electrons in n-type Si is typically 10^{10} cm^{-3} at room temperature. [6] This is negligible when compared to even the lightest doped region of a silicon device, around 10^{14} - 10^{17} atoms cm^{-3}. [7] However, if the device is operating in a

high temperature environment, around 300° C, the temperature rise can cause the number of intrinsic carriers to rise to the level of dopants, thus interrupting the expected behavior of the device. This may lead to, as an example, improper switching of the device. However, this can be mitigated by the use of WBG semiconductors, whose wider bandgap gives them significantly lower intrinsic carrier concentration than Si and who do not run into high temperature difficulties until much higher temperatures, beyond 600° C. [7]

Another important figure of merit for WBG semiconductors is the critical electric field, ξ_c, which is the upper limit that a semiconductor can withstand before undergoing avalanche breakdown. Avalanche breakdown occurs when the electric field is sufficiently high enough that excited carriers have enough energy to excite other carriers, which can excite more carriers, leading to "uncontrolled multiplication." [5] A high critical field and thus high breakdown strength allows for the design of a thinner drift region for a given blocking voltage. Reducing the drift region thickness in turn reduces the specific ON state resistances and results in lower capacitances. This reduces the associated switching losses which then allows for higher frequency switching operation. [8] A comparison of specific on-resistances vs critical electric fields for real devices is given in Figure 1.1.

One of the relevant applications for WBG is in the field of radiation hardened devices. Radiation hardened devices are those which can withstand a larger flux of radiation commonly found in space environments, nuclear reactors, or high-energy particle colliders. [10] Depending on the location of a satellite or spacecraft, the internal electronics can be subject to any combination of ionizing and non-ionizing

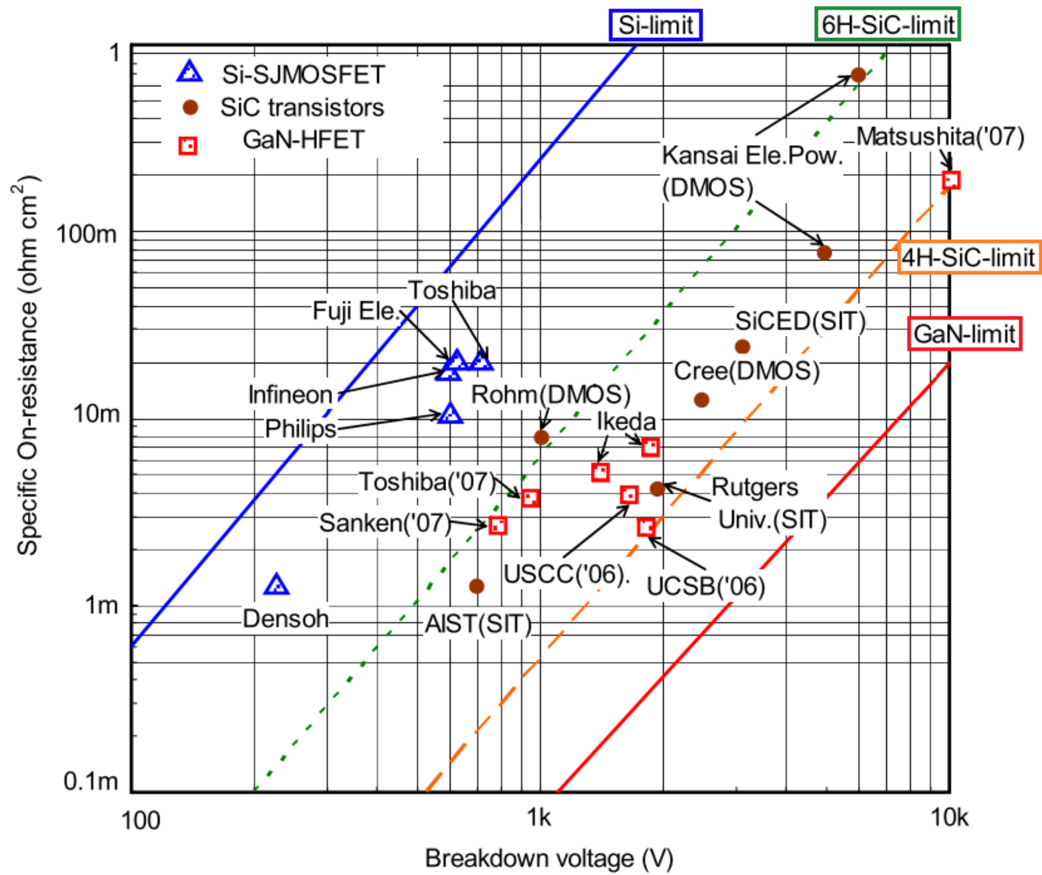

Figure 1.1: Comparison of wide bandgap semiconductors. Adapted from [9].

radiation such as electrons, protons, neutrons, gamma rays, heavy ions, etc. [11] These electronics, which are critical to powering, navigating, and communicating with the spacecraft, are at an even higher risk for off-planet missions. Since radiation hardness is a result of strong atomic bonding, the unit cell size of a crystal is a good predictor of a crystals resistance to knock-on damage. It has been empirically observed that atomic displacement energy, E_d, is inversely proportional to the unit cell, as shown in Figure 1.2. Fortunately, WBG semiconductors have compact crystal structures, and as such have correspondingly higher atomic displacement energy. GaN specifically has been gaining attention for its potential radiation hardness. [12, 13]

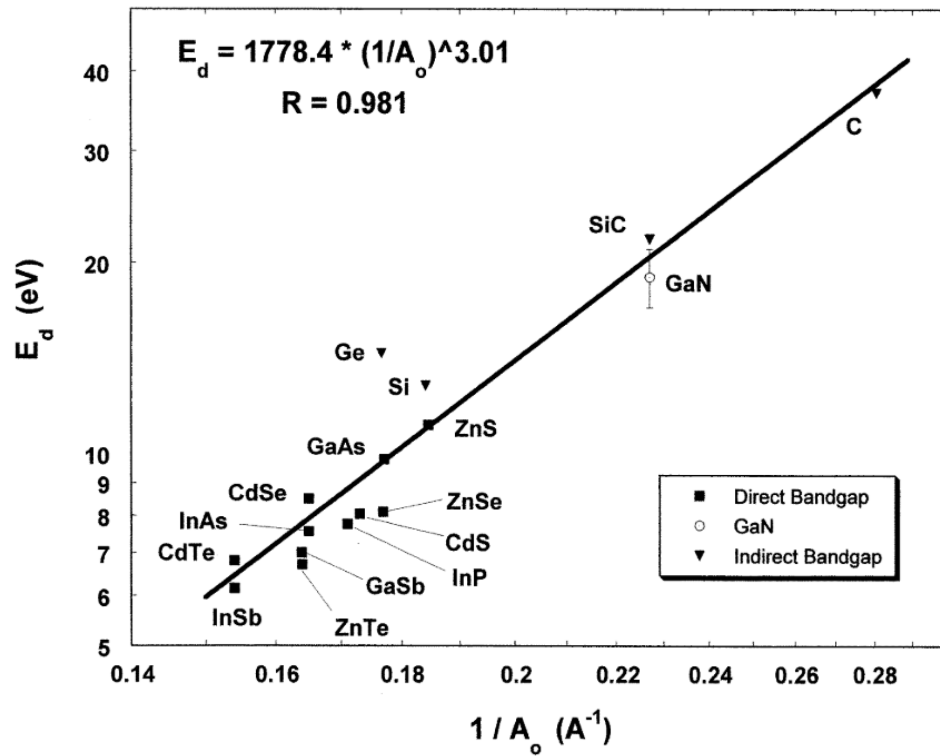

Figure 1.2: Empirical measurements of the atomic displacement energy, E_d as a function of the decreasing lattice constant. Adapted from [14].

1.1.2 Materials Properties of GaN

Gallium nitride (GaN) is most famous for its part in the light emitting diode (LED) revolution, specifically the invention of blue LEDs. This invention led to the ability to produce white LEDs with a higher luminous flux which led to the 2014 Nobel Prize in Physics being awarded to Akasaki, Amano, and Nakamura. Besides LEDS, GaN is already being used in a variety of other applications, such as laser diodes, solar cells, and photodetectors.

In the past, the lack of native substrates required heteroepitaxial growth of GaN on sapphire, Si, SiC, and AlN, which have mismatches in lattice constant and thermal expansion coefficient. [4] For example, growing GaN-on-Si results in high threading dislocation densities (TDD) of $10^8 - 10^{10}$ cm^{-2}. [15] The main advantage of growing on Si is the cheaper cost of production, however, the dislocations degrade device performance by acting as traps and recombination centers, leading to leakage current and breakdown. [16] More recently, high pressure, ammonalthermal, and hydride vapor phase epitaxy (HVPE) growth methods have been used to grow bulk, free-standing GaN as a suitable substrate for epitaxial growth. HVPE grown free-standing GaN has a higher TDD ($10^6 - 10^7$ cm^{-2}) than high pressure or ammonalthermal grown ($10^2 - 10^4$ cm^{-2}), but HVPE is more attractive due to its wider availability, faster growth rates, and larger and more uniform wafer size. [17]

The recent commercial availability of these GaN-on-GaN devices has led to an increased interest in GaN for power electronics applications, for the reasons discussed earlier. One application is in high electron mobility transistors (HEMT),

which take advantage of the two dimensional electron gas (2DEG) in GaN. Other promising devices are GaN-on-GaN Schottky power diodes, [18, 19, 20, 21] which are able to withstand high voltages before undergoing breakdown.

1.1.3 Goal of this work

One of the most common ways to characterize n-type GaN is by measuring the minority carrier (hole) diffusion length, $L_p \equiv (D_p \tau_p)^{1/2}$. [22] Physically, the minority carrier diffusion length represents the average distance a minority carrier can diffuse into a semiconductor of majority carriers before being annihilated. As such, it is heavily influenced by the type and quality of the semiconductors, which makes it very useful to compare the differences between epilayers grown by various methods.

As Yakimov noted, [23] the methods of measuring L_p in n-GaN, mainly SEM cathodoluminescence (CL) and SEM electron beam induced current (EBIC), are not always consistent. This is mainly due to the fact that GaN has a much smaller minority carrier diffusion length than Si, and therefore detailed analysis must be performed to correctly interpret SEM CL or EBIC (see Section 1.3.4). The goal of this work is to develop an alternative to SEM CL and EBIC by measuring L_p of bulk n-GaN using a STEM EBIC technique. Not only does this technique have signficant advantages over SEM CL and EBIC, it is also used to explore the effects of electron radiation damage to GaN.

1.2 Lithium Ion Batteries

Efficient energy storage is a critical aspect of materials development for a sustainable future, especially since many renewable energy sources such as solar and wind are intermittent and cannot supply constant energy to the grid. High-energy density, long lasting, rechargeable lithium ion batteries (LIB) are currently used for device powering and for small-scale storage applications such as electric vehicles. A battery has three main components: an negative electrode referred to as the *anode*, a positive electrode referred to as the *cathode*, and an *electrolyte* (for our purposes is considered to be an ionic salt dissolved in a liquid aprotic solvent). Other important components in the battery are the current collectors, separator, and other packaging components that influence the performance of the battery.

The commercial boom of rechargeable, or secondary, LIB was due to the application of Li^+ intercalation chemistry by Whittingham, [25] followed by the development of lithium cobalt oxide cathodes by Goodenough *et al.* [26] and the deveopment of graphite anodes by Akira Yoshino of Asahi Kasei Corporation in Tokyo. These three scientists were awarded the 2019 Nobel Prize in Chemistry for their significant contributions. Intercalation chemistry refers to the reversible inclusion or insertion of the ion into compounds with layered structures. In LIB, for example, during charging, an electron is transferred from the cathode side to the anode via an external circuit. This causes the Li^+ in the lithium cobalt oxide cathode to diffuse through the ion conducting electrolyte and intercalate into the layers of the graphite anode, thus converting electricity into stored chemical energy.

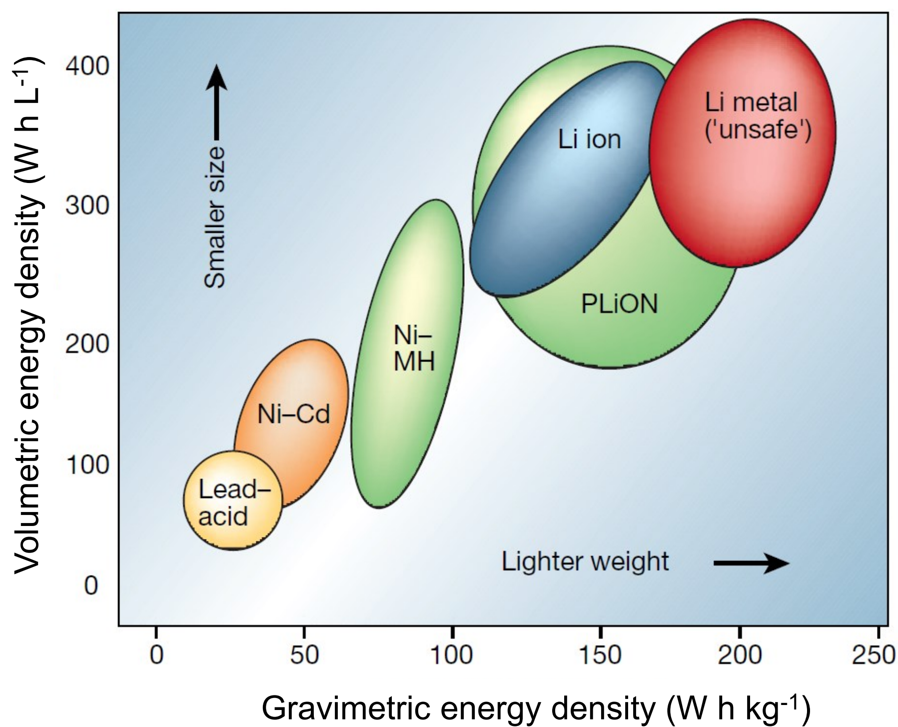

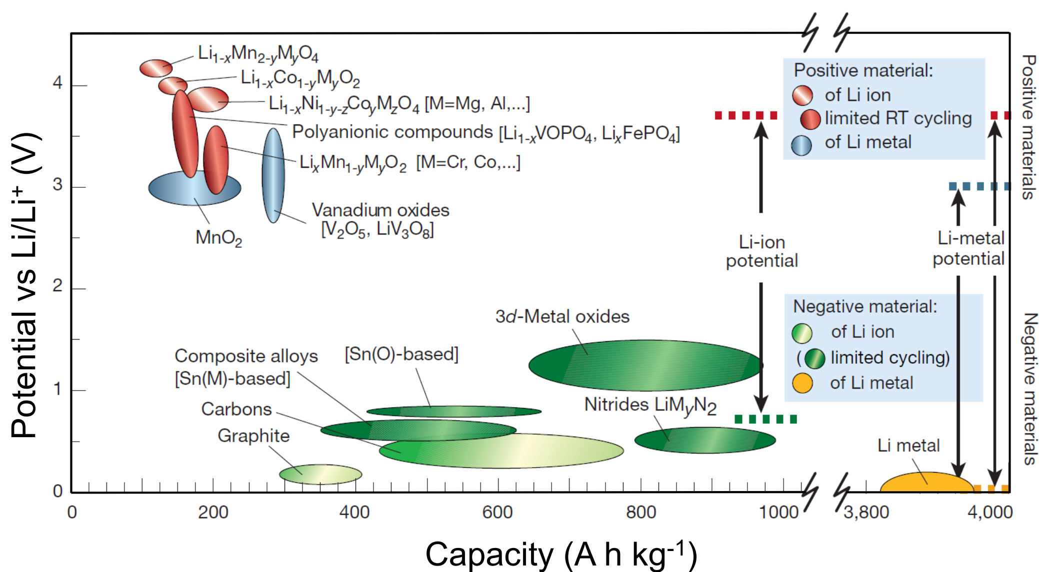

Figure 1.3: A representation of (a) the energy densities of different battery chemistries and (b) the potentials and capacities of different LIB electrode materials. Adapted from [24].

During discharge, the Li^+ flow in the opposite direction, causing electrons to flow from the anode to the cathode through the external circuit, resulting in a current which can be used to power electronic devices. The advantage of using Li^+ is that it is highly electropositive (–3.04 V versus standard hydrogen electrode), it is very small and also very lightweight. [24] All of these factors cause LIB to have the highest gravimetric and volumetric energy densities, as shown in Figure 1.3a.

1.2.1 LIB Anode Materials

While graphite is the most successful LIB anode, it has one of the lowest theoretical gravimetric capacities (see Figure 1.3b), which has been achieved. [27] Furthermore, the rate of Li diffusion into graphite is slow ($10^{-9} - 10^{-7}$ cm^2 s^{-1}), [28], resulting in low power density. Pure Li metal anodes have the highest theoretical capacity and are considered to be the holy grail of LIB, with ongoing efforts to create working anodes. [29] The main limitation for Li metal anodes is the harmful dendrite formation which leads to short circuiting. In the route towards higher capacity and higher power density anodes, other non-intercalation processes are being considered, such as alloying and conversion anodes. [30] Table 1.2 shows the theoretical gravimetric capacities of relevant LIB anode materials. The benefit of alloying anodes, such as Si and Sn, is that the atomic structure of the anode host does not constrain the reaction, as is the case with intercalation materials. [31] Unfortunately, the very same property that enables such high theoretical capacities is the same one that results in poor cycling. This is because the materials undergo

Material	Type	Theoretical gravimetric capacity
C (graphite)	Intercalation	372 mAh/g
Li metal		3860
Si	Alloying	4200
Sn	Alloying	994

Table 1.2: Storage capacities for LIB anodes. [34]

large volume expansion, bond breaking and dramatic structural changes during lithiation, and, upon subsequent removal of Li, they crack and pulverize. [32] They can form inactive lithium oxide layers as well as disconnect from the current collector. To limit these degradation mechanisms, one strategy is to fabricate nanostructured anodes to reduce the effect of mechanical stress as well as increase the surface to volume ratio. [33, 34]

1.2.2 Nanostructured Sn Anodes

In order to realize the success of nanostructured alloying anodes, we must understand the degradation mechanisms and how to best mitigate them. [35] There are a variety of strategies being explored for nanostructure anodes including: architecture engineering, [36, 37] chemical functionalization, [38] artificial SEI (solid electrolyte interphase) control [39] or other coatings. [40] Many of these solutions have been pursued for Si anodes, however, strategies on Sn anodes are also needed. One of the benefits of Sn alloying anodes is that Sn is a relatively large and heavy atom, and as such has high Z contrast in the TEM/STEM. This makes Sn an attractive material for in-situ TEM/STEM studies on alloying anodes. The first in-situ TEM lithiation studies were by Huang *et al.* on SnO_2 nanowires, [41, 42] which

showed a total volume expansion of the nanowire under lithiation of 240%. There are also efforts to explore Sn and SnO_2 for sodium ion batteries. [43, 44] Early in situ TEM studies were done on sodium insertion/extraction in Sn nanoparticles [45] followed by SnO_2 nanocrystals [46] and SnO_2 graphene nanocomposites [47]. We are interested in the *lithiation* of Sn, which has the reversible reaction given by:

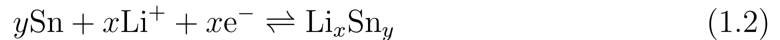

$$y\mathrm{Sn} + x\mathrm{Li}^+ + x\mathrm{e}^- \rightleftharpoons \mathrm{Li}_x\mathrm{Sn}_y \tag{1.2}$$

If there is a SnO_2 layer present, it will first have an irreversible Li_2O lithiation reaction, followed by the reversible Sn-Li alloying reaction. [48] Crystalline Sn can be fully reformed upon delithiation, [49] however, as mentioned earlier, can suffer from the same volume expansion and subsequent pulverization.

One study by Wang *et al.* observed the in-situ lithiation of Sn nanoparticles. [50] They reported that the structural evolution of Sn nanoparticles was highly dependent on the particle size, with micron size particles experiencing large volume expansion and cracking during lithiation. They hypothesized that during delithiation, the fast dealloying rate induces a large concentration gradient of lithium as well as a high stress/strain which can induce cracking and facilitate void formation in dealloyed Sn anodes. A different study by Li *et al.* on Sn nanowires found that delithiation was limited not by the lithium diffusion rate but rather by the interfacial conversion reaction rate. [51] However, the potential advantages of nanowires are still unclear, as Janish *et al.* observed a reversible lithiation reaction in some nanoneedles but an irreversible amorphous Li-Sn compound formation in others.

[52] They hypothesized that the orientation and directionality of the Sn nanowire influenced its degradation, or that perhaps these differences could be attributed to poor electrical/chemical contact with the nanowires. In all of these previously mentioned studies, the TEM observations were done in a "dry" cell, leading one to ask what the degradation mechanisms are in the liquid electrolyte environment.

1.2.3 Goal of this work

The goal of this work is to develop an in-situ holder for the JEOL 2100 FEG which is compatible with the Center for Integrated Nanotechnologies (CINT) Electrochemical-Cell (EC) discovery platform [53]. The EC discovery platform is a sealed liquid cell allowing for advanced in-situ studies inside the vacuum environment of the TEM [54], discussed more in Chapter 4. The holder and EC platform will enable future studies on the effect of cycling Sn nanoparticles under realistic battery conditions and at slightly elevated temperatures. We are interested in learning if the reaction kinetics significantly increase at elevated temperatures and what effect this will have on the electrode structure, alloying process, and cycle reversibility [55].

1.3 Introduction to Experimental Methodologies

1.3.1 TEM, STEM and SEM

The transmission electron microscope (TEM) was first built in 1928 by Max Knoll and Ernst Ruska. Because this instrument became such an important tool for scientists, Ernst Ruska was awarded part of the 1986 Nobel Prize in Physics, the other part went to Gerd Binnig and Heinrich Rohrer for their design of the scanning tunneling microscope. The TEM uses electrons to magnify objects in a similar way to a compound light microscope. In both microscopes, the specimen needs to be thin enough to allow for the transmission of the probing radiation and the magnified image is a result of the interactions between the light and the specimen. (For a short educational video about the TEM starring Joy Chao and the author, see [56].)

The most obvious benefit of the TEM over conventional light microscopes is the increased resolution. The resolution, δ, is defined as the limit at which two separate points are distinguishable and, using the Rayleigh criterion, is a function of the wavelength of the light, $\delta \approx 1.22\lambda$. [57] For electrons, the wavelength depends on their kinetic energy, which is determined by the accelerating voltage of the microscope, with higher accelerating voltages having better resolution. Practically however, this resolution is limited by the electromagnetic lenses used to focus the electrons; effects such as spherical aberration, parasitic aberration, and voltage instability decrease the observed resolution. [58] Generally, TEMs are operated in the accelerating voltage range of 100 - 300 kV. The primary instrument used in this

research was a JEOL JEM 2100 FEG microscope, at both 100 and 200 kV. The field emission gun (FEG) is a tungsten cold emitter that provides a more coherent, higher current density (brighter), and more stable electron source than the older, LaB_6 thermionic emitter.

In traditional TEM, the specimen is illuminated with a parallel beam of electrons and the magnified image is projected onto a fluorescent screen or a charged couple device (CCD) camera. The magnification is determined by the strength of the objective lens and post-specimen lenses. In scanning transmission mode, the electron beam is focused into a small probe on the specimen and scanned across the specimen. The deflection coils are synced with the detector and display such that the each pixel corresponds to a location on the specimen, this is shown schematically in the block diagram of Figure 1.4. In this case, the magnification is primarily determined by the size of the scan area, with smaller scan areas resulting in larger magnifications. The STEM is similar to the lower voltage scanning electron microscope (SEM). In an SEM, the probe is scanned in a similar way as STEM, except the collected signals are due to secondary electrons (SE) or backscattered electrons (BSE). One of the benefits of SEM and STEM is that it allows the user to collect analytical information such energy dispersive x-ray spectroscopy (EDS) and electron energy loss spectroscopy (EELS) because the signal is correlated with a specific location. The JEOL 2100 FEG microscope used in this work is equipped with scanning coils as well as bright field (BF) and annular dark field (DF) detectors. It is also possible for the TEM column to be equipped with a SE detector as is typical in SEM, however, this detector has not yet been equipped on the JEOL 2100 FEG.

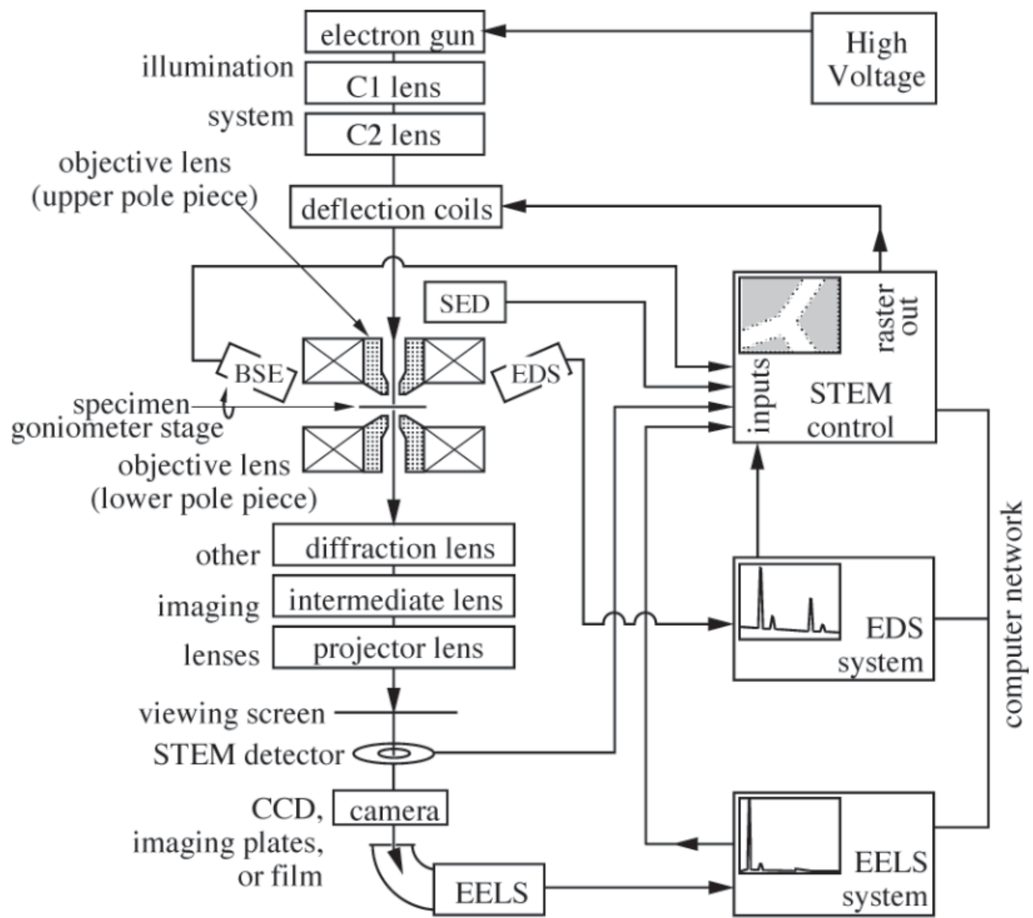

Figure 1.4: TEM/STEM Block Diagram. [59]

In most TEMs there are two primary modes: low mag (LM) mode and mag mode. The main difference between these two modes is that mag mode involves the use of the objective lens while LM mode does not. The objective lens (shown in Figure 1.4) surrounds the specimen and creates a very strong magnetic field ($\sim$2 Tesla) which is responsible for the high resolution capabilities of these instruments. It is arguably the most important aspect of the microscope as it determines the contrast transfer function and thus the image formation. [60] In the case of our JEOL 2100 FEG, a ultra high resolution (UHR) pole piece is used for the objective lens. This is an advantage when performing high resolution microscopy.

However, the objective lens and, in particular, the UHR lens can introduce problems to an experiment. There may be instances when a user might not want the influence of the strong magnetic field on their sample, e.g. magnetic materials. In Lorentz microscopy, LM mode is typically used or the objective lens is manipulated such that the user can apply a magnetic bias to the specimen. One disadvantage of the JEOL 2100 FEG microscope compared to the JEOL 2100 LaB_6 is that the pole piece gap is extremely small in the FEG, around 1.2 mm compared to the LaB_6, which is > 2 mm. Since the very tip of the holder (nose) which holds the specimen is required to fit in this space, it does not leave much room for the user to focus the specimen at the eucentric height. Furthermore, this restriction makes it difficult to design in-situ holders, as is discussed in the next section. Two decades ago there was a need for UHR microscopes since users wanted to push the resolution capabilities of the instrument but more recently there has been a drive away from UHR and towards pole pieces that are large enough to perform experiments inside

the microscope. This is in part due to better engineering of the microscope and astigmatism correctors such as the spherical aberration, C_S, corrector.

One of the limitations to TEM and STEM is that sample preparation, the process of making a nanosized specimen, can often change the original material. Destructive properties such as milling (mechanical or ion beam) can introduce artifacts which make studying the intrinsic properties of a new material more complicated. In the case of power electronics, thinning the material can alter the behavior so significantly that it may not be able to withstand the high voltage it was designed to block. For battery materials, any components that contain Li will oxidize if the battery is opened to make a traditional STEM sample.

1.3.2 In-situ Holders

The most common use for the SEM, TEM, and STEM are to collect structural, morphological, chemical, and elemental information from a static specimen. In this case, the only interactions are between the electron beam and the specimen. For example, one common technique is to perform postmortem analysis on devices that have been cycled, experienced breakdown, or have undergone some other change. This analysis is performed in a TEM using a single or double-tilt holder. The holder can be moved in the x, y, and z direction in order to locate areas of interest and focus them to the correct height in the microscope. The holder can also rotate about its long axis in a single tilt holder and rotate along the short axis at the front (nose) of the holder in a double tilt holder, but otherwise do not interact with the specimen.

There has been an increasing interest in observing the behavior of materials as they undergo changes, especially in observing these changes at the nanoscale. This has led to the development of in-situ or in-operando techniques to study materials in real time. When a specimen is studied *in operando* it implies that the material is behaving the same way it would under real operating conditions. This is sometimes difficult to achieve due experimental limitations which is why materials are often studied *in situ*. This method implies that the device is being manipulated in real time, but it does not mimic true operation of the device. For example, in order to limit the effects of the electron beam on the experiment, one might collect images at a slower rate although still frequently enough to discern any changes happening. [54] In-operando studies are becoming more attainable as microscopes and detectors become more advanced, e.g. the Gatan K2 camera. [61]

The ability to perform in-situ studies is largely due to the development of specialized in-situ holders. These holders are designed in such a way as to facilitate the interaction of the user with the sample. Many of these holders are available through commercial vendors such as Gatan, Hummingbird, Protochips, and DENSsolutions. Because of the spatial and geometric restrictions of most microscopes, many holders are designed for one or two capabilities, and therefore a different holder is often needed for different experiments. For example, there are cryo holders, liquid cell holders, MEMS holders, heating holders, biasing holders, etc. It is also common for labs to build custom holders, although it is becoming easier to partner with commercial vendors to purchase holders with custom designed noses and feed throughs that meet the user's requirements.

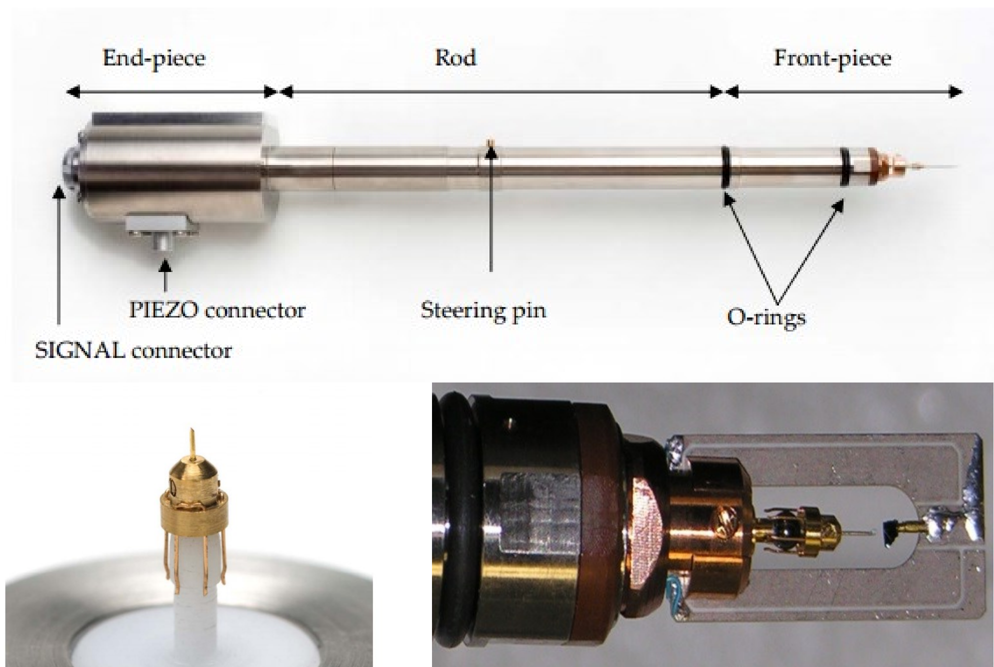

Figure 1.5: Nanofactory In-situ STM Holder. Top figure shows overall holder. Bottom left figure shows the Pt tip mounted in the tip hat. Bottom right figure shows the tip and specimen at the front end of the holder. [62].

The primary in-situ holder used in this dissertation is the Nanofactory STM-TEM holder, shown in Figure 1.5. This is a biasing holder which has electrical feed throughs running through the interior of the holder, with two connections at the air-side of the holder. These two connections, the signal connector and the piezo connector shown in Figure 1.5a, allow the user to interact with the specimen when it is inside the microscope. The signal connector is coupled to the tip hat and the sample mount, which are shown in Figure 1.5c. When the Pt tip (shown 1.5b) makes contact with the sample, the circuit is complete and electrical measurements can be performed. The piezo connector enables the user to move the tip hat towards the specimen. A LabVIEW program and linear amplifiers from Piezo Systems, Inc. Cambridge Massachusetts, are used to apply a voltage to a piezo tube located inside the holder. The tip is driven by a stick-slip method depending on the applied voltage to the piezo, thus allowing the user to slowly move the tip until it makes contact with the specimen. This can be done in extremely small, even nanometer sized, steps which allows for extremely precise adjustments and contact. The Pt tip is electrochemically etched so that the radius of curvature at the tip is small enough to make contact to a surface or even a nanowire.

1.3.3 Electron Beam Induced Current

Electron beam induced current (EBIC) differs from traditional SEM or TEM detectors discussed earlier because the specimen itself acts as the detector. In principle, the electron beam is used to excite a material and create charge carriers which,

in the presence of an electric field, will move and produce a measurable current, i.e. EBIC. It is common to use EBIC in an SEM, where the focused electron beam is rastered across the sample and an EBIC image is formed by coupling the EBIC current to the display monitor, with brighter pixels representing a larger collected current. When combined with traditional SEM detectors such as secondary electron (SE) or backscattered electron (BSE), which measure structure and morphology, one can correlate electronic properties with materials properties at the sub-micron scale. This is demonstrated schematically in 1.6. Furthermore, if combined with traditional STEM detectors, one can correlate these properties at even higher resolution.

When an energetic primary electron collides with valence electrons in the material, it ionizes the atoms to produce an electron in the conduction band and a hole in the valence band, i.e. an electron – hole pair (EHP). Typically, the carriers will diffuse randomly away from the location they were created and will either recombine and annihilate one another or become trapped until all the excess carriers are eliminated. However, the presence of an electric field will cause the carriers to depart from a purely random motion - this nonrandom motion constitutes a current that may be detected in an external circuit. [63] Because there must be an electric field present in the material to collect an EBIC signal, this technique is primarily used to study interfaces, defects, or similar features which change the local bandgap structure and introduce electric fields into a given material. In some cases, an applied voltage is used to increase the strength of the electric field, and thus increase the number of carriers that can be collected.

In the case of measuring the EBIC signal of an ideal interface, the geometry

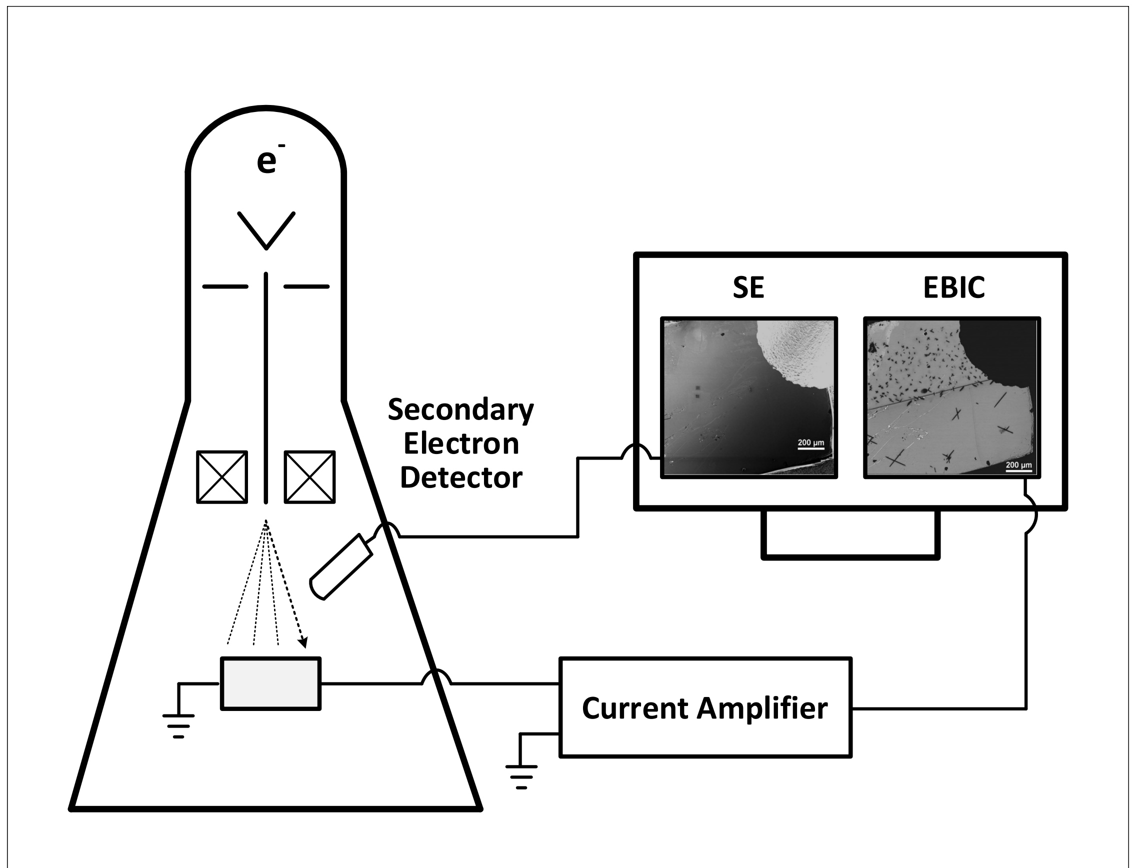

Figure 1.6: SEM with EBIC Capabilities. A TEM/STEM can also be configured for EBIC in a similar way. Figure adapted from [63] with insets from [64].

is described by the orientation of the interface/junction with respect to the electron beam. When the junction is parallel to the beam, it is perpendicular to the raster direction, thus it is referred to as the normal geometry. When the junction is perpendicular to the beam, it is in plane with the raster direction, thus it is referred to as the planar geometry. Lastly, in the depth dependent geometry, the junction is kept in plane with the raster direction of the beam, however, the energy of the incident beam, E_b, is varied, which changes the penetration depth of the incident electrons. All of these geometries can be used to study a p-n junction or a metal-semiconductor contact however, conventionally, the p-n junction is studied by cleaving and using the normal geometry or keeping planar and using the depth dependent geometry, while the metal-semiconductor contact is typically studied via the planar or depth dependent geometry. In this thesis, the planar geometry is used to study the GaN/Ni Schottky diodes.

It is obvious that the collected EBIC current, often referred to as I_{EBIC}, depends on the position of the incident beam, i.e. $I_{EBIC}(x, y)$. Brighter pixels correspond to areas of large EHP generation and diffusion, whereas dark areas correspond to areas which trap or recombine carriers. EBIC mapping is often used in a similar way as its complimentary technique, cathodoluminescence (CL), in order to correlate electrical and compositional properties, and it is common for both methods to be used in an SEM. [65] However, the power of EBIC comes from the usefulness in determining quantitative information about the specimen. Since the EBIC signal is fundamentally determined by the excitation, diffusion, recombination, and collection of minority charge carriers, it is possible to obtain quantitative information

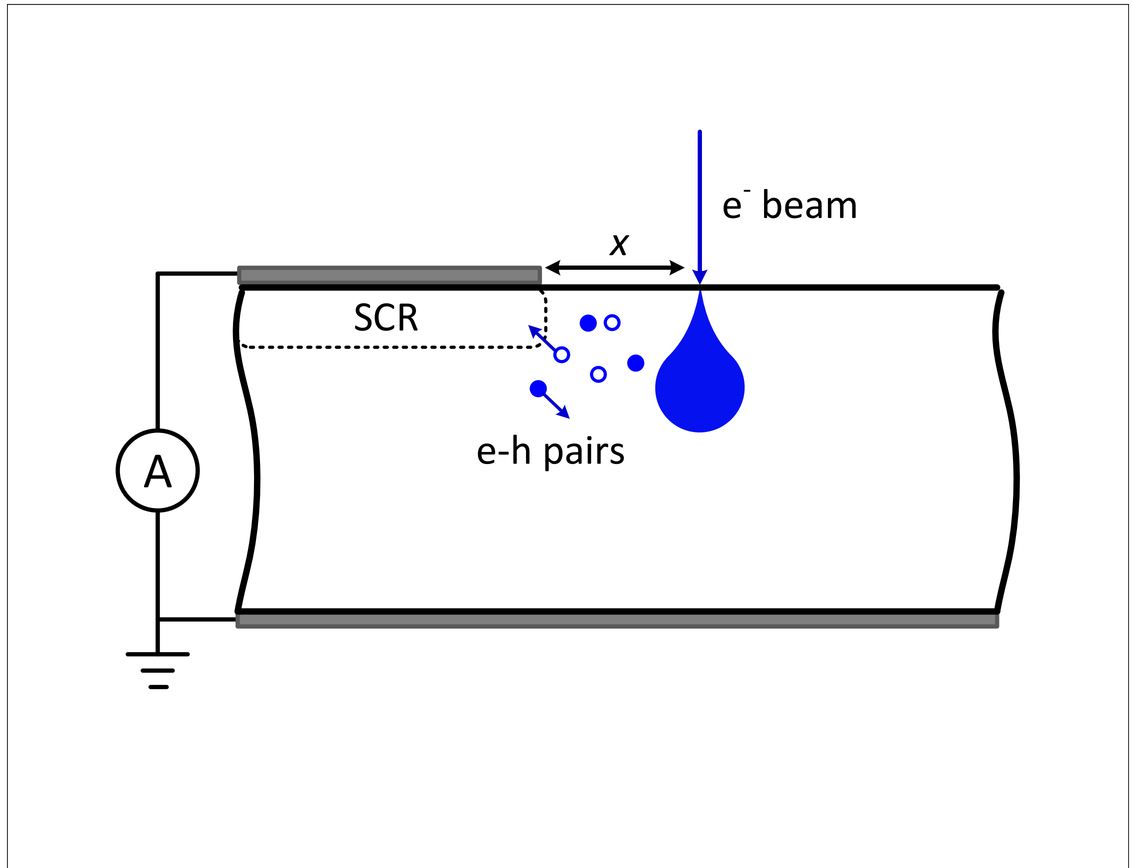

Figure 1.7: EBIC planar geometry. The top contact forms the Schottky junction and the subsequent space charge region (SCR). The bottom (or side) contact forms the ohmic contact.

about these processes in the bulk semiconductor. In particular, EBIC is most often used to determine the diffusion length and recombination lifetime of semiconductors like Si and GaN. [66]

1.3.4 Quantitative EBIC Resolution

In principle, the resolution of an EBIC image is determined by the size of the SEM or STEM probe, which for the purposes of this dissertation is described by

the radius of the incident electron beam, r_0 or d_{beam}. However, even if the probe is well focused on the surface of the specimen, one must consider the interactions below the surface, in the depth of the solid, illustrated schematically in Figure 1.7. This so called interaction volume (IV) or generation volume of the electron beam with the bulk specimen can impair the actual resolution of the technique. This is especially important when considering that early solutions for the planar geometry were derived using point source approximations. For example, Ioannou, Davidson, and Dimitriadis (IDD) derived a simple expression for fitting to experimentally collected $I_{EBIC}(x)$ for a planar Schottky junction, [67, 68] given by:

$$I_{EBIC}(x) \propto x^n e^{-x/L_p} \tag{1.3}$$

where x is the distance from the edge of the planar Schottky junction, L_p is the minority carrier (hole) diffusion length and n is the surface recombination factor - originally 3/2 in IDD model. Their model followed the derivation of Berz and Kuiken, [69] which was for a p-n or Schottky junction in normal geometry. Berz noted that the interaction of the electron beam inside the solid will create an extended generation volume with a penetration depth, R. However they also note that the distribution of holes, Δp, outside the generation volume is the same as those produced by a point source generation and derived their solution with the assumption that the carriers had a long diffusion length, $L_p \gg R$ and a farther scan range $x \gg R$. As Berz, IDD, and others pointed out, [70] this assumption may not always be true. As Luke notes, the point source approximation creates a limit on

the lowest L_p detectable. [71, 72] Leamy approximates this limit as $L_p \sim R$ while Luke argued that this limit is smaller by a factor of four. The overall consensus is that the derived expressions, such as IDD model, cannot be immediately applied to determine L_p in a low micron or submicron ranges without first examining the influence of an extended source on EBIC.

Despite the limitations of the IDD model, it is still commonly used by experimentalists to analyze EBIC data. This is a particular problem for GaN, which has a small L_p compared to Si, and, as pointed out by Yakimov, [23] can cause a significant overestimation of the L_p of n-GaN. One strategy is to use a lower accelerating voltage in order to more closely mimic a point source approximation, however the downside of this method is that the collection efficiency drops substantially, likely as a result of surface recombination. [73] Another strategy is to use the depth-dependent geometry discussed earlier since it is, to first order approximation, indifferent to the generation volume shape and size. The relationship between the EBIC profile and the incident beam energy, E_b, is used to determine the minority carrier diffusion length. Yakimov concluded that the SEM depth-dependent and CL measurements gave the most accurate and consistent result for L_p in n-GaN. Again though, this method can also be affected by surface recombination, especially at the lower E_b range.

Other work by as Boersma *et al.* [74] derived analytical solutions for a planar Schottky or p-n junction under point source generation approximations for a negligible depletion width and arbitrary surface recombination. This solution can be extended to a finite size generation volume by performing a convolution of the

generation volume with the solution to the diffusion equation derived under point source generation. This is the method we use for this dissertation and is discussed in Chapter 2.5.

1.3.5 CASINO

The program CASINO, which stands for "monte CArlo SImulation of electroN trajectory in sOlids" is a useful program for electron microscopists because it simulates electron trajectories in solids. [75, 76, 77] Originally, CASINO was only available for SEM electron voltages, but it was extended to 300 kV in 2010 so that TEM/STEM data could be simulated. [78] When an incident electron impinges on a thick specimen, it will scatter off of the atoms in the solid until it loses enough energy to be considered absorbed by the specimen. The scattering is determined by the incident electron energy (higher energy electrons can penetrate deeper into the specimen), the atomic number (higher Z materials will stop more electrons), the density of the material, and other factors. In CASINO, the relevant electron beam and specimen details are entered into the simulation and a random sampling method is used to generate individual scattering trajectories. The number of simulated trajectories can be decided by the user; larger sampling sizes give more precise numerical results. The scattering trajectories are plotted on the (x,z) plane and the forward scattered electrons are colored blue. The back scattered electrons (those which make it back to the surface of the specimen) are colored red. Other useful information, such as the energy distribution map, is also available. These output files

can be used to understand and explain experimental observations in SEM, TEM, and STEM.

A relevant example of the usefulness of CASINO is shown in Figures 1.8 and 1.9. In this simulation, electron trajectories were simulated for SEM accelerating voltages of 5 kV, 10 kV, and 20 kV, under the same conditions (GaN thickness = 100 μm, $r_0 = 10$ nm, $n_{traj} = 10^4$). As can be seen immediately from 1.8, the width of the interaction volume is dependent on the incident electron energy. Even at a low accelerating voltage, the interaction volume (approximated by the size of the blue trajectories) is well over 100 nm wide. This can complicate the issues of SEM EBIC resolution, as was mentioned in the previous section. In some cases, it is more useful to describe the interaction volume by the electron energy distribution, shown in 1.9. Despite the large size shown in 1.8, most of the energy (75-90%) is actually deposited into the specimen right at the point of injection along a well collimated path. For higher accelerating voltages, the beam is able to penetrate deeper into the specimen and remain highly collimated. This is even more apparent at STEM accelerating voltages - the percentage of backscattered electrons (BSE) goes from 24-25% for SEM to 17-19% for STEM.

CASINO was used in this dissertation to model the electron trajectories at 100 and 200 kV to understand the background signal of the collected bulk STEM EBIC linescans. Entire interaction volumes were simulated and the trajectory statistics were used to determine the long range scattering of backscattered electrons (BSE). Separately, near surface (~ 1 μm deep) trajectories and the corresponding electron energy distributions were performed and used to build the EHP generation function

that was then used in the EBIC numerical simulation.

The CASINO mesh (resolution) depends on the input sample thickness and the divisions parameters in the distributions option. One software note is that if the same exact simulation is run multiple times, without changing any input parameters, a different X/Y range is generated for each run which means that the mesh creation can be significantly different from run to run. Running multiple accelerating voltages (e.g. 100 and 200 kV) in the same simulation also results in different X/Y range for each voltage. Furthermore, we note that the divisions parameter in the "Distributions" option will determine how the mesh is divided in the x/y/z space. Given these factors, it may take the user several iterations to create the appropriate mesh with the necessary resolution for their purpose.

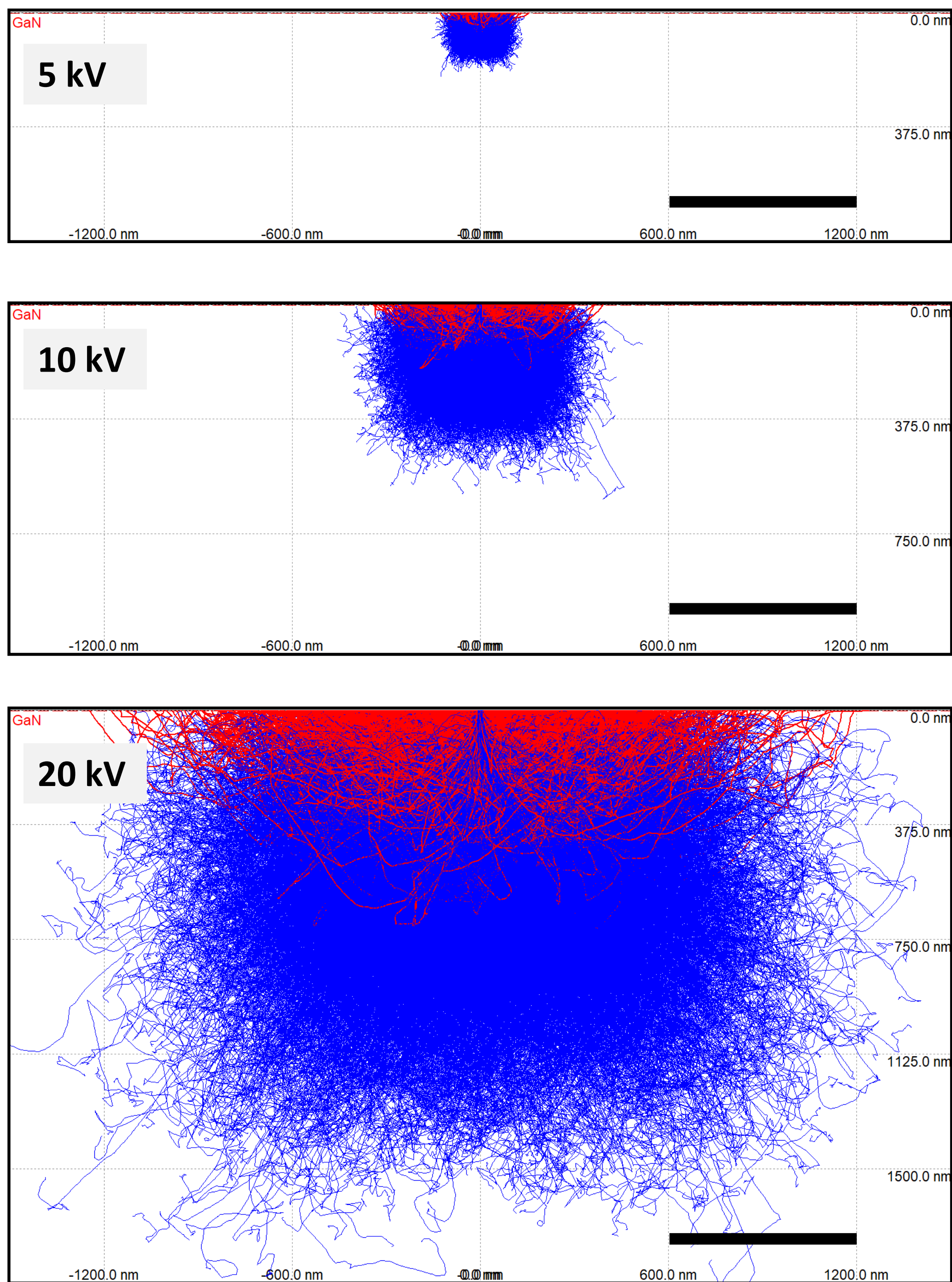

Figure 1.8: CASINO electron scattering trajectories for SEM voltages 5kV, 10kV, and 20 kV. Scale bar is 600 nm.

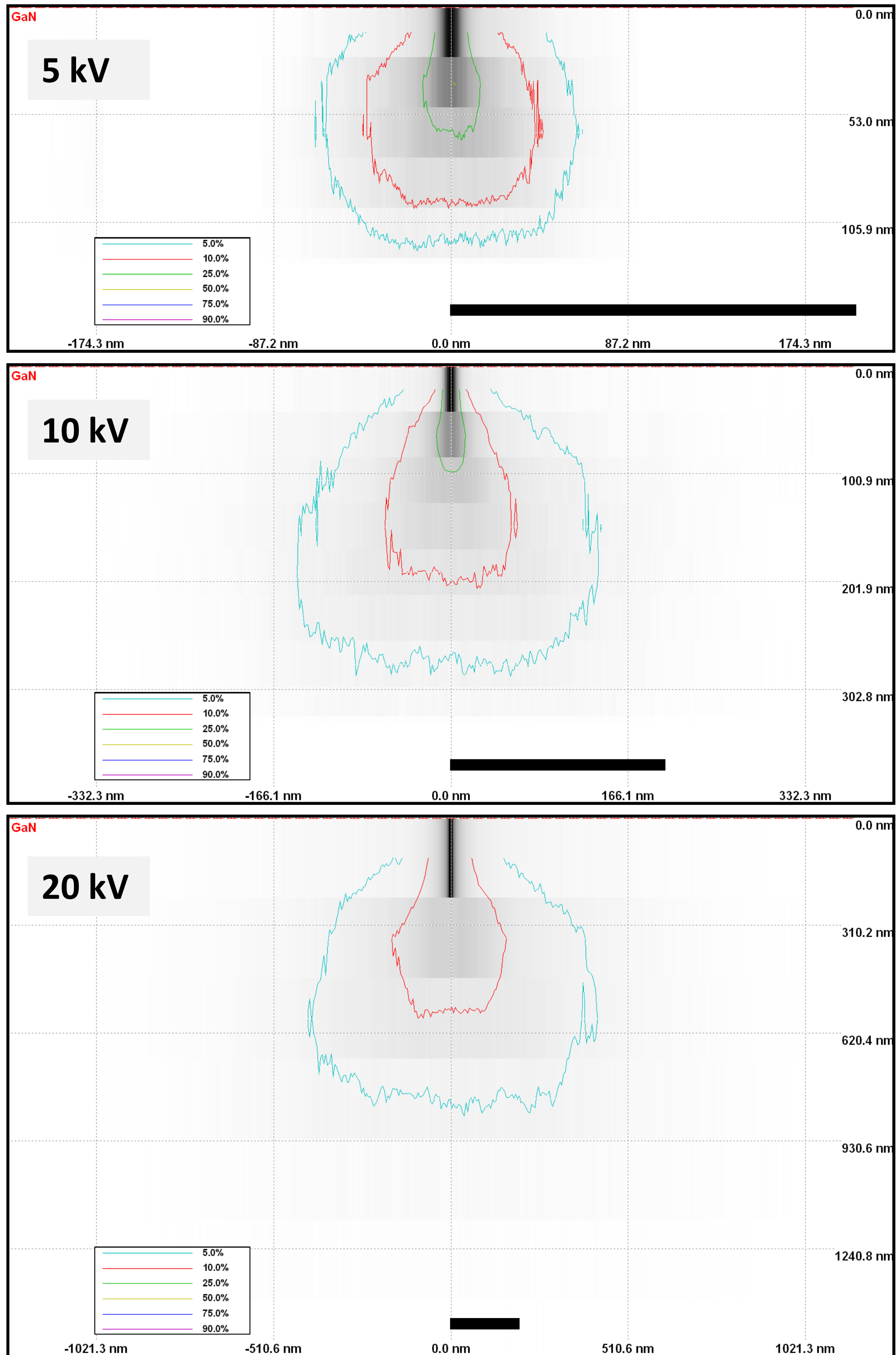

Figure 1.9: CASINO electron energy distributions for SEM voltages 5kV, 10kV, and 20 kV. Scale bar is 200 nm.

Chapter 2: Bulk STEM EBIC

2.1 Preliminary Hypothesis

For those familiar with traditional SEM electron beam induced current (EBIC), the idea of bulk STEM EBIC might sound strange. After all, the size of the interaction volume is a function of the electron beam accelerating voltage, and at STEM voltages, the interaction volume is extremely large (see Figure 2.1). If separating the interaction volume from the minority diffusion length of GaN is already difficult in SEM, as discussed in Section 1.3.4, one might naively assume that it would be even more difficult in STEM. The opposite turns out to be true, as we will explore in this chapter.

In SEM EBIC, the probe size is determined by the entire interaction volume, which is why low accelerating voltages can increase the resolution. However, this suffers from several disadvantages, as was discussed earlier. One of the draw backs of this model is that even at low accelerating voltages, the interaction volume is too large to use a point source approximation for the electron hole pair (EHP) generation. Essentially, the interaction volume begins to approach the length scale of the minority carrier diffusion length in GaN, thus making subsequent analysis difficult.

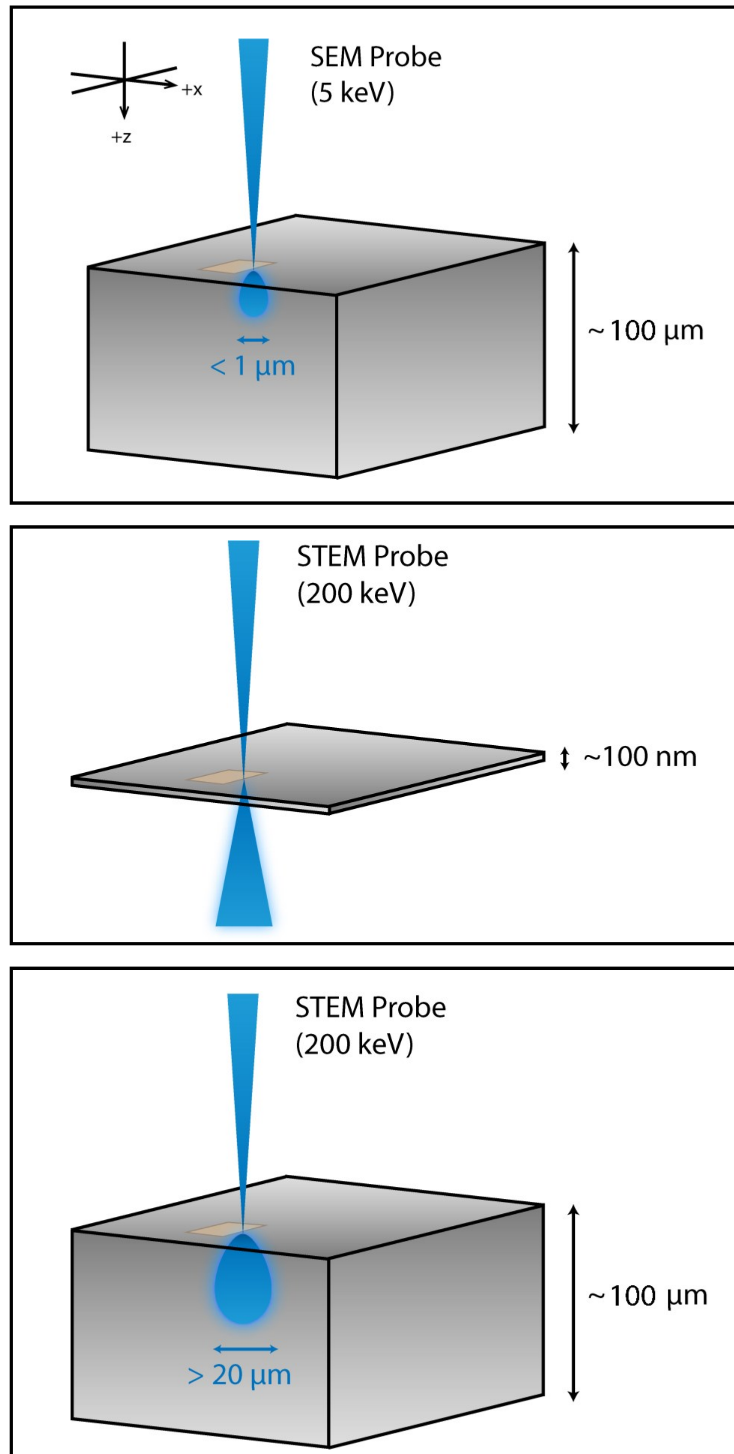

Figure 2.1: EBIC Interaction Volumes for bulk SEM (top), thin STEM (middle), and bulk STEM (bottom).

In this work, the probe size is actually determined by the incident spot size, which enables high resolution EBIC imaging. This is because the electron beam remains highly collimated when it first enters the specimen. There is of course a large interaction volume due to back scattered electrons, however this can be easily modeled and subtracted, resulting in an EBIC profile that can then be fit to a straightforward diffusion/collection model. This is possible because the length scale of the interaction volume is much larger than that of the minority carrier diffusion length, i.e. the reverse situation of SEM EBIC. In SEM EBIC, the interaction volume is *ideally* orders of magnitude smaller than minority carrier diffusion length. In bulk STEM EBIC, the interaction volume is orders of magnitude *larger* than the minority diffusion length, thus making the two length scales easily distinguishable in the analysis.

This chapter describes the collection, processing, and analysis of bulk STEM EBIC for determining the minority carrier diffusion length in n-GaN. The experimental work is complemented by numerical simulations, which confirm our hypothesis. The results, advantages, disadvantages, and limitations of this technique are discussed in this chapter while future work is discussed in Chapter 5.

2.2 Experimental Methods

2.2.1 Sample Preparation

Si-doped, n-type GaN was grown by MOVCD on commercially available hydride vapor phase epitaxy (HVPE) grown free-standing GaN substrate with dislo-

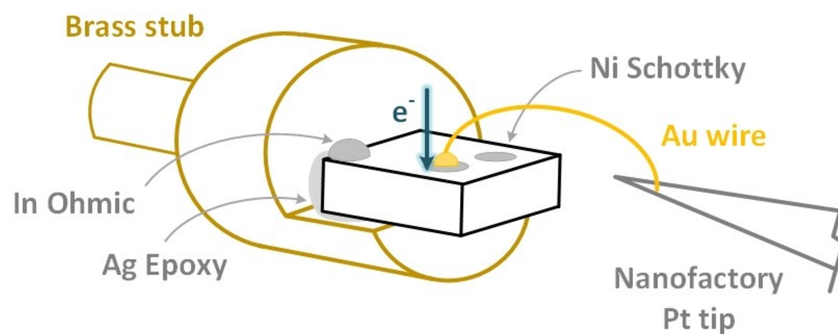

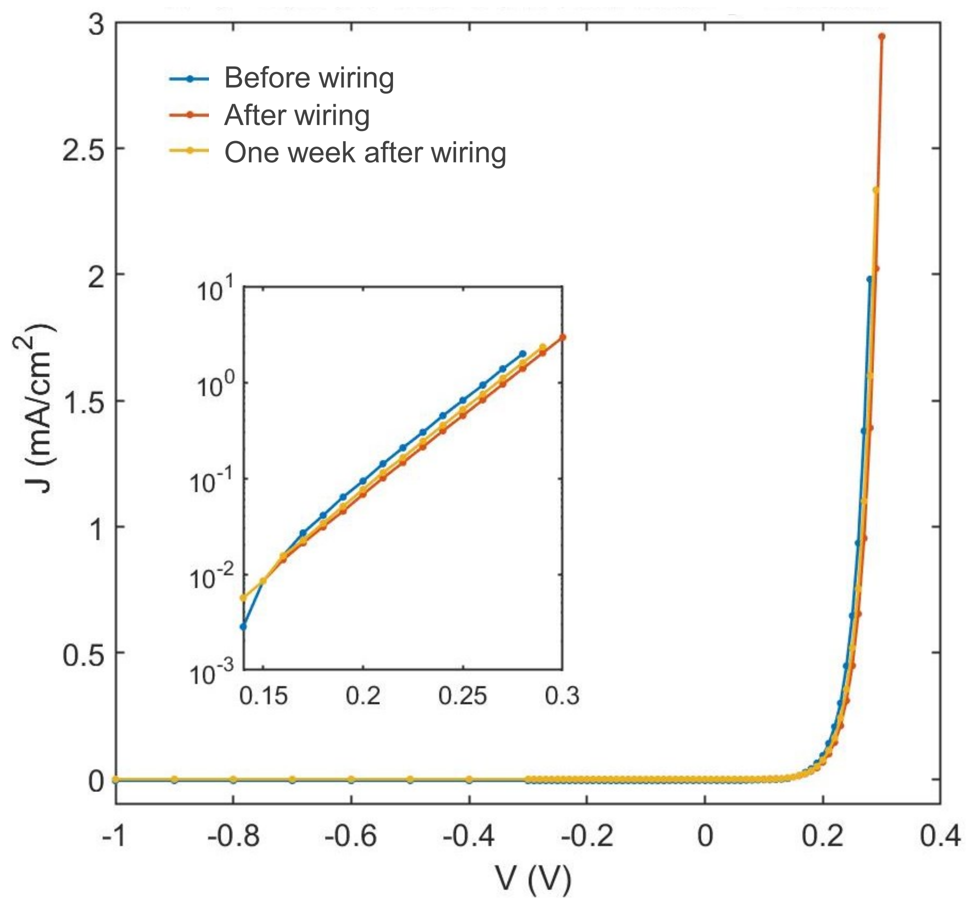

Figure 2.2: Top figure shows bulk GaN specimen mounted to Nanofactory brass stub, including incident STEM probe. Bottom figure shows J-V measurements before and after wiring.

cation densities of $\sim 10^6$ cm^2. The n-GaN epilayers have a net doping concentration of 10^{16} cm^{-3} and a thickness of 8 μm. These samples were received from Sandia National Laboratory, CA, in small wafer size. An array of thin Schottky contacts (10–15 nm thick) was formed by evaporating Ni through a shadow mask, either at Sandia or at UMD. Indium solder was used to form the ohmic contacts. Specimens of approximately 2 x 4 mm^2 were cleaved and mounted to disposable brass stubs which are compatible with the Nanofactory STM in-situ holder (discussed in Section 1.3.2). Au wires were wire-bonded to the Ni contacts and then connected to the Nanofactory Pt tip. Ag epoxy was used to connect the In ohmic to the other side of the holder. The sample geometry is shown schematically in Figure 2.2. J-V measurements were collected before and after specimen preparation to verify that the rectifying behavior of the contact had not been altered. A detailed description of the sample preparation can be found in Appendix A.

2.2.2 EBIC Collection

Before inserting the NanoFactory holder into the microscope, the STEM probe is aligned in LM and mag mode using a typical electron-transparent sample such as gold nanoparticles on holey carbon. Once the alignment is satisfactory, the Nanofactory holder is placed inside the microscope. Unfortunately there is no secondary electron detector attached to the JEOL 2100 FEG, so the EBIC current itself is used to find the area of interest. The signal output of the Nanofacotry holder is coupled to a DL Instruments current preamplifier [79] which is then coupled to the

Gatan Digiscan system to produce a current map. When not near the Ni pad, no current is produced and thus the image is simply due to noise ($\sim$ pA), but once the Ni pad is located, the EBIC signal is very bright. The probe is re-focused using the EBIC image and either the height (in mag mode) or the focus knobs (in LM mode). A comparison of optical and EBIC micrographs are shown in Figure 2.3. The pixel intensity corresponds to the amount of current detected, which depends on the beam voltage and current density. For the settings used in 2.3, the current on the Ni pad was approximately 220 nA (see Section 2.3.4 for details). Due to significant ground noise, a custom power supply was built to power and isolate the preamplifier from the wall. Other best practices included twisting BNCs together to prevent ground loop noise and grounding the experiment to the microscope ground, both of which greatly improved the quality of the images.

Figure 2.3 also shows the higher magnification micrograph of the Ni/n-GaN edge, again where the current is high on the Ni and low on the GaN. Any linescan which crosses the edge shows a characteristic decay profile such as that in the inset of 2.3. Again, this is due to the planar Schottky geometry, and as such can be fit using an appropriate collection model. Qualitatively, the characteristic profile has (1) a sharp decay due to diffusion of charge carriers to the junction and (2) a long decay due to the long range back scattered electrons. After appropriate processing, background subtraction, and analysis, the minority carrier diffusion length, L_p, of n-GaN can be determined from these linescans. Furthermore, as discussed in Chapter 3, in-situ measurements are also possible and can provide further information about the electronic properties of the material.

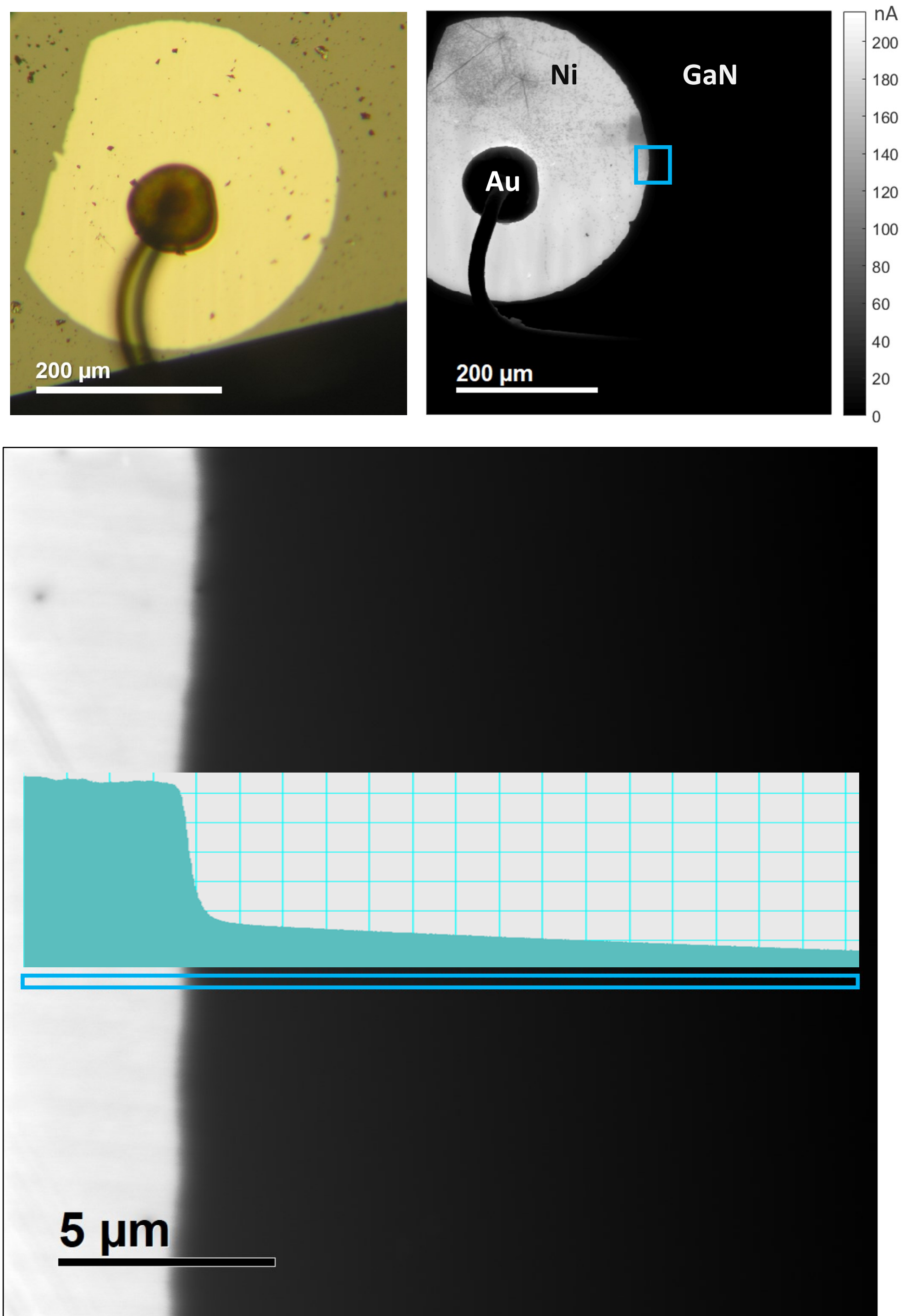

Figure 2.3: Top figures show optical (left) and 200 kV EBIC (right) micrographs of the same specimen. Bottom image is of 200 kV LM 15kx EBIC micrograph with the subsequent collected line profile which shows the characteristic decay profile.

2.3 Data Processing

2.3.1 LM STEM Magnification Calibration

Magnification calibration is a necessary and standard procedure for any user who wishes to extract quantitative information from micrographs or diffraction patterns. [60] This is especially important when collecting images in low mag (LM) mode, since the JEOL 2100 FEG is not optimized for this mode. Simply put, the magnification scale bar in LM mode is incorrect, especially when the accelerating voltage on the microscope is set to 100 kV. In Figure 2.4, two 15,000 x magnification STEM DF images are shown before and after calibration. Before calibration, the scale bars both show 5 μm, however, the 200 kV appears to be at a higher magnification than the 100 kV, therefore one – or both – of the calibrations are incorrect. The scale bar for EBIC images collected in LM STEM at 15 kx were calibrated using the sample CAT #603 Latex Spheres on Diffraction Grating from Ted Pella. The diffraction grating and the latex spheres have a known length. The diffraction grating has a known length scale of 0.463 μm. Before calibration, the diffraction grating size measured 0.237 $\pm$ 0.010 μm for 100 kV and 0.388 $\pm$ 0.013 μm for 200 kV. After the calibration, the diffraction gratings measured 0.463 $\pm$ 0.010 μm. The pixel size is calibrated in Gatan Digital Micrograph (GMS3), in the image info "image calibration" scale dimensions option, before exporting the files from GMS3. The intensity scale (i.e. EBIC current) is calibrated in Matlab after the linescan is exported from digital micrograph, discussed in Section 2.3.4.

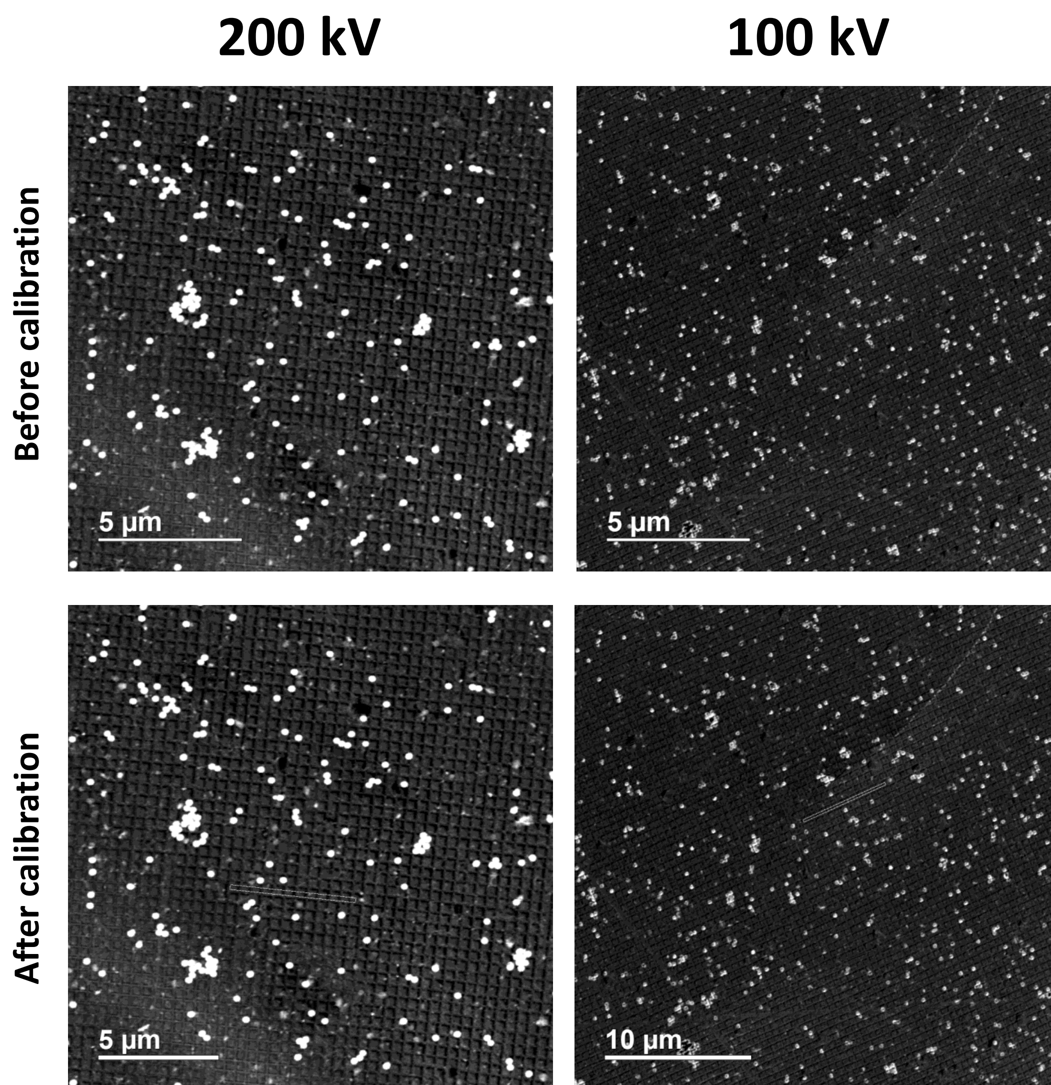

Figure 2.4: LM DF STEM micrographs of latex spheres on a diffraction grating (Ted Pella #603) which were used to calibrate the pixel size for 100 and 200 kV.

2.3.2 Image Resolution Estimate

After calibrating the magnification to ensure that we have the correct pixel size, we estimate the EBIC image resolution by measuring the STEM LM resolution. While the resolution is normally approximated by the probe size in STEM mag mode, JEOL does not report the spot size in LM as a number, just simply "L." In order to estimate the "effective resolution" of the images, one can use a pristine holey carbon on copper grid and measure the resolution of the edge of the holey carbon. This is done by selecting a line scan perpendicular to the holey carbon edge which crosses from vacuum (intensity is zero) to the holey carbon (where intensity is constant nonzero). The numerical derivative of the line scan is then fit to a Gaussian, and the resolution is estimated as the full width at half maximum (FWHM). This was done for images while varying the accelerating voltage, image size, scan speed, and integration width. An example of the analysis is shown in Figure 2.5, which compares two images taken at different images sizes. Both were collected for 200 kV, at 15 kx, with a scan speed of 16 μs/pixel, and an integration width of 10 pixels. The pixel size was 20 nm and 40 nm for 1024 and 512 respectively while the effective resolution was 60 nm and 70 nm respectively. The resolution at 100 kV is approximately the same. A probe size of 60-70 nm is used as the beam diameter in both CASINO and Matlab simulations.

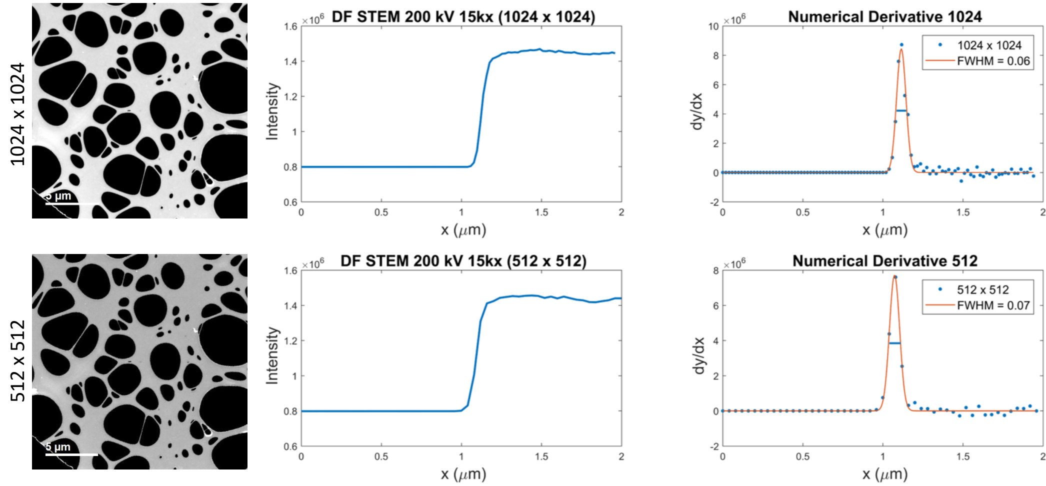

Figure 2.5: Example of LM resolution estimate for 200 kV at 15 kx.

2.3.3 EBIC Linescan Selection

Depending on the size of the collected EBIC image, there are 512 or 1024 horizontal lines that form the image. Since the current, I_{EBIC}, has a characteristic decay away from the edge of the Ni Schottky contact, we select a line which is perpendicular to the Ni/GaN edge (integration width is typically ten pixels to increase the signal-to-noise ratio). The minority carrier diffusion length is a fundamental property of the material, so we *should* be able to select any area and obtain the same quantitative results. This is true for most cases, as shown by the example in Figure 2.6b. Four horizontal linescans were chosen, listed as A-D. These lines were chosen semi-randomly, while considering two features of the vertical line scans shown in Figure 2.6a. First, there is a background AC noise which can be seen in the

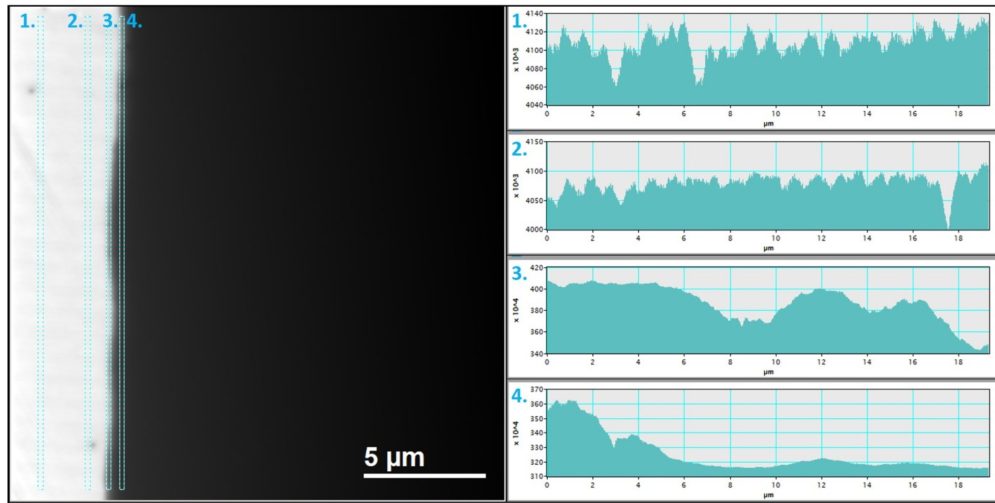

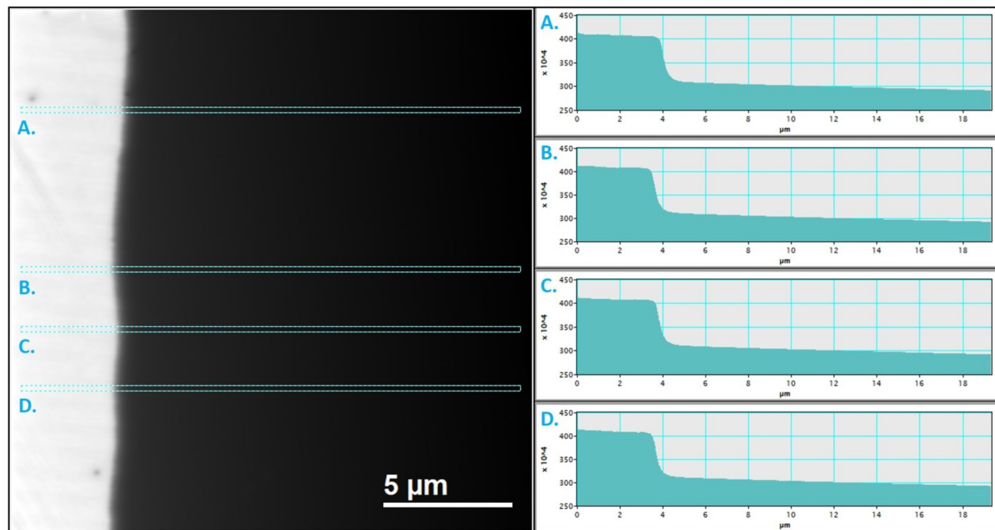

Line	*R* (µm)	L_p (nm)
A	31.2 ± 0.9	190 ± 3
B	33.7 ± 0.9	194 ± 3
C	33.5 ± 0.9	188 ± 4
D	34.3 ± 1.0	187 ± 3
Avg ± StDv	**33.2 ± 1.2**	**0.190 ± 2**

Figure 2.6: EBIC collected at 200 kV 15 kx. The top figure shows vertical linescans which reveal scan noise as well as non-uniformity in the Ni deposition. The middle figure shows the four horizontal linescans (A-D) which were analyzed using methods described in Section 2.4 and 2.5 Results for the background long range scattering, L_{LR} and the minority carrier diffusion length, L_p are tabulated.

profile for lines 1 and 2. Secondly, the Ni deposition onto the GaN is not uniform, which can be seen in vertical lines 3 and 4. Keeping this in mind, the exact location of the lines A-D were chosen based on which areas consistently had the flattest slope for all four vertical lines.

Lines A-D were analyzed using the methods described below (Section 2.4, 2.5, and 2.6), and the results are tabulated in Figure 2.6c. The average minority carrier diffusion length, L_p, was determined to be 190 nm with a 2 nm standard deviation. The average background long range scattering decay, L_{LR}, was found to be 33.2 μm with a standard deviation of 1.2 μm. In summary, a single EBIC image provides consistent measurements across the entire Ni/GaN interface. Lastly, differences in the minority carrier diffusion length are observed in this work, and are attributed to electron beam irradiation. This is discussed in detail in Section 2.6 and 3.1.

2.3.4 EBIC Current Calibration

Once the area of interest is narrowed down, the profile of the linescan is exported using a script in Digital Micrograph. [80] This exports the data as a two-column text file with the first column corresponding to the position values and the second column corresponding to the intensity values. The scale calibration (x values) is done in Digital Micrograph before exporting and the intensity calibration (I_{EBIC}) is done in Matlab. The current is scaled according to separate measurements collected before an EBIC image of the Ni-GaN junction has been collected. Two EBIC images are taken, one scanned on the pure GaN side of the junction,

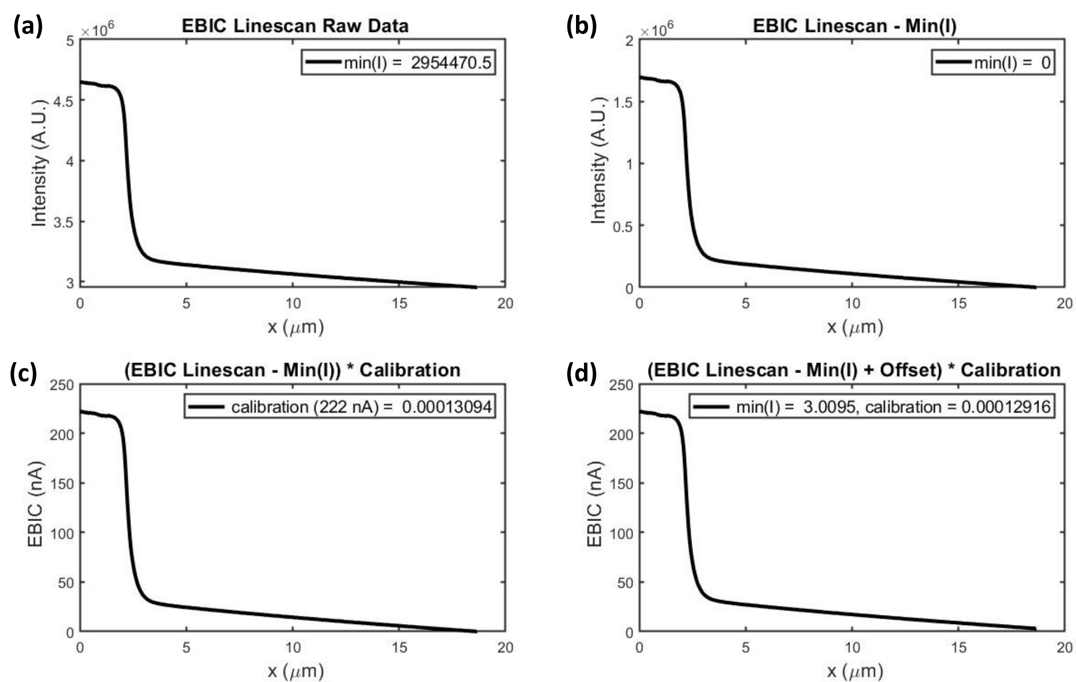

Figure 2.7: EBIC Current Calibration Example (a) Uncalibrated EBIC data in A.U. (b) Data after the minimum A.U. intensity has been subtracted. (c) Data multiplied by calibration factor to correct the maximum intensity. (d) Data with an added offset to correct the minimum intensity.

the other on the Ni side. While this scan is taking place, the voltage readout is recorded, and an average current for the image is calculated based on the settings of the current amplifier. For example, for the sample shown in 2.7, the average current measured on the GaN was 3 $\pm$ 0.5 nA while the average current measured on the Ni side was 222 $\pm$ 0.5 nA. These numbers depend not only on the specimen properties, but also on the beam voltage and beam current setting of the microscope. Using the average current measurements, the raw data is scaled so that the maximum and minimum points correspond to the Ni and GaN currents, respectively. The maximum and minimum are used because those are the points when the scan is farthest away from the junction and is assumed to represent what the average current away from the junction would be. Once the data is correctly calibrated it is analyzed using methods discussed in the remaining sections.

2.4 Long Range Background Subtraction

As shown in Figure 2.7d, there is a significantly long range EBIC signal several microns away from the Ni edge. This signal can not be attributed to the diffusion length of n-GaN, since it is nominally less than 1 μm, [23] and thus the signal is attributted to long range back scattered electrons (BSE). The main focus of this section is to sufficiently describe and subtract the long range signal so that the subsequent EBIC profile can be analyzed with respect to diffusion mechanisms only.

A long range decay length, L_{LR}, is used to describe the observed long range EBIC signal. L_{LR} is simply a measure of the size of the interaction volume in

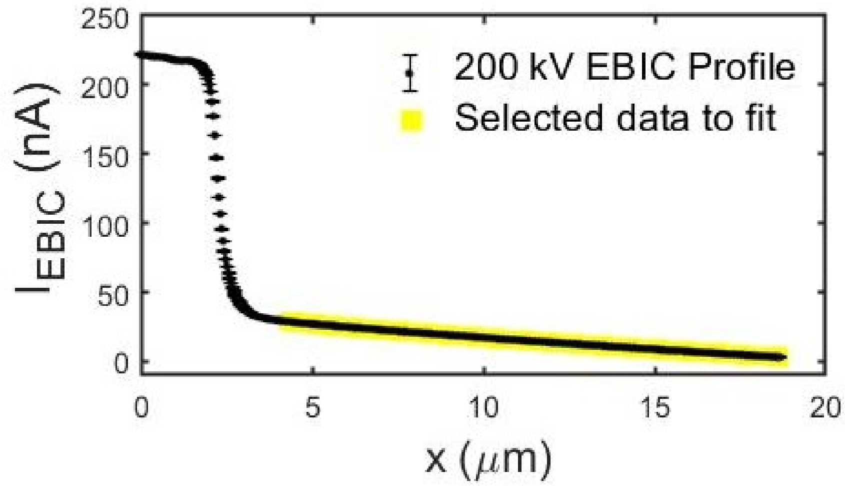

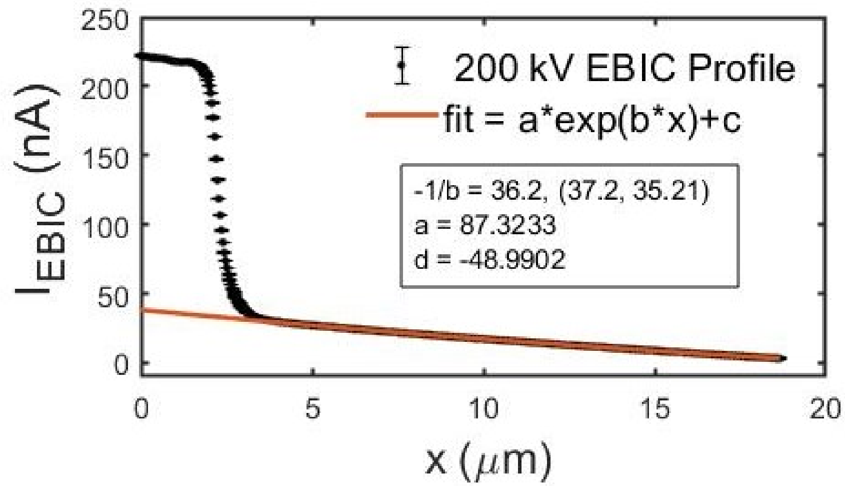

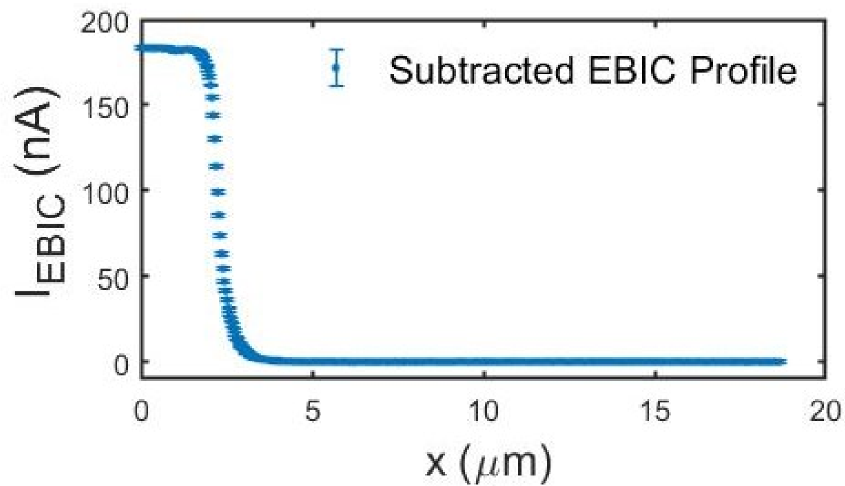

Figure 2.8: Example of background subtraction for bulk STEM EBIC micrograph acquired at 200 kV and 15 kx.

bulk STEM EBIC, and thus it does not shed any light onto the specific materials properties of GaN. That being said, it is useful to consider the physical meaning of L_{LR}, and to justify the necessity of subtracting this signal from the initial data.

The functional forms considered for fitting the background signal were a single exponential decay, a Gaussian profile, and a complementary error function. Ultimately, the exponential decay profile was used for all linescans discussed in this work so that the data could be appropriately compared. An example of the fit and subtraction is shown in Figure 2.8; where the data shown in 2.8a is the same as that shown in 2.7d. The characteristic long range decay length is defined as $L_{LR} = 1/b$, which, for 200 kV at 15 kx gives $L_{LR} = 36.2 \pm 1.0$ μm.

EBIC micrographs of the same sample were acquired at 100 kV and 200 kV at 15 kx. The results are tabulated below, in Table 2.1. The measurements are consistent with a simple penetration depth model of the interaction volume, discussed in the next section. At 200 kV, a lower magnification is necessary to fully capture the size of the interaction volume. Since the exact value of L_{LR} is not needed, it is preferable to use 15 kx magnification since the resolution of the EBIC image is higher, and thus the error on subsequent minority carrier diffusion lengths is lower.

E (Magnification)	L_{LR}
200 kV (15 kx)	36.2 ± 1.0 μm
100 kV (15 kx)	6.7 ± 1.0 μm
200 kV (5 kx)	30.0 ± 0.5 μm

Table 2.1: Long range decay lengths which describe the large interaction volume of the beam with GaN. This signal is subtracted from the data before further analysis.

2.4.1 Electron Penetration Depth Theory

When an electron beam interacts with a specimen there are many different phenomena that occur. The electrons will be elastically or inelastically scattered in the forward and backward direction, and the electron/specimen interactions will generate secondary electrons, x-rays, Auger-Meitner electrons, etc. In SEM (or bulk STEM) the specimen is typically several microns or millimeters thick, so the electron beam is stopped by the sample through many scattering events. The average distance that the electron travels through a medium is described by the penetration depth, R, typically described empirically by:

$$R = \left(\frac{C}{\rho}\right) E_b^{\gamma} \tag{2.1}$$

where ρ is the material density, E_b is the incident energy of the electron beam in eV, and γ is 1.75 for air,[81, 82] and 1.67 for solids. [83] Grun's expression was determined based on experimental work on electron penetration in air, and confirmed by Everhart and Hoff, however they note that γ depends on the material property. C is a proportionality constant given as $C_{Grun} = 0.0457$, $C_{Kanaya} = 0.0844$. Kanaya also includes a correction factor for relativistic electrons. As shown in Figure 2.9, the penetration depth increases with increasing accelerating voltage, as expected. By adjusting the proportionality constants, the penetration depth theories can be used to fit the observed beam energy dependence of L_{LR}, also shown in 2.9. As expected, L_{LR} is longer for larger E_b.

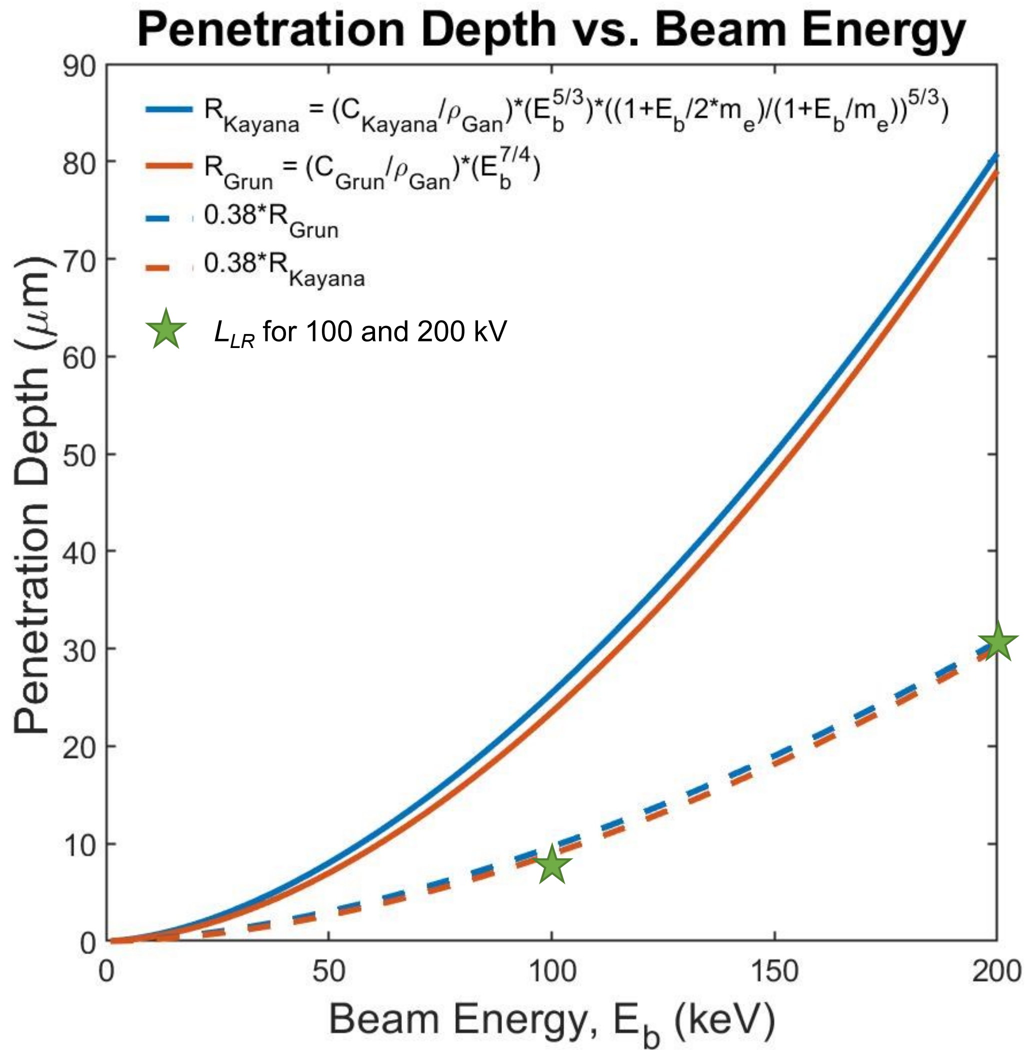

Figure 2.9: Penetration depth model for the distance an electron can travel into a solid material for a given beam energy. Measured values for L_{LR} described by this model when the proportionality constants are adjusted.

2.4.2 CASINO Simulations of Long Range Scattering in GaN

While the penetration depth theory discussed in the previous section is useful to understand the dependence of L_{LR} on beam energy, in EBIC planar Schottky geometry the raster direction is perpendicular to the penetration depth. Therefore it is more accurate to describe L_{LR} as a measurement of the width of the interaction volume, not the depth. Monte Carlo simulations were performed using the program CASINO to simulate a high energy electron beam scattering in 100 μm thick GaN. The surface radius distribution of back scattered electrons was used to approximate the width of the interaction volumes (see Figure 2.10). The decay lengths were found to be 5.2 μm and 16.7 μm for 100 and 200 kV respectively. This simulated long range scattering is shorter than the measured L_{LR} for 200 kV. The difference is attributed to electron channeling in GaN, which is not accounted for in CASINO.

The method and results of subtracting the long range scattering are consistent with previous work by Parikh, et. al. [84, 85] They find that the radial distribution of energy deposition can be split into two components: one due to forward scattered electrons (FSE) which results in a spatially narrow distribution, and another due to BSE which results in a spatially diffuse distribution. There may be a case where some BSE are scattered through extremely large angles, and thus might contribute to a broadening of the spatially narrow distribution, however, CASINO simulations show that the total number of BSE comprise only 17-19% of the incident electrons. An even smaller amount of the total BSE are scattered through such large angles, which means only a small fraction of BSE which would contribute to such broadening.

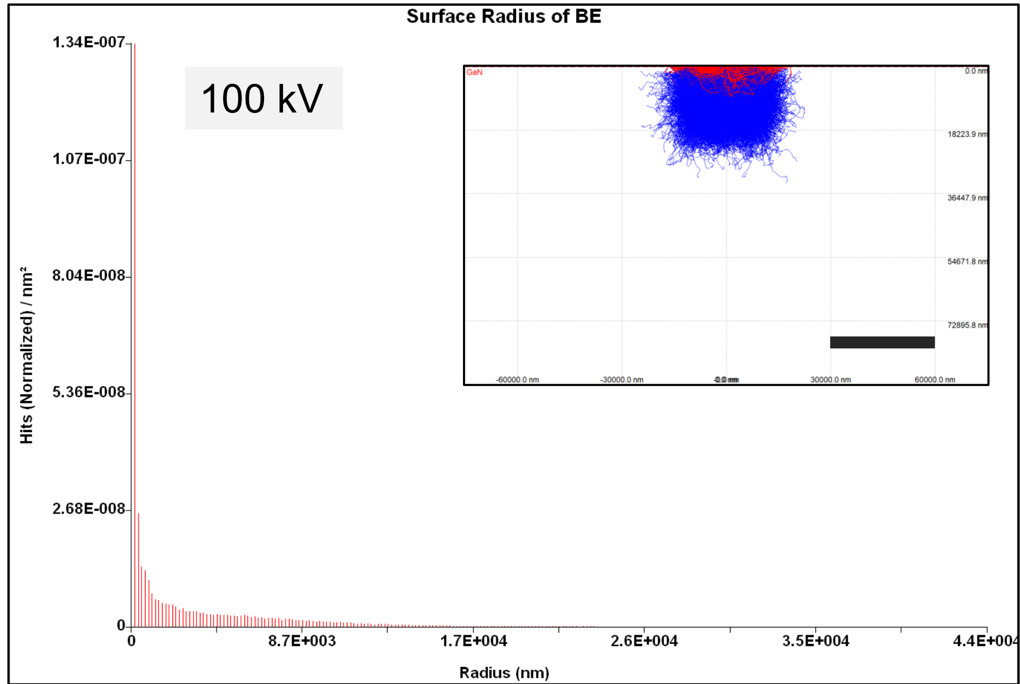

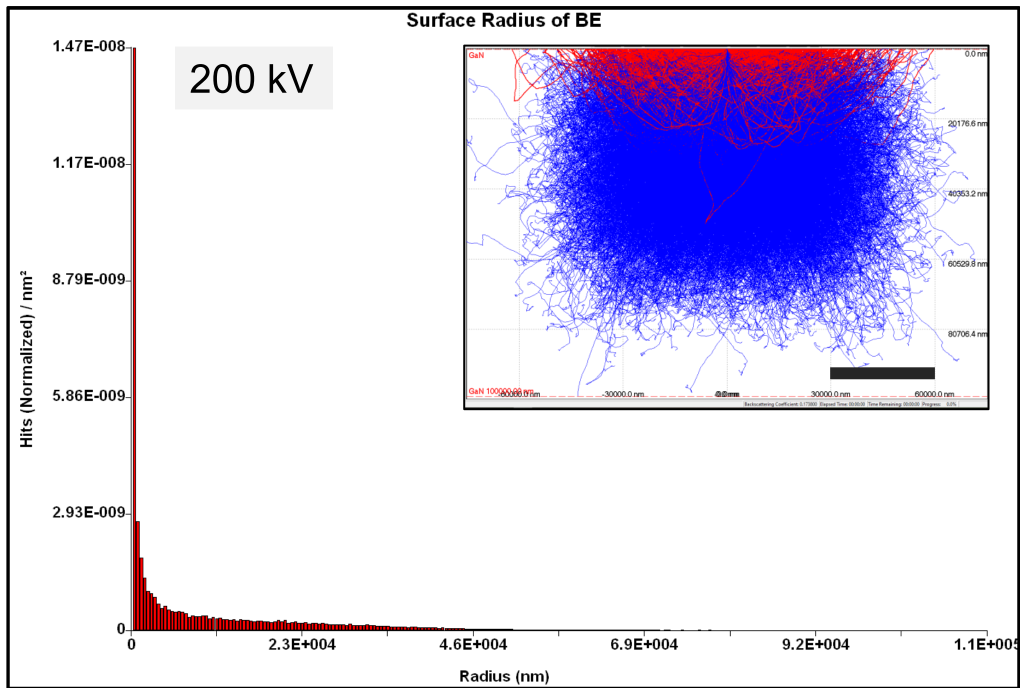

Figure 2.10: Results from CASINO Simulations of electron trajectories in 100 μm thick GaN. The surface radius distribution of BSE was used to estimate the width of the interaction volumes at 100 and 200 kV. Scale bar of insets is 30 μm. (Note: scale of x-axis is different for surface radius distributions).

2.5 Modeling Bulk STEM EBIC

After subtracting the background signal, the resulting EBIC profile shown in Figure 2.8c is only due to the generation of holes from forward scattered (i.e. short range) electrons and the subsequent diffusion and collection of those carriers. This allows for a simple model for the predicted current, which avoids the complication of having to simulate the short and long range scattered electrons. The goal of this section is to show that the best choice for fitting to bullk STEM EBIC profiles is the complementary error function (erfc) fit similar to that used by Boersma *et al.* [74] While Boersma's model could be adapted to apply to the bulk STEM planar geometry, it is the author's opinion that, much like the IDD model discussed in Section 1.3.4, our straight forward model will aid in the adoption of this technique by EBIC experimentalists.

Following the derivations of Donolato and others, [86, 87, 88, 89] it can be shown that the general form for the collected current, $I_{EBIC}(x_0)$, for a Schottky planar geometry can be expressed as a convolution of the normalized electron-hole pair generation function, $g(x, y, z)$, and the collection probability, $p(x, y, z)$, written as:

$$I_{EBIC}(x_0) = \int_{W_{dep}}^{0} \int_{-\infty}^{\infty} \int_{x_0}^{\infty} g(x, y, z)\, p(x, y, z)\, dxdydz \qquad (2.2)$$

where x_0 is the beam position, W_{dep} is the depth of the depletion region, and $p(x, y, z)$ is the solution to the homogenous diffusion equation. The functions used for p and

g are described in the next section. Rather than solving this integral by hand, a numerical convolution was performed in Matlab, discussed in Section 2.5.4.

2.5.1 Diffusion Equation Solution

Following the derivations from Van Roosbroeck, [90] Berz and Kuiken, [69, 91] and others, [63, 92] we start with the continuity equation for minority carriers (holes) in an n-type semiconductor in one dimension [5]:

$$\frac{\partial \Delta p}{\partial t} = G_p - \frac{1}{q}\frac{\partial J_p}{\partial t} - R_p \tag{2.3}$$

where G_p and R_p are the generation and recombination of holes and J_p is the current density of holes due to drift and diffusion, $J_p = q(\mu_p p \mathcal{E} - D_p \frac{\partial p}{\partial x})$. Substituting J_p and assuming (1) constant D_p and (2) carriers are generated outside the depletion region, ($\mathcal{E} = 0$), we get the hole diffusion transient state:

$$\frac{\partial \Delta p}{\partial t} = D_p \frac{\partial^2 \Delta p}{\partial^2 x} \tag{2.4}$$

which is equivalent to Fick's second law of diffusion of atoms in a solid. For the case of a thin source, whose concentration goes to zero at infinity, the solution can be written as [93]:

$$p(x,t) = \frac{p_0}{\sqrt{4\pi D_p t}} \exp \frac{-x^2}{4D_p t} \tag{2.5}$$

To isolate the spatial dependence, we introduce the characteristic time scale,

τ_p, and integrate with respect to time, employing the Dirac delta function as follows:

$$p(x) = \int_0^\infty \delta(t - \tau_p) \frac{p_0}{\sqrt{4\pi D_p t}} \exp \frac{-x^2}{4D_p t} = \frac{p_0}{\sqrt{4\pi D_p \tau_p}} \exp \frac{-x^2}{4D_p \tau_p} \tag{2.6}$$

Introducing the characteristic length scale, $L_p \equiv \sqrt{D_p \tau_p}$, Equation 2.6 becomes:

$$p(x) = \frac{p_0}{L_p \sqrt{4\pi}} \exp \frac{-x^2}{4L_p^2} \tag{2.7}$$

Finally, we extend this derivation from a thin source in one dimension to a point source in three dimensions. After normalizing the integration constants, Equation 2.7 becomes:

$$p(x, y, z) = \frac{p_0}{(L_p \sqrt{4\pi})^3} \exp \frac{-(x^2 + y^2 + z^2)}{2L_p^2} \tag{2.8}$$

Intuitively, this equation describes a model in which, after the hole is created, it diffuses outward radially with a length scale described by the minority carrier diffusion length, L_p.

2.5.2 Generation Volume Equation

Choosing the correct electron hole pair (EHP) generation volume function, $g(x, y, z)$, is important because, as discussed earlier, this can dramatically affect the predicted current results. Parish *et al.* [94] and Kurniawan *et al.* [95] discussed the most popular choices for generation volumes for modeling SEM EBIC currents, such

as those by Donalto, [96] or Bonard.[97] Both authors conclude that Monte Carlo simulations of electron-solid interactions can be used to either validate analytical expressions for g or, in the case of numerical simulations, can be used for generation volumes in place of the analytical models. This is based on the assumption that the EHP generation volume can be approximated by the energy deposition distribution from Monte Carlo simulations.

Following the methods from Parish and Kurniawan, we use CASINO to validate the chosen generation volume for STEM voltages at 100 and 200 kV. A Gaussian generation function which spreads out as the beam penetrates deeper into the specimen (negative z) can be written as:

$$g(x, y, z) = \frac{1}{\sqrt{2\pi}(r_0 - \alpha z)} \exp \frac{-(x^2 + y^2)}{2(r_0 - \alpha z)^2} \tag{2.9}$$

where r_0 represents the initial STEM probe size and α represents the beam spread of the forward scattered electrons. As z becomes more negative, the spread of the beam becomes larger. Additionally, α is a function of the incident beam energy and is inversely proportional to the incident beam energy. Higher incident energy will result in less spread. The most appropriate value for r_0 is given by the resolution estimate from Section 2.3.2.

In order to estimate an appropriate α, simulations of the incident beam in GaN were performed used CASINO. Input voltages of 100 and 200 kV were used with a beam diameter of 70 nm. A simulation depth of 2 μm was used. A larger depth could have been simulated, however the pixel size that CASINO uses for larger meshes

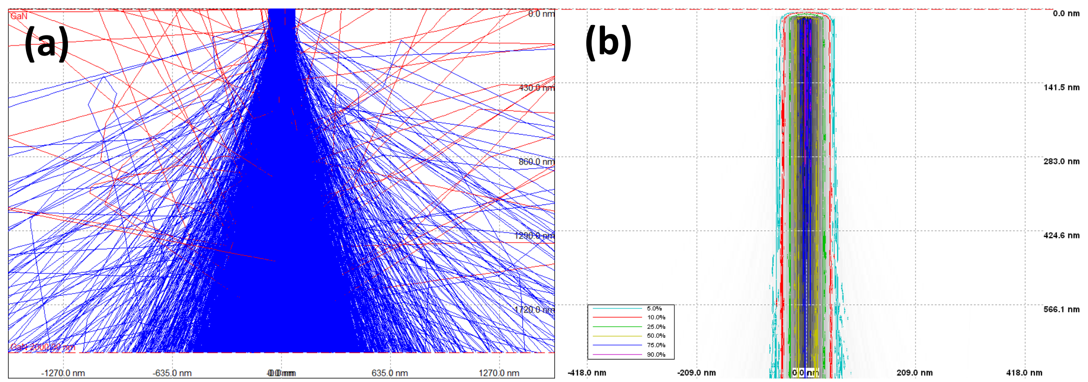

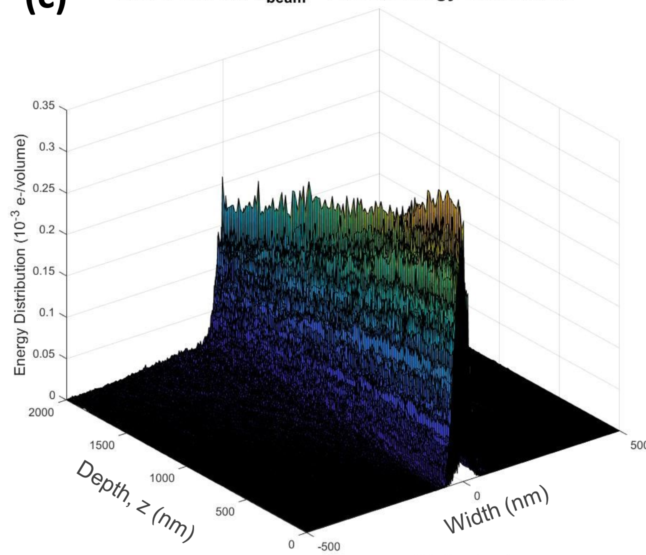

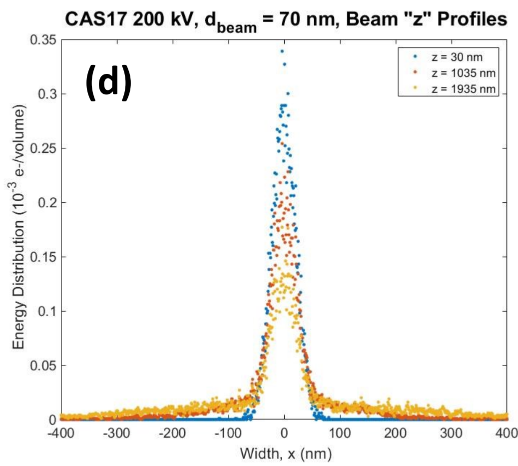

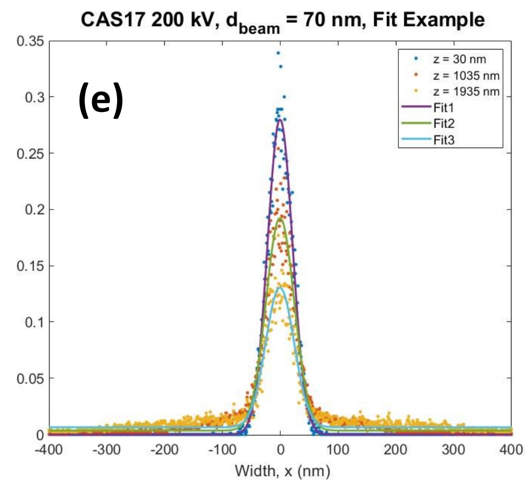

Figure 2.11: Results from CASINO simulations for 200 kV with beam diameter of 70 nm. See 2.12 for results from Gaussian fits.

would have made subsequent analysis unhelpful. It is also unnecessary to simulate much deeper than 2 μm, since holes created below this depth will not be able to diffuse to the depletion region. The trajectories output and energy distribution output for 200 kV is shown in Figure 2.11a and b. Once the simulation is complete, the energy by position data is copied and exported from CASINO and imported into Matlab. The copied data provides the x/z positions of the energy distribution intensity while the exported data contains the mesh information and is used to create a corresponding mesh in Matlab (see 2.11c). In this case, 10^4 trajectories was sufficient to obtain the energy distributions. The $(x, energy)$ data is then fit to a Gaussian at every z division. For example, slices at the top, middle, and bottom of the beam are shown and fit in 2.11d and e. From these fits, the spread parameter and the strength parameter are plotted as a function of z.

The results from the CASINO fits for 200 and 100 kV are shown in Figures 2.12 and 2.13. As expected, at 200 kV the beam remains highly collimated for the first 2000 nm. At 100 kV, the beam remains fairly collimated for the first 1000 nm, but then begins to spread out gradually. These results reiterate an important point about the accelerating voltage. Below 100 kV, the beam will spread out rapidly since the electrons do not have enough forward momentum to penetrate deep into the specimen. For generation volumes typically used to describe SEM voltages, αz is replaced with αz^2 or another dependence.

Based on the results from the linear approximation, shown in Figure 2.14, an α of 0.01 and 0.1 were used for 200 an 100 kV, respectively. The effect of α on the simulated EBIC profile is discussed in Section 2.5.4.

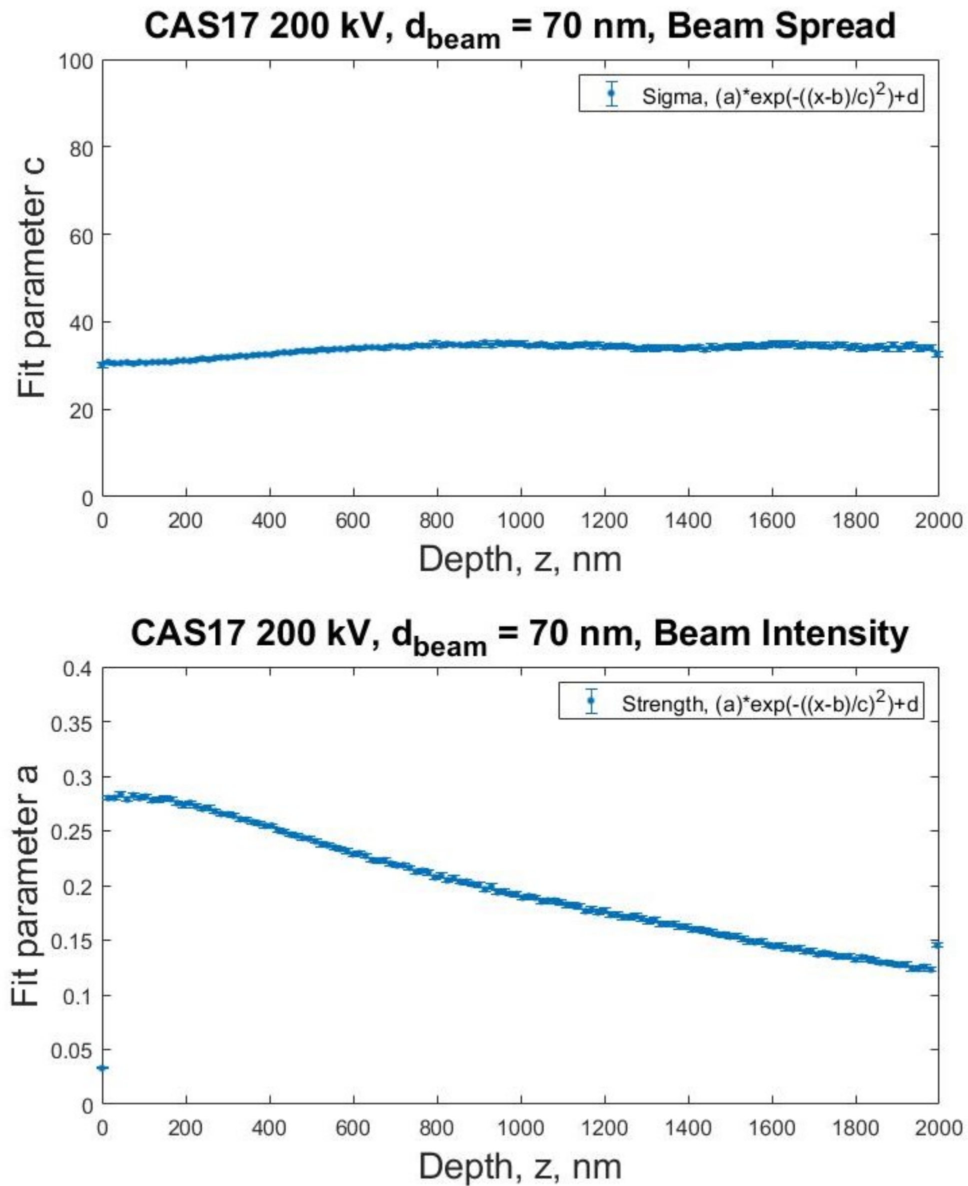

Figure 2.12: Top figure shows width of Gaussian from Figure 2.11e, as a function of depth, z (no broadening). Bottom figure shows the energy density vs depth.

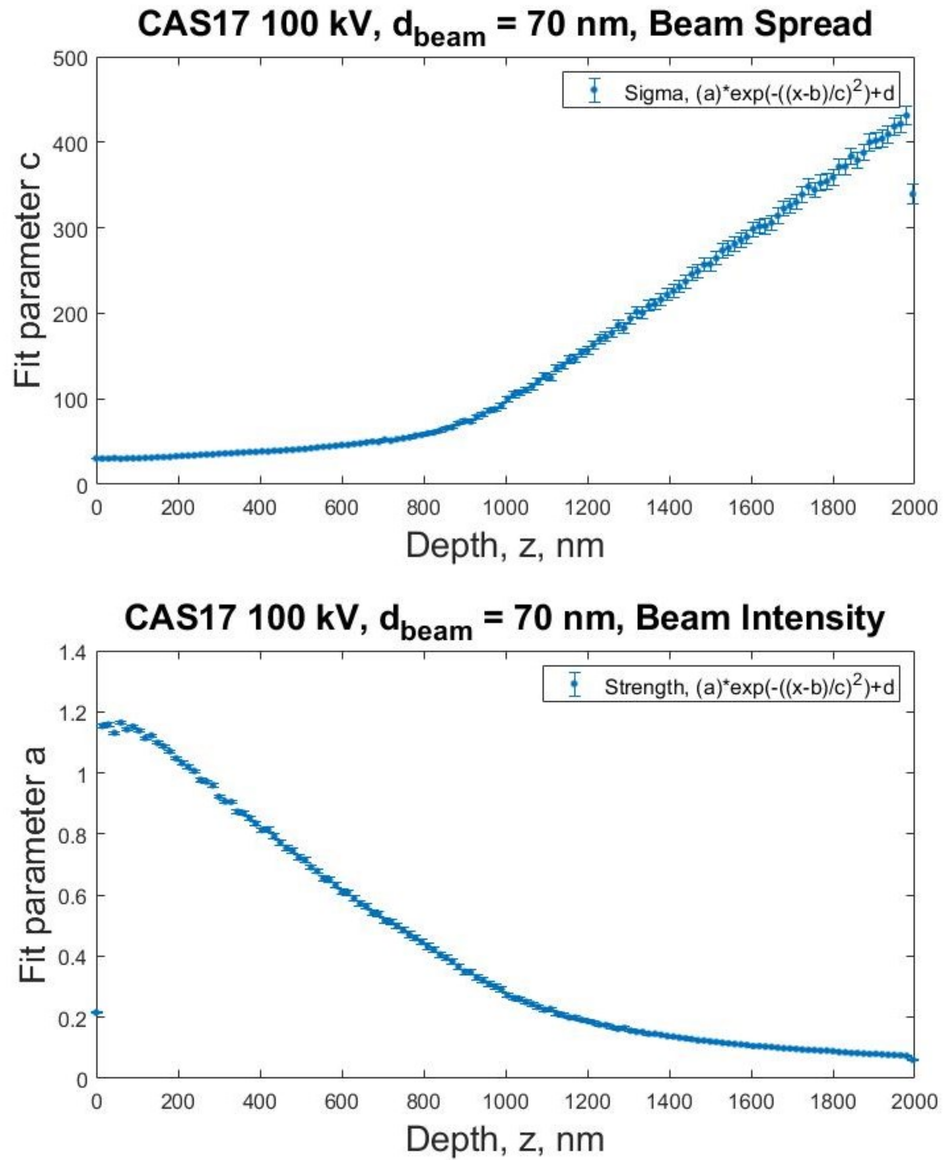

Figure 2.13: Top figure shows that the beam does not remain as collimated for 100 kV as it does for 200 kV, since the width of the Gaussian spreads out as z increases.

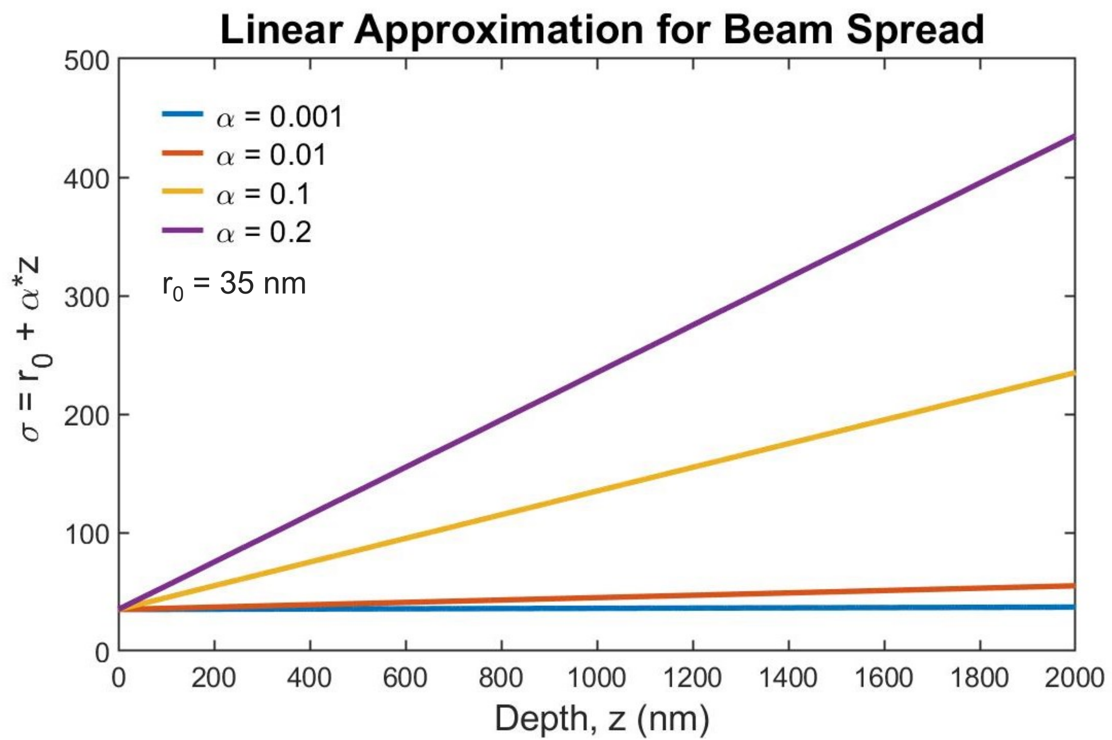

Figure 2.14: Comparing top figures from 2.12 and 2.13 to the linear approximation fo beam spread, an α of 0.01 and 0.1 were chosen for 200 and 100 kV, respectively.

2.5.3 Integration Limits

The integration limits in Equation 2.2 are set by the planar geometry of the problem. In this case, the beam is being rastered in the x direction, which is why the predicted I_{EBIC} is plotted with respect to the distance from the edge of the Schottky contact, x_0. Since the geometry is symmetric with respect to y, the limits are from $-\infty$ to $+\infty$. Lastly, only the charge carriers which can diffuse to the depletion region are considered collected current, which sets the limits of integration for z to be from the depletion width, W_{dep} to 0. Technically this is the depletion region *depth*, since the Schottky contact is planar.

To determine the appropriate W_{dep}, consider the Ni/n-GaN (metal/semiconductor) contact. Figure 2.15 shows a energy band diagram for an ideal metal/n-type semiconductor contact, where the work function of the metal is larger than that of the semiconductor, $\Phi_M > \Phi_S$. In this case, the Schottky barrier is equal to the difference in the metal work function and the semiconductor electron affinity, $\Phi_B = \Phi_M - \chi$. For Ni/GaN, this difference is 5.1 - 4.1 = 1.0 eV. The built-in potential, V_{bi} felt by electrons in the semiconductor trying to enter the metal is the difference between the two work functions, $V_{bi} = \Phi_M - \Phi_S$.

The loss of electrons from the n-type semiconductor to the metal creates a depletion region, x_n or W_{dep}, or space charge region (SCR) in the n-type semiconductor. The size of the depletion region can change by applying an external voltage, V_A, which either enhances or reduces the size of the intrinsic electric field. It can be shown that the ideal equation for the depletion region is given by [5]:

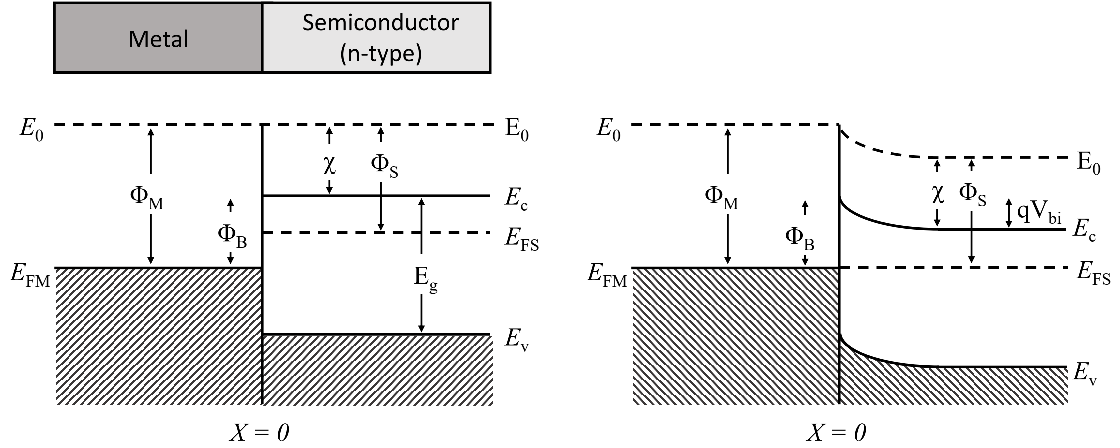

Figure 2.15: Metal-Semiconductor Schottky barrier energy band diagram (a) at initial contact and (b) after reaching thermal equilibrium. $\Phi_B = \Phi_M - \chi$ is the barrier felt by electrons in the metal trying to enter the semiconductor, and $qV_{bi} = \Phi_M - \Phi_S$ is the barrier felt by electrons in the semiconductor trying to enter the metal.

$$W_{dep} = \sqrt{\frac{2\varepsilon_s\varepsilon_0}{qN_D}(V_{bi} - V_A)} \tag{2.10}$$

which, under no bias and for $\varepsilon_s = 9$ [3], $N_D = 10^{16}$, [98], $V_{bi} \approx \Phi_B = 1.0$ eV, gives a value for the depletion region of approximately 300 nm.

2.5.4 Numerical Simulation Results

With equations for the EHP generation volume 2.9 and the subsequent diffusion and recombination 2.8, the convolution (2.2) can be solved and the predicted $I_{EBIC}(x_0)$ compared to experimental EBIC profiles. A closed form analytical solution is not necessary; instead a discrete mesh evaluation of the convolution is per-

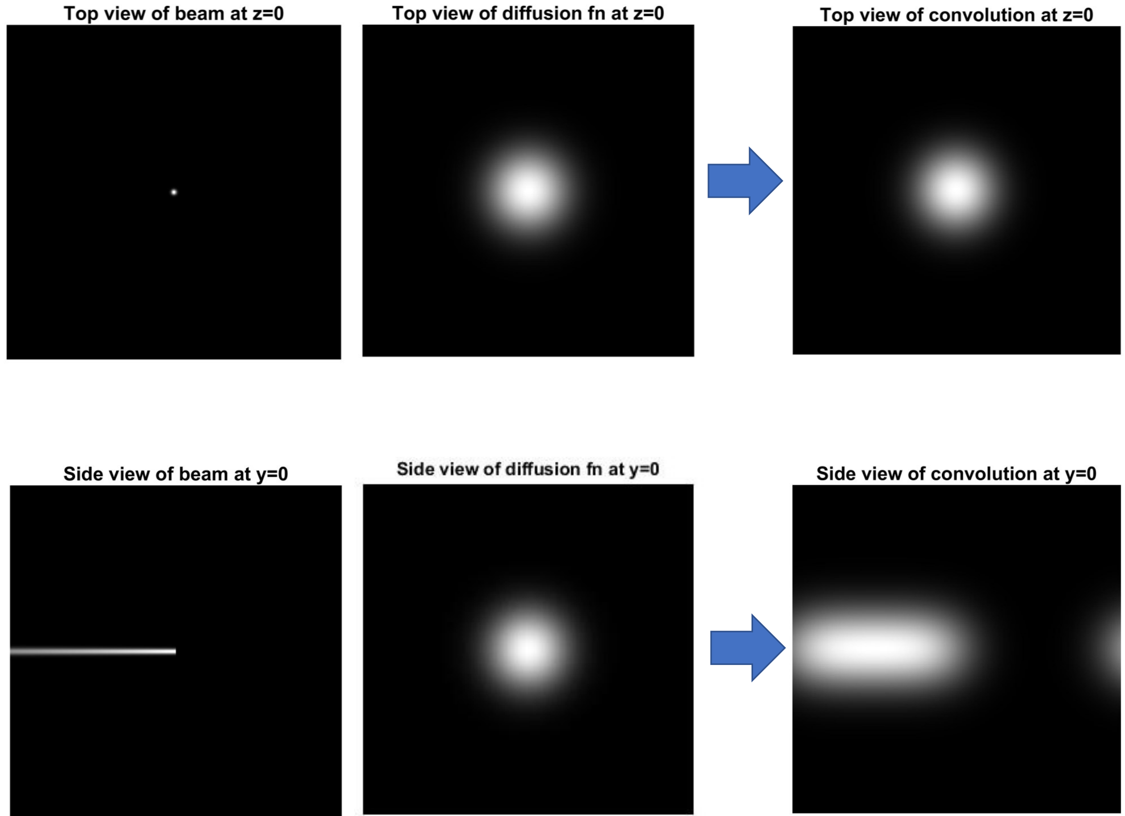

Figure 2.16: In-plane cross sections of the distribution profiles for the generation volume (beam), the diffusion volume, and the subsequent convolution of the two.

formed using fast fourier transform (FFT) analysis. Essentially, the diffusion equation is used as the kernel with respect to the generation volume, producing a convoluted beam-diffusion distribution, shown in Figure 2.16. The predicted $I_{EBIC}(x_0)$ is then determined by numerical integration of the distribution over the depletion region (W_{dep}) to determine $I_{EBIC}(x_0)$, where again x_0 is the scan raster direction. This is shown in Figure 2.17a. Details of the code can be found in Appendix B.

Once the data is simulated, it is then fit using an erfc, shown in Figure 2.17b. In this example, the input was L_p = 200 nm, and the fit result L_p = 1/(sqrt(2)*b)

= 202.6 nm. The effect of changing the input parameters L_p, α, d_{beam}, and W_{dep} are explored in Figures 2.18 and 2.19. For the most realistic parameters, $\alpha = 0.01$, $d_{beam} = 70$ nm, and $W_{dep} = 240$ nm, the fit diffusion length is equal to the input diffusion length with 1% numerical error.

More specifically, $\alpha < 0.5$ does not significantly change the fit diffusion lengths (see 2.18b) which is expected. This is because the interaction volume is dependent on the incident beam energy (see Section 2.4), while the minority carrier diffusion length is a fundamental property of GaN. This is confirmed in the results from the numerical simulation, which show that the simulated EBIC profile does not depend on the accelerating voltage. An $\alpha > 0.5$, is not physically relevant for STEM, however, it does shed light on the potential pitfalls of SEM accelerating voltages.

In the case of the input beam diameter, d_{beam}, the beam diameter does affect the fit diffusion length (see 2.19a), particularly when the input diffusion length is on the smaller end, when $d_{beam} \approx L_p$. Again, this makes sense, and runs into the same problem at SEM accelerating voltages, where the two are on the same order of magnitude.

Lastly, the depletion width (depth) does not impact the output diffusion length, (see 2.19b). The depletion width will affect the maximum current collected, which is then normalized. However, in this approximation the depletion width is a simple rectangle approximation. Since this is not exactly the correct physical form of the depletion region, the model is slightly limited in this respect. Further limits of the model are explored in the next section.

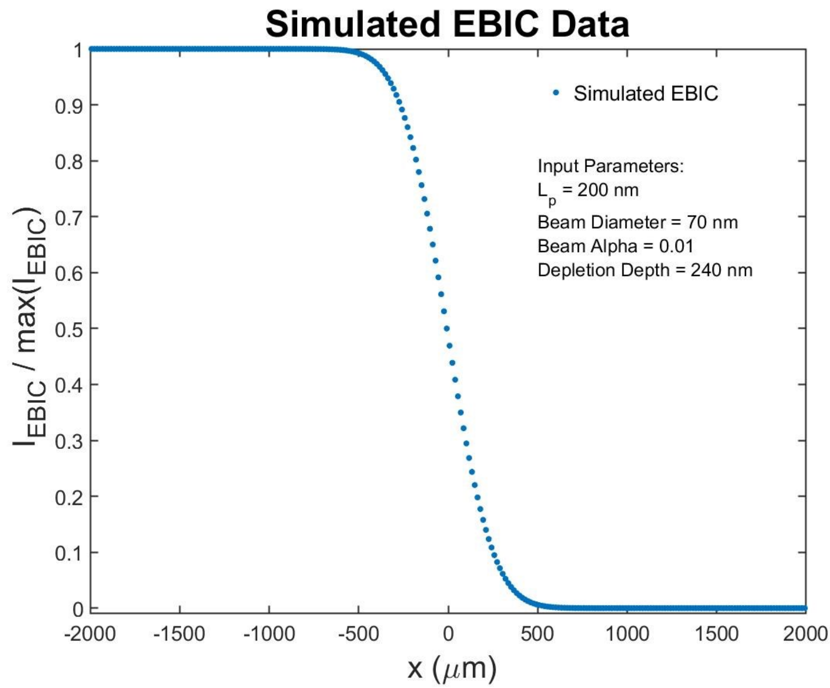

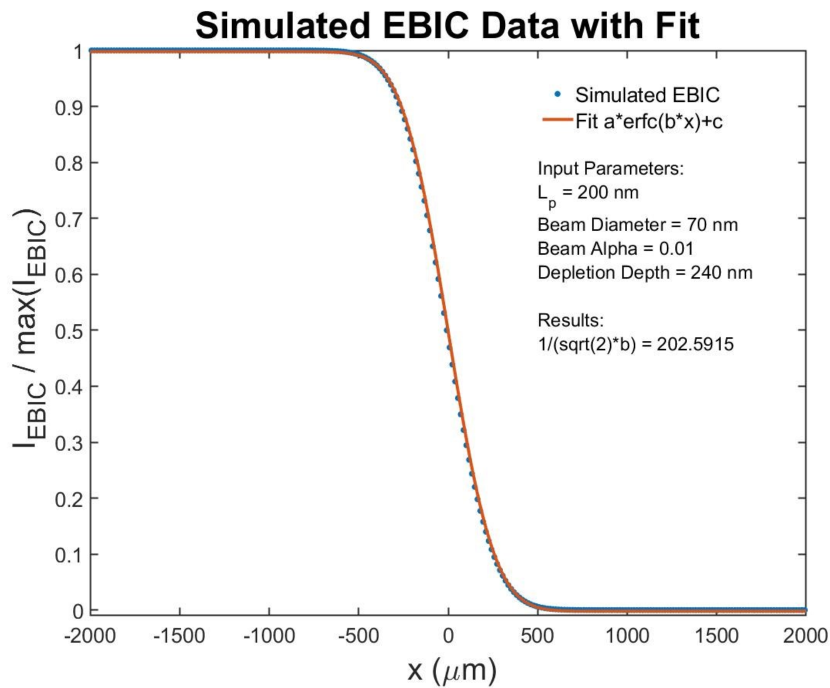

Figure 2.17: Top figure shows the simulated EBIC data, which qualitatively looks similar to measured EBIC profiles. Bottom figure shows erfc fit of simulated data.

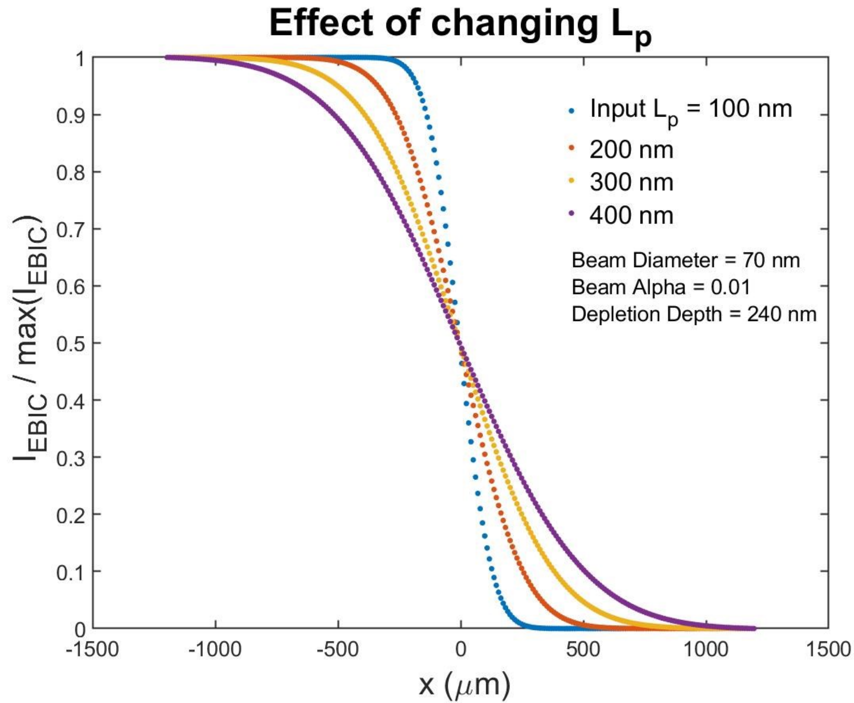

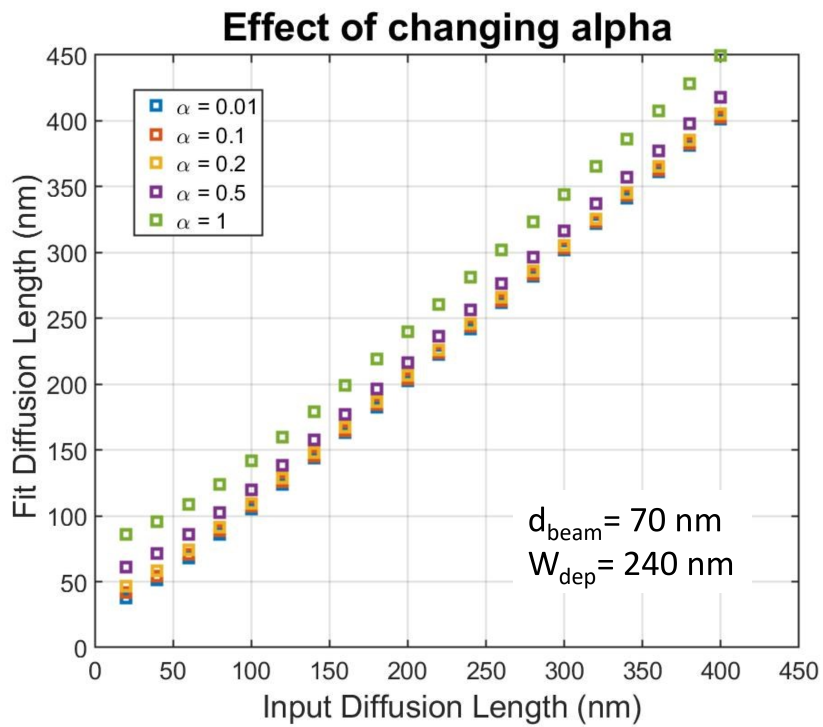

Figure 2.18: Top figure shows the change in expected EBIC profile for materials with differing diffusion lengths, while keeping all other parameters constant. Bottom figure plots input diffusion length vs fit diffusion length for several different choices of α, while keeping other parameters constant.

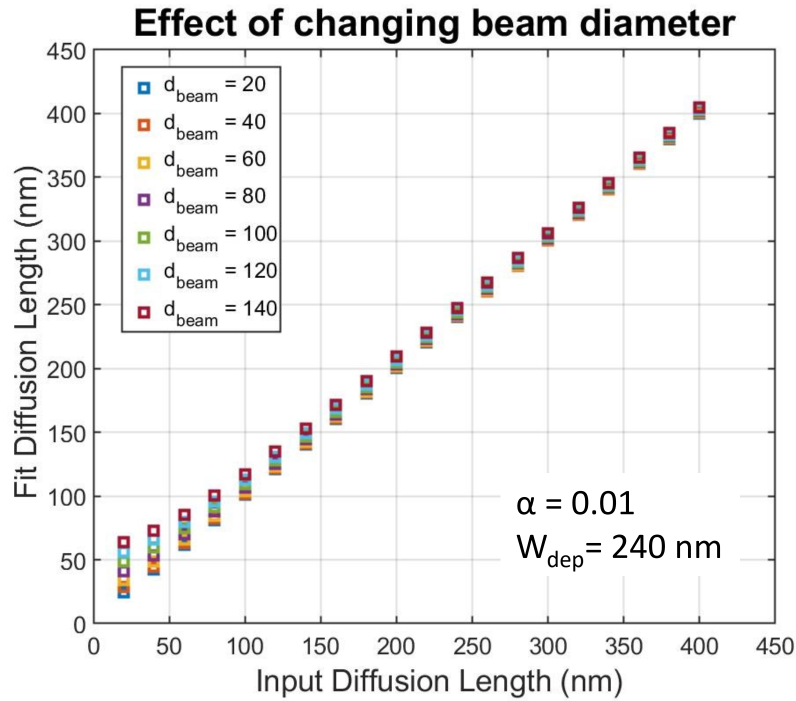

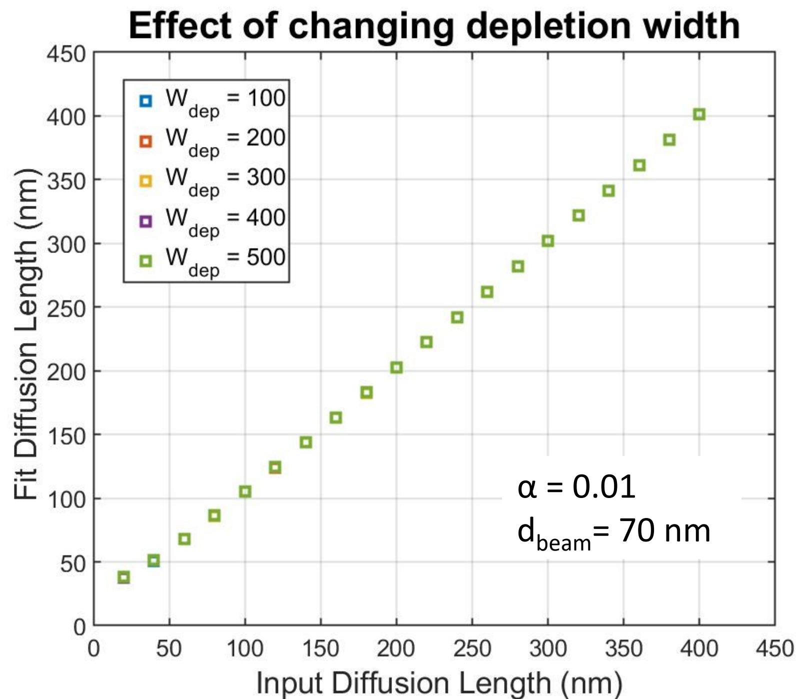

Figure 2.19: Top figure plots input diffusion length vs fit diffusion length for several different choices of input beam diameter, while keeping other parameters constant. Bottom figure shows similar results for depletion width.

2.6 Experimental bulk STEM EBIC results

As shown in Section 2.5, the simple erfc is sufficient to analyze the simulated EBIC linescans of a high energy electron beam incident on a bulk planar Schottky junction. The erfc model was used to fit the simulated EBIC profiles in order to accurately measure the minority carrier diffusion length, L_p, where $L_p = 1/(\text{sqrt}(2)\text{*b})$. We now discuss the results of using this model to analyze experimental EBIC linescans collected via bulk STEM EBIC technique. Again, this analysis is performed on linescans after the background BSE signal has been subtracted (see Figure 2.8).

An example of the analysis is shown in Figure 2.20, for an EBIC linescan acquired at 200 kV 15 kx. In this case the erfc fit does not fit the experimental data as well as expected. For all linescans analyzed in this work, the fit consistently underestimates the experimental data when $x_0 > 0$. This difference is most likely due to the approximation that the depletion region is a perfect rectangle, which is not a true physical representation of the electric fields present at the junction. [99]

Results for L_p from the same experimental EBIC linescans analyzed in Section 2.4 are tabulated in 2.2. Based on these results the diffusion length is around 250 nm, which is consistent with measurements of these same specimens acquired through traditional SEM depth dependent analysis. [98] However, there is a significant spread between the reported values. This difference is attributed to electron beam damage and is explored in the next Chapter.

E (Magnification)	L_{LR}	L_p
200 kV (15 kx)	36.2 ± 1.0 μm	258 ± 11 nm
100 kV (15 kx)	6.7 ± 1.0 μm	271 ± 8 nm
200 kV (5 kx)	30.0 ± 0.5 μm	238 ± 12 nm

Table 2.2: Minority carrier diffusion length results

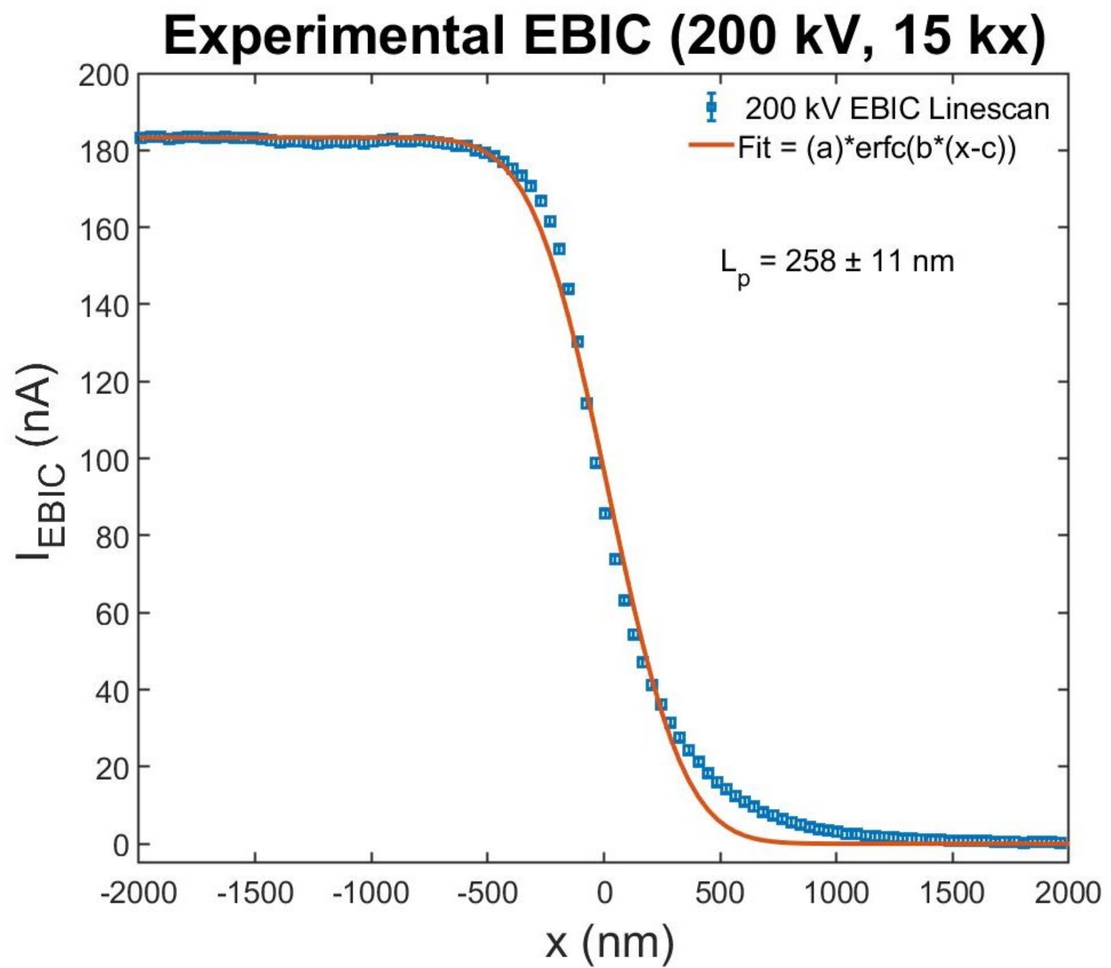

Figure 2.20: EBIC linescan acquired at 200 kV 15 kx. $L_p = 258 \pm 11$ nm.

Chapter 3: In-situ Bulk EBIC

3.1 Electron Beam Irradiation of GaN

3.1.1 Evidence of electron irradiation damage to GaN

Typically, the minority carrier diffusion length is consistent within a single EBIC micrograph (see section 2.3.3). However, as illustrated in Figure 3.1, sometimes there can be a wide range of L_p in a single micrograph which can not be attributed to the resolution of the technique. For example, 3.1 was collected after several higher magnification images were collected, the outline of the scanned areas can be seen on the Ni side. Qualitatively, the imprint of the higher magnification scans can be seen and suggests evidence of carbon contamination at the very least. Quantitatively, several different linescans were analyzed, and the minority carrier diffusion length, L_p, is smaller for areas which appear to have damage. This large difference in L_p suggests that the previous scans at 200 kV caused permanent damage to the Ni/GaN junction which caused the carrier lifetime and diffusion length to decrease.

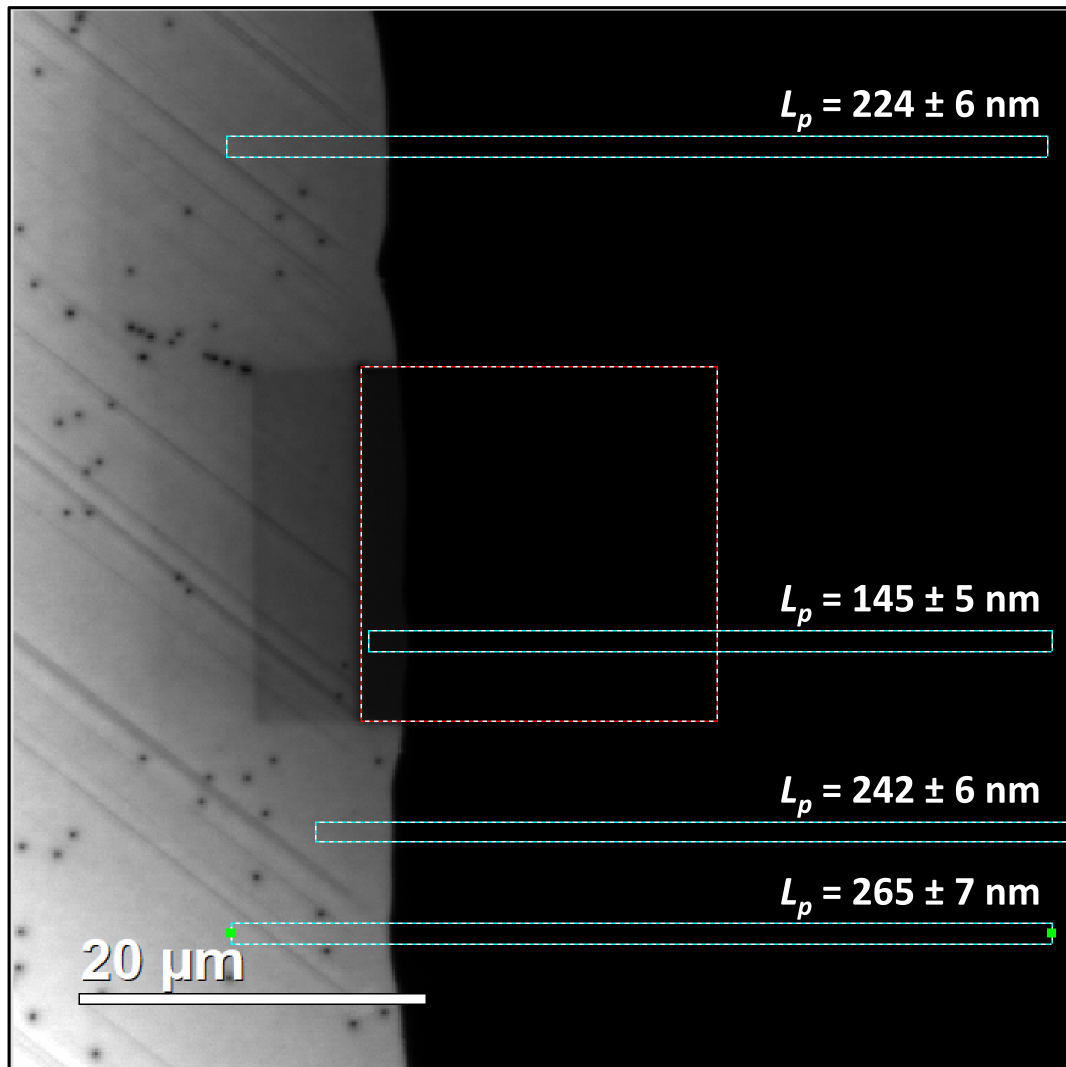

Figure 3.1: EBIC micrograph collected at 200 kV, 5kx showing evidence of electron beam damage. Each linescan was analyzed using the methods discussed in Chapter 2, and the resulting L_p for each is shown above its corresponding linescan.

3.1.2 Beam Current Measurements

In order to quantify the beam damage to the specimen during EBIC measurements, we must first estimate the total current imparted from the beam to the specimen. The JEOL phosphor screen detects and reports a current density, however this number is not calibrated to the electron gun. Traditionally, a Faraday cup would be used to capture all the electrons (incoming, SE, BSE, etc), and could be used to calibrate the screen current; [100] this is common in SEM systems but not available in our TEM. To overcome this, we use the JEOL 2100 F electron energy loss spectrometer (EELS) detector to measure the beam current, as described by Mitchell and Carrow. [101] In the typical EELS operating mode, incoming electrons pass through a drift tube, in which a magnetic prism bends the trajectory so that the electrons can be detected by the Gatan Image Filter (GIF). For our beam current measurements, we turn off the magnetic prism, which causes the incoming electrons to impinge on the wall of the drift tube. We measure this current by coupling the drift tube safe high voltage (SHV) cable to our external picoammeter. A Keithley 617 Electrometer was used to measure the beam current with 1 pA tolerance.

To measure the beam current in transmission mode, we adjust the condenser lenses (brightness knob) to condense the beam to a spot that is small enough to pass through the drift tube entrance aperture (5 mm) using the shift knobs. For STEM measurements, the pre-specimen lenses focus the beam to a spot on the specimen plane, so that by the time the beam reaches the phosphor screen, it has spread. This spread is so large in STEM Low Mag mode that the brightness knob is

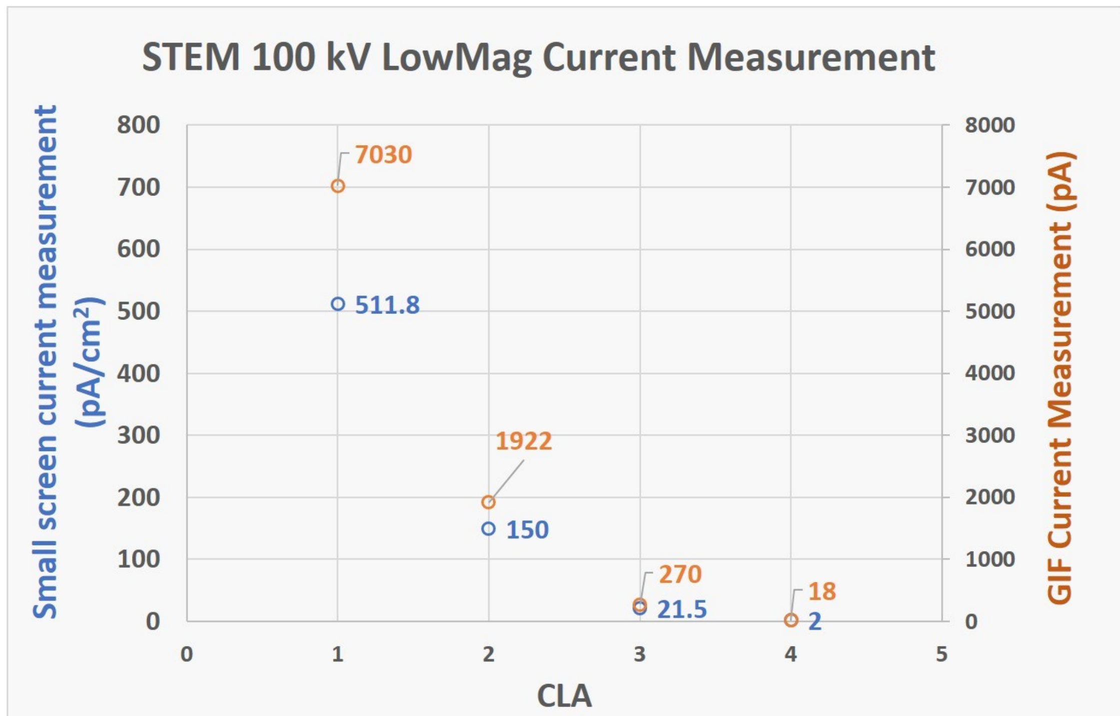

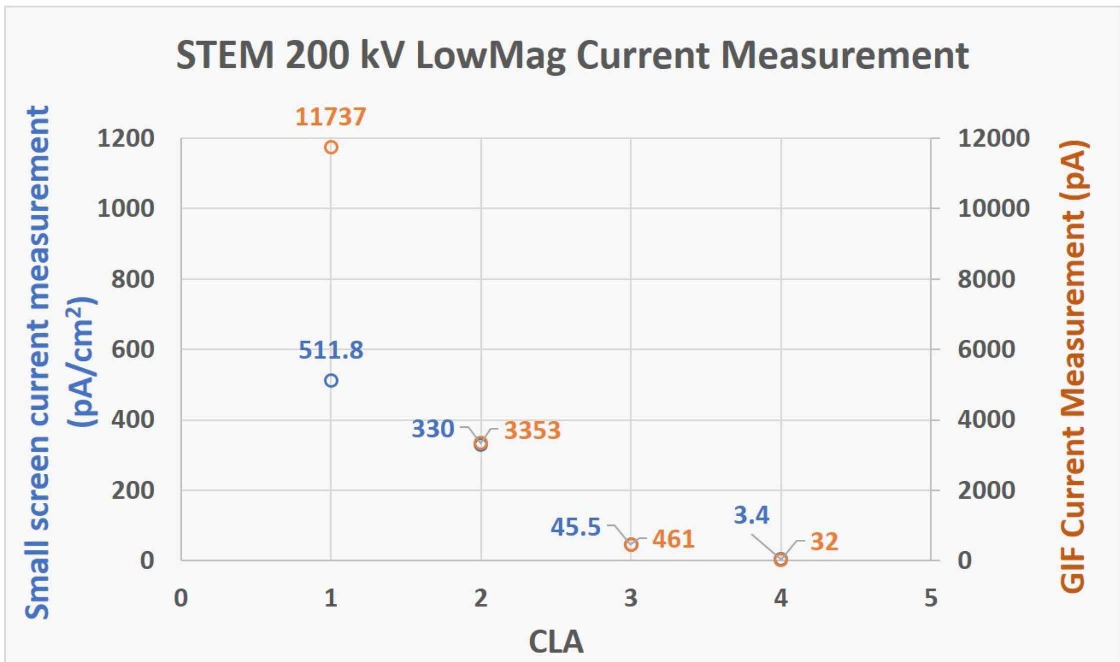

Figure 3.2: STEM Beam Current Measurements for different condenser lens apertures (CLA) correlating screen current reading to the actual (GIF) current.

insufficient to condense the spot to pass through the 5 mm entrance aperture of the drift tube, thus not all of the electrons will be collected. To correct this error, we use free lens control mode to adjust the post-specimen lenses to condense the beam to pass through the drift tube entrance aperture. Specifically, we use intermediate lens 2 (IL2) to condense the spot while the first condenser lens aperture (CLA 1) is inserted, since this is the largest condenser aperture. The same IL2 setting can then be used for CLA 2-4 because the smaller apertures will produce an even smaller spot size, all of which will easily pass through the entrance aperture. Figure 3.2 reports the STEM Low Mag beam current measurements for both 100 and 200 kV. The correction factor was determined to be 10 cm^2. Note that the screen current measurement for CLA 1 were 511.8 pA cm^{-3} for both 100 and 200 kV, while the GIF current measurements were 7030 pA and 11737 pA, respectively. This suggests that the screen cannot detect a current density higher than 511.8 pA/cm3, however, this should not be an issue for most users, since CLA 1 is rarely used to form the STEM probe. For the work in this dissertation, either CLA 2 or 3 was used for EBIC imaging.

To calculate the dose rate and total dose imparted during a single STEM image, we consider the beam current, pixel size, image size, and scan speed:

$$\dot{d} = \frac{I/q}{Area} = \frac{(3.3 \times 10^{-9}\ C/s) \times (1.602 \times 10^{-19}\ e/C)}{512^2 \times (400\ \text{Å})^2} = 0.491\ e/\text{Å}^2 s \tag{3.1}$$

$$total\ dose = \dot{d}\ \times\ (32 \times 10^{-6})\ \times\ 512^2 = 4.12\ e/\text{Å}^2 \tag{3.2}$$

3.1.3 Electron Irradiation Data Collection

One advantage of the bulk STEM EBIC technique is that one can study the effect of hundreds of keV electrons on homoepitaxial GaN. An accumulated dose effect of 200 keV electrons at $\sim 10^{16}$ cm^{-2} was studied by acquiring consecutive scans of the same area. Figure 3.3 shows the Ni/GaN junction micrographs and accompanying linescans which were used to analyze the effect of beam damage on the specimen. The beam was blanked between each image acquisition so that no additional damage would occur between images. The linescans show that the long range scattering length, L_{LR} does not change. There is a noticeable decrease of the maximum current on the Ni side of the junction. Also, the short decay length becomes more narrow, reflecting a decreasing minority carrier diffusion length in each image. It is important to note that there is always carbon contamination and carbon deposition on the surface of the specimen during image acquisition (see Ni in Figure 3.1). However, this EBIC technique is measuring sub-surface minority carrier behavior, not surface behavior. Furthermore, if the EBIC decay signal was due to surface effects, then one would expect the short decay length to broaden, since the carbon would scatter the electrons more and broaden the edge, but we observe that the short decay length narrows. Each subsequent dose image was analyzed by the methods discussed in Chapter 2. An example of the background fitting and subtraction followed by the erfc fitting is shown in Figure 3.4.

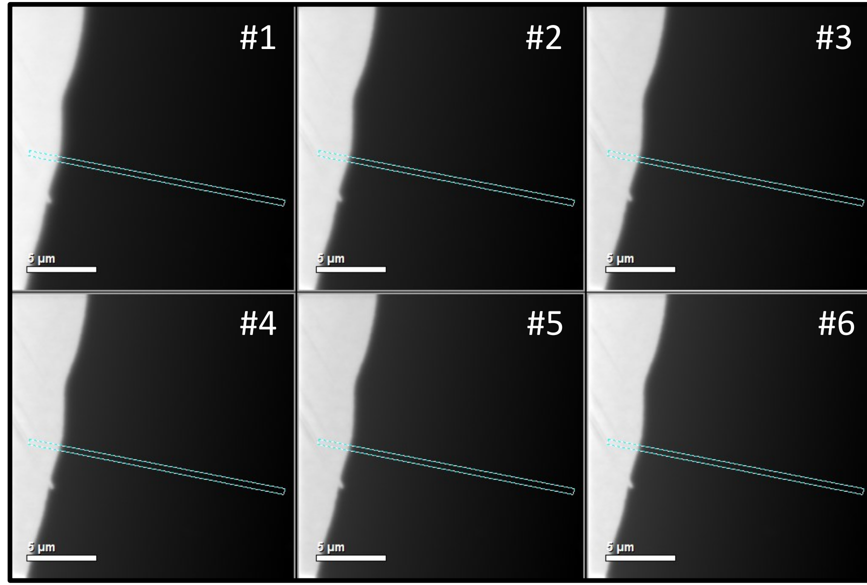

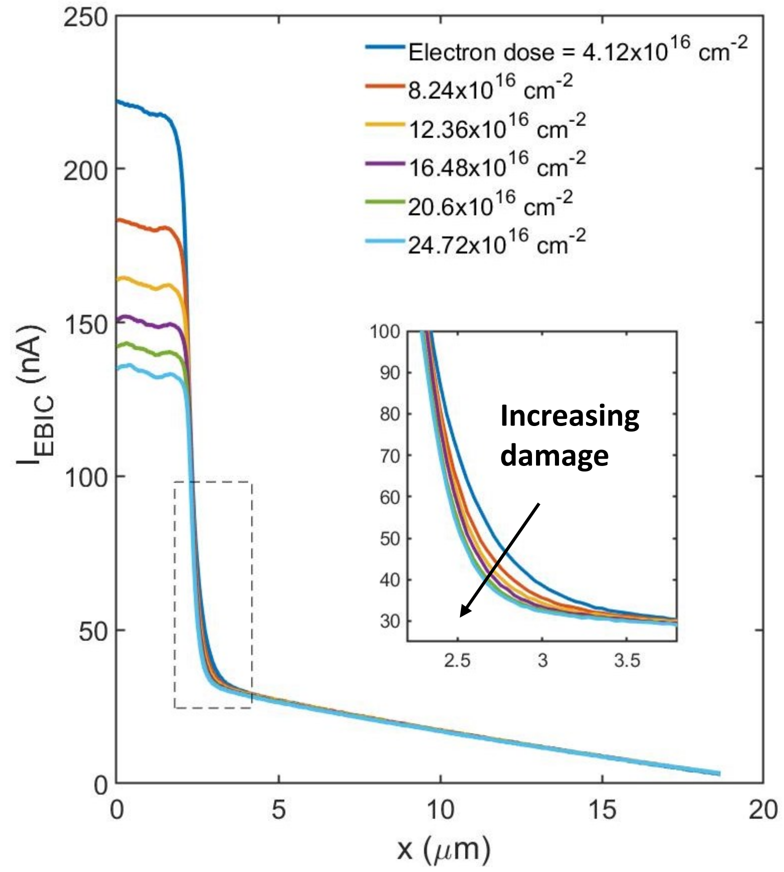

Figure 3.3: EBIC micrographs of the same area collected consecutively under same operating conditions. Linescans show evidence of accumulated electron beam damage.

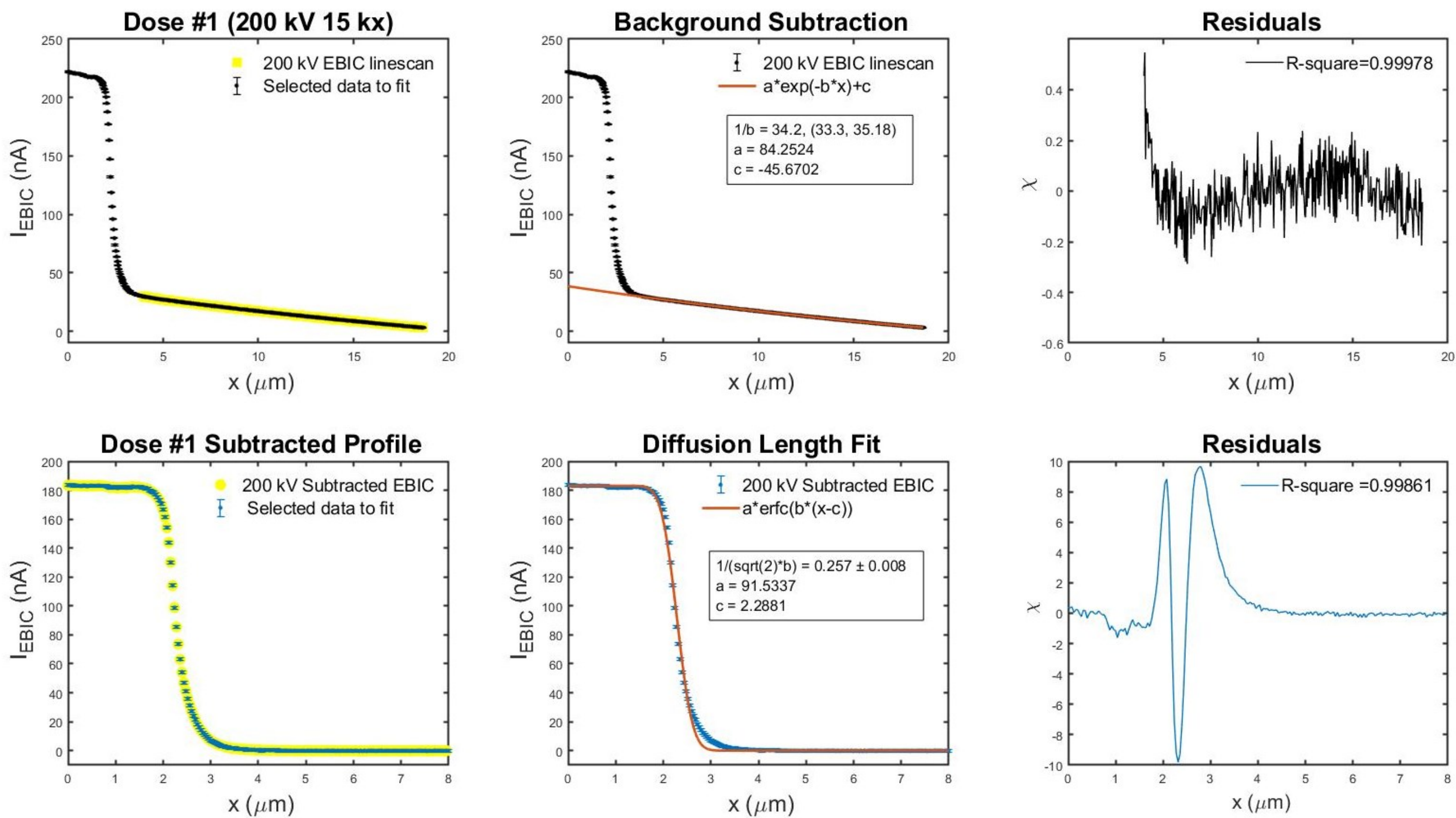

Figure 3.4: Example of analysis of Dose #1 from 3.3.

3.1.4 Electron Damage Results

The electron damage analysis results are summarized in Figure 3.5, showing that the accumulated dose only reduces the minority carrier diffusion length, L_p, and has no effect on the interaction volume long range scattering length, L_{LR}. An approximate 35% decrease in L_p was observed, corresponding to a $\sim$ 2.5x increase in point defect density, assuming $N_D \propto L_p/2$. [98] This is consistent with previous calculations for the onset of knock-on damage to be 100 keV for the N sublattice. The creation of V_N and N_i Frenkel pairs by irradiation of electrons at 0.7 MeV [102] has been previously observed, estimating an atomic displacement energy, E_d of 10.8 eV for N. However, knock-on damage to the Ga sublattice can not be ruled out entirely. While a previous study by Ionascut-Nedelcescu *et al.* did not observe knock-on damage to Ga until an onset voltage of 433 keV, the active layer in their configuration was buried beneath 25 microns. [14] The lack of observed device degradation may have simply been due to inactive layer stopping an electron beam $<$ 400 kV before it reached the active layer.

There are two main categories of electron radiation damage: (1) atomic displacement (knock-on) damage, caused by the small fraction of electrons which pass close enough to an atomic nucleus to be scattered through large angles and suffer appreciable energy loss and (2) ionization damage (radiolysis) caused by the large fraction of electrons which scatter inelastically and suffer energy losses between a few eV to tens or hundreds of eV.[103] While the damage rate of the minority carrier lifetime $\tau \propto L_p^2$ with increasing dose follows an inverse relationship, and can

therefore not be explained with a direct relationship to determine a lifetime damage constant [13, 104] this is attributed to the time dependence of damage rather than any inherent nonlinearity in the response. [103] Further investigations at both 100 and 200 kV are necessary to make a more compeling argument for knock-on damage to the N sublattice.

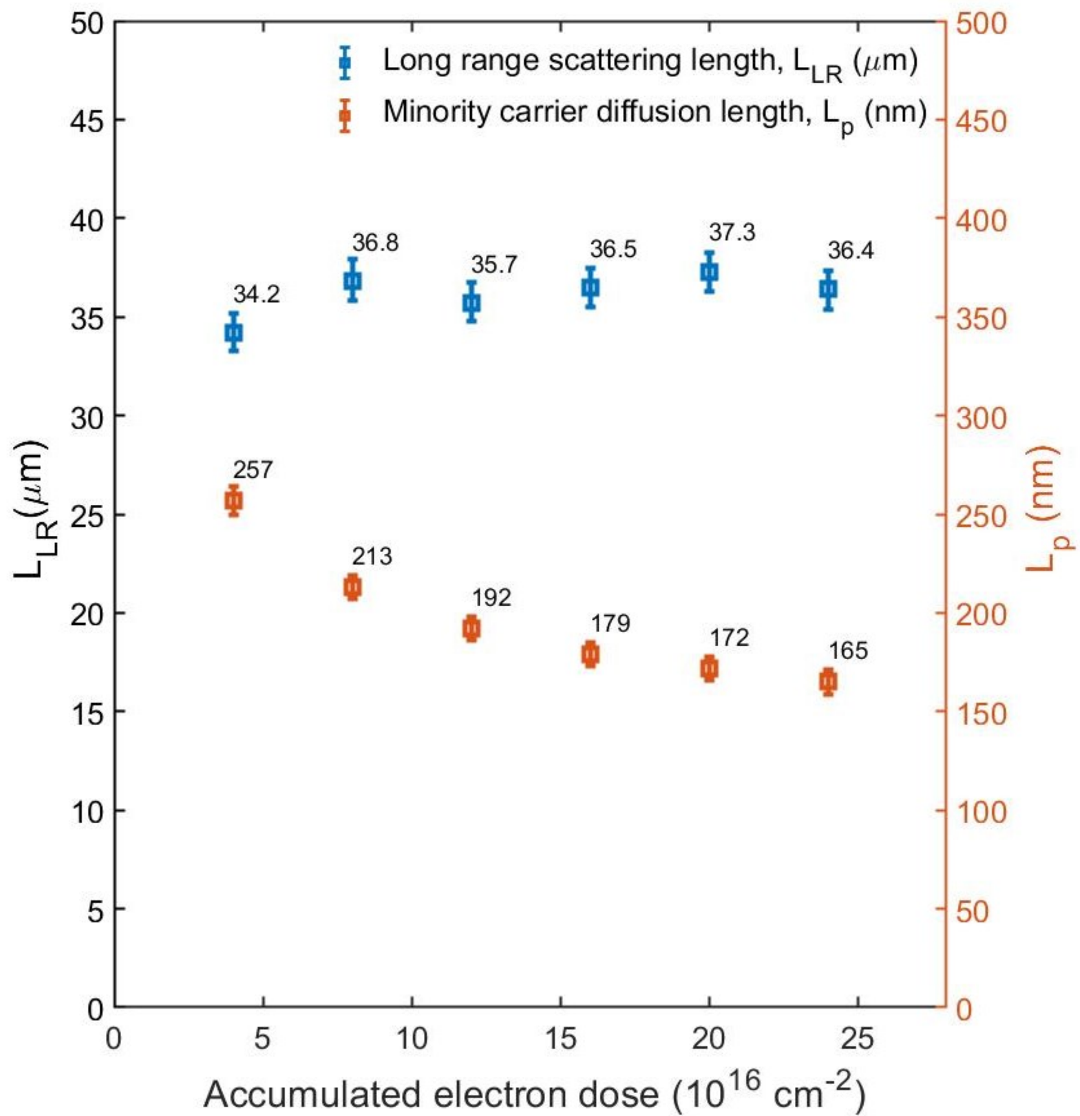

Figure 3.5: Results from accumulated electron dose effect on both the long range scattering length as well as the minority carrier diffusion length.

3.2 In-situ Reverse Biasing

When a reverse bias, V_A, is applied to a Schottky junction, the energy barrier experienced by electrons in the n-type semiconductor becomes larger. One consequence of this is an increase in the size of the depletion region, x_n or W_{dep}, as described in equation 2.10. The theoretical effect of an increasing reverse bias on the depletion region of a Ni/GaN junction is shown in Figure 3.6 for varying donor concentrations. For samples with lower doping concentrations, a large bias could induce enough depletion region growth to be observed via bulk STEM EBIC.

In order to collect the reverse bias data, an external high voltage power supply was used to apply a voltage to the specimen, by coupling the supply to the current head (which was previously grounded for no-bias EBIC images). An EBIC image was collected while at a corresponding voltage, then the beam was immediately blanked and kept blanked while ramping up to the next voltage, and then unblanked to collect the next image. Practically, the GaN bulk specimens are still high-voltage devices since no thinning was done, however these samples were not biased to more than -30 V because we were also imaging with the electron beam at the same time and did not want to induce early breakdown. Initially, reverse biasing data was only collected at 200 kV. However, once 100 kV data collection became more regular, we were able to collect biasing data at both 100 and 200 kV for the same specimen.

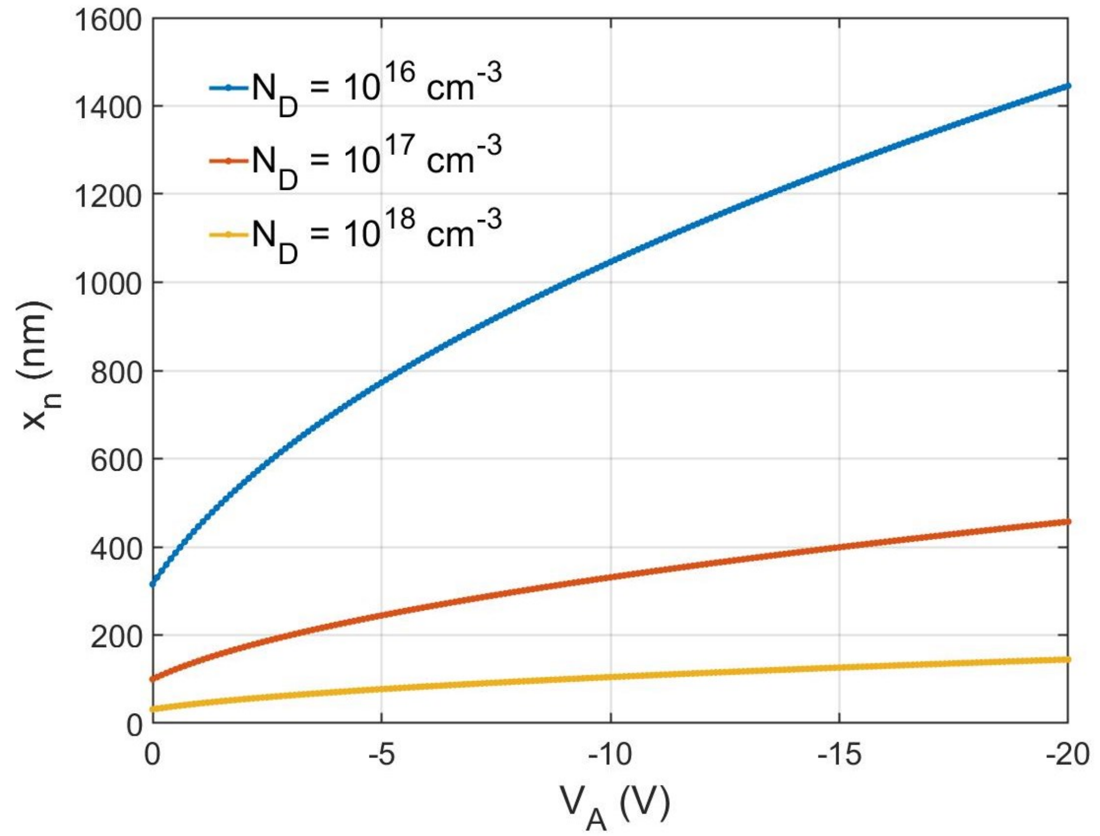

Figure 3.6: Expected growth of the depletion region in a Ni/GaN junction for various N_D ($V_{bi} = 1.0$ eV, $\varepsilon = 9$).

3.2.1 Data Analysis and Results

The reverse biasing EBIC micrographs collected at 100 kV are shown in Figure 3.7 and linescans in 3.8. Overall there is an increase in current intensity as the reverse bias is applied. There are also two bright spots that start to appear around -10 V, which were avoided when choosing where to select linescans to analyze. As shown in 3.8, the characteristic Schottky junction decay profile grows with increasing voltage. Both the amount of current and the distance from the initial Ni-GaN edge increase, the latter corresponding to a growth of the depletion region. The 100 kV data was analyzed by taking the numerical derivative of each line and fitting to a Gaussian distribution. The center of the Gaussian fit was chosen to represent the "edge" of the depletion region, which shifted with each increase in voltage. The line of the depletion region edge squared to the applied voltage was fit using equation 2.10, as shown in the inset of 3.8. From the fit, we estimate a built-in voltage, $V_{bi} = 1.685$ V, doping concentration, $N_D = 3 \times 10^{16}$ cm^{-3}, and $W_{dep}(V_A = 0) = 244$ nm.

The reverse biasing EBIC micrographs collected at 200 kV are shown in Figure 3.9 and linescans in 3.10. Instead of individual spots becoming brighter, the entire Ni edge becomes brighter at around -15 V. These bright edges appear to be due to avalanche effects. The combined effect of a large reverse bias and high energy electron beam cause uncontrolled multiplication of electron hole pairs, which leads to an extremely large collected current. This effect has been observed in other GaN devices, [105] where the edge termination of the diode was determined to be the cause of the onset of avalanche breakdown.

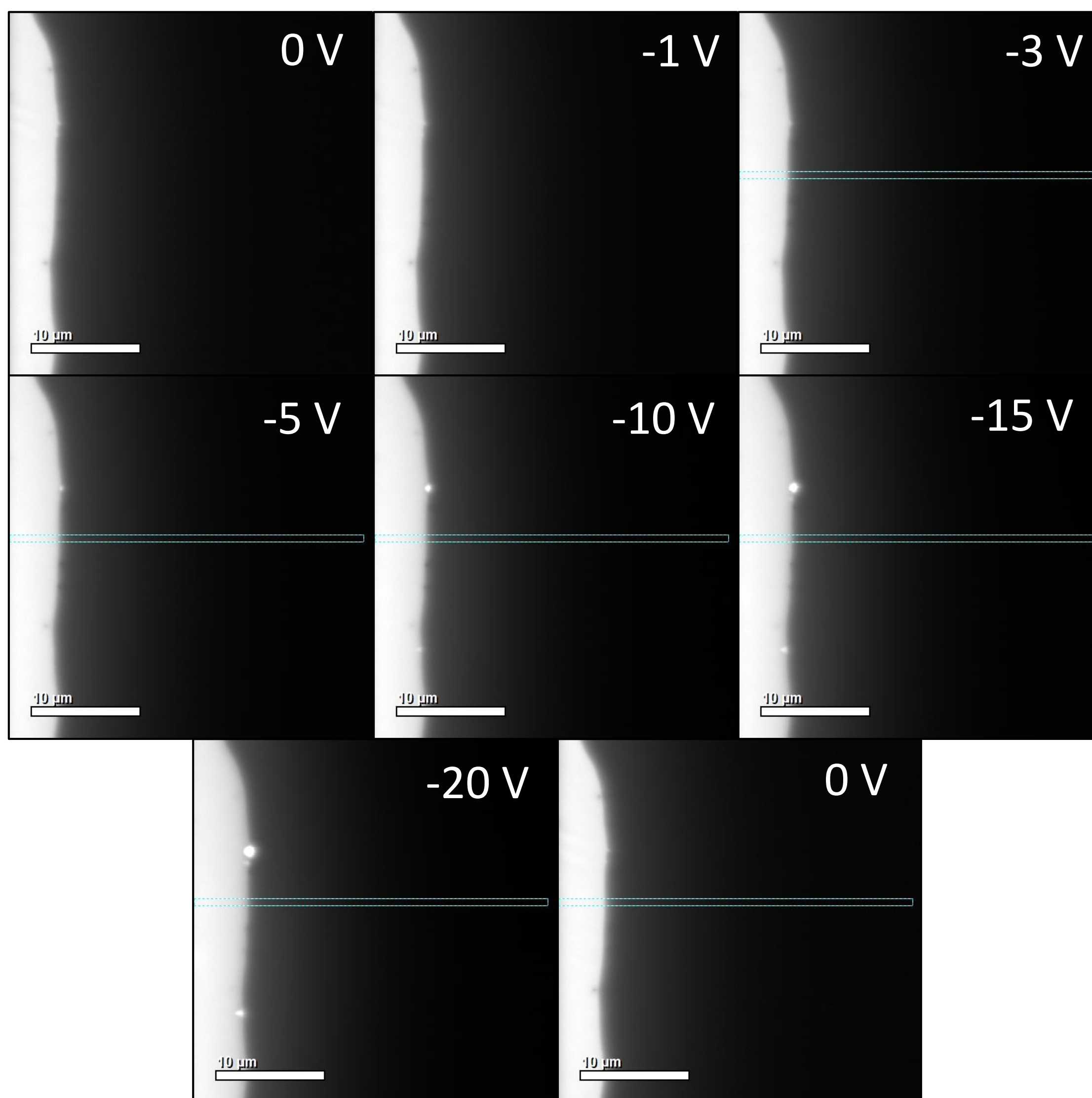

Figure 3.7: In-situ reverse biasing of Ni/GaN Schottky junction at 100 kV.

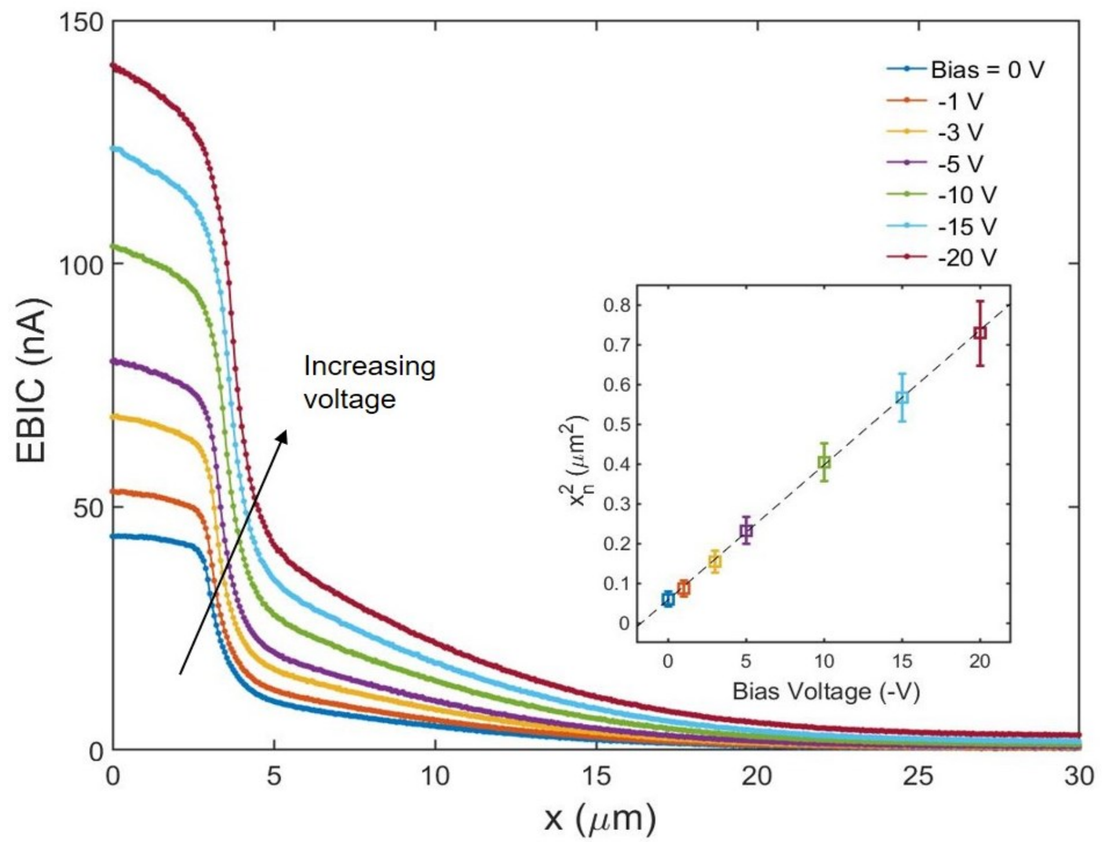

Figure 3.8: Linescans of reverse biasing of Ni/GaN Schottky junction at 100 kV.

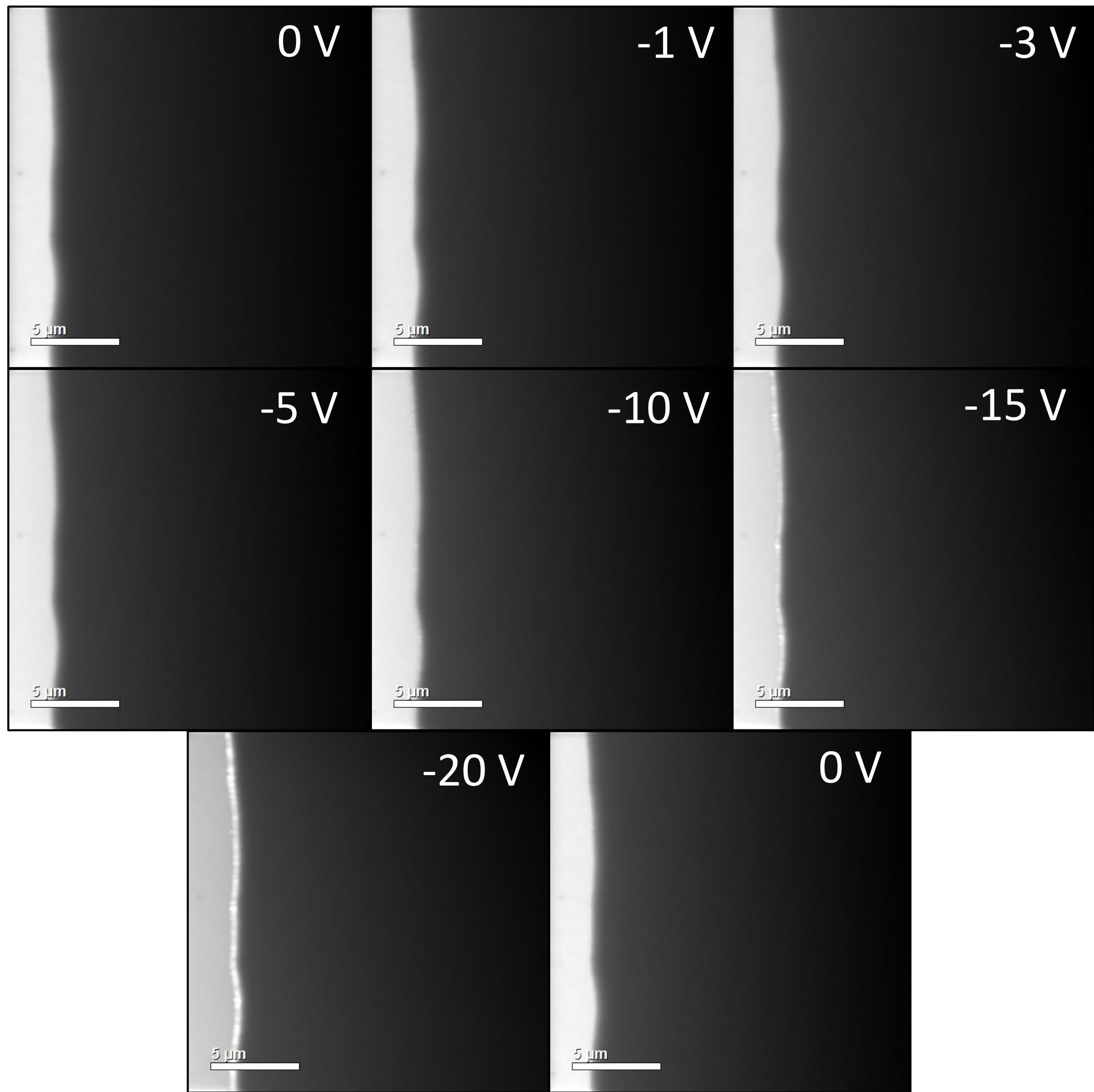

Figure 3.9: In-situ reverse biasing of Ni/GaN Schottky junction at 200 kV.

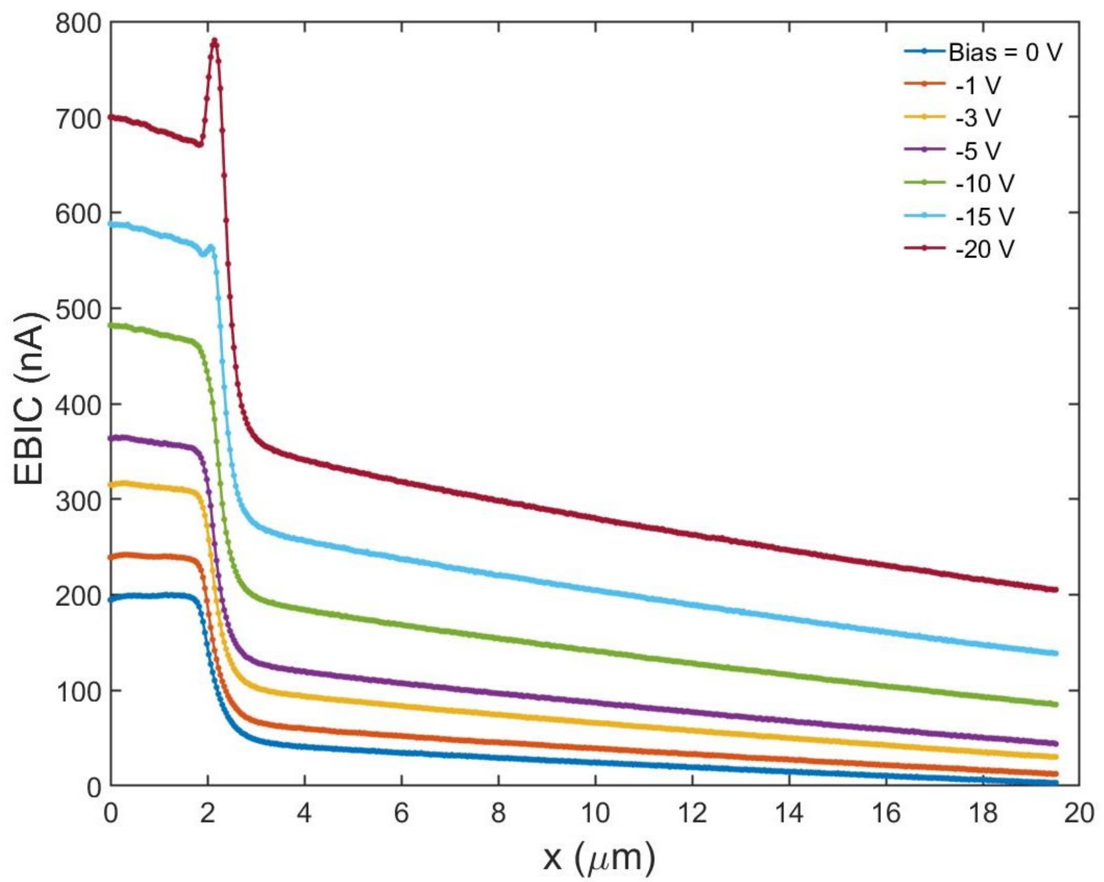

Figure 3.10: Linescans of reverse biasing of Ni/GaN Schottky junction at 200 kV.

3.3 Thinned GaN EBIC

While there are many benefits to using the bulk STEM EBIC technique for GaN, there is one large drawback, which is that the thick specimen prevents the user from employing traditional STEM techniques such as BF, DF, EDS, or EELS. This prevents the simultaneous collection of EBIC data and important microstructural information during STEM imaging. It is for this reason that there has been work towards combining the powerful techniques of EBIC inside a traditionally thin STEM specimen. The main difficulties with achieving successful thin EBIC are: (1) compromising the device during thinning/wiring, (2) achieving a thin specimen for STEM imaging but a thick enough specimen to have a good signal-to-noise ratio, and (3) quantitative analysis of the EBIC signal coming from a thin device. Progl *et al.* used a custom TEM EBIC sample holder to acquire EBIC linescans from an InGaN multiple quantum well device with V defects. [106] They found that the V defects suppressed the EBIC signal but also suggested that the V defect had a longer minority carrier diffusion length, although no EBIC linescans of the defect-free area were shown for comparison.

Another method by Han *et al.* used a piezo-driven Nanofactory Holder (the same as discussed in Section 1.3.2) to drive the W tip to a p-type Si nanowire. [107] In this experiment, the probe itself was used to form the depletion region, and an EBIC current was measured as a function of distance away from the contact at different reverse biases, shown in Figure 3.11. By fitting these lines, the authors were able to extract a minority carrier diffusion length for p-type Si, which was

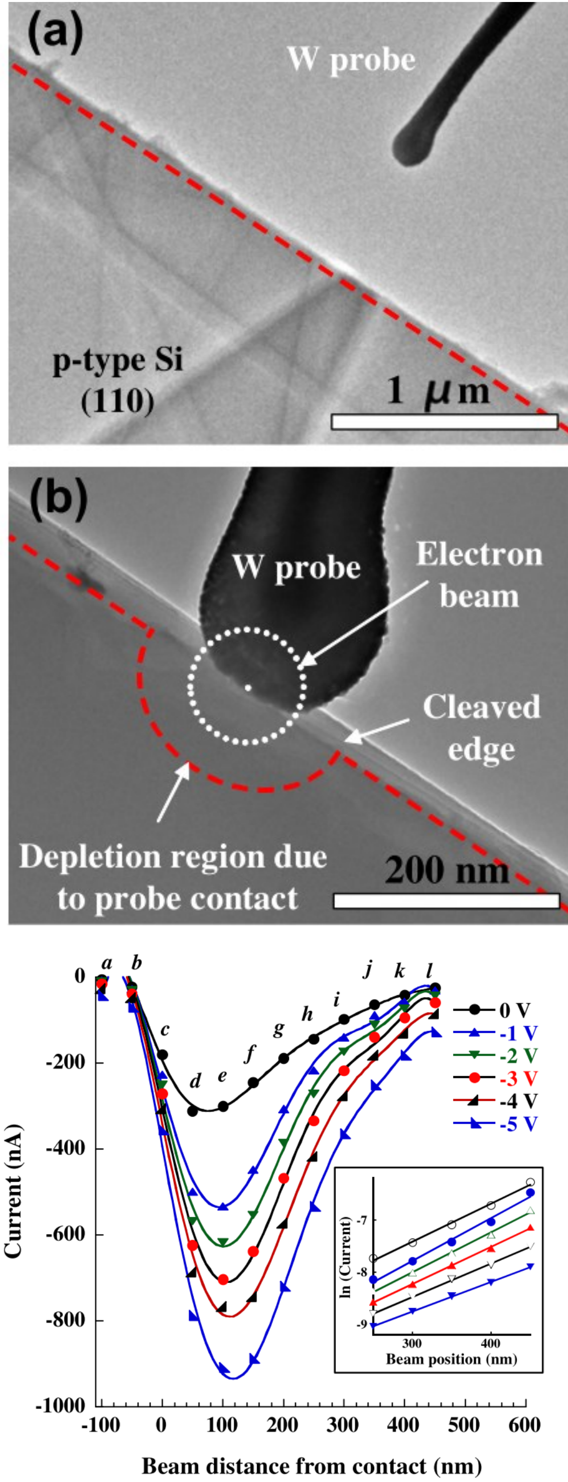

Figure 3.11: Example of thin STEM EBIC using a NF holder, from [107]. Bottom image shows the collected current as a function of distance from the contact and applied reverse bias.

orders of magnitude lower than bulk p-type Silicon (presumably due to surface recombination).

3.3.1 Data Analysis and Results

In this next section we discuss results of STEM EBIC on a n-GaN/Ni Schottky contact that was thinned via focused ion beam (FIB) milling using a Ga ion beam at Sandia National Laboratory, CA. This sample was mounted to the Cumings group Nanofactory holder in a similar geometry to the bulk STEM EBIC, where the Cu FIB Grid was mounted to the brass stub, illustrated in Figure 3.12 In this setup, the STEM beam rasters across the cross-section of the Ni/GaN junction, in the normal geometry configuration. The TEM BF micrograph shows both the $\sim$ 100 nm electron transparent portion as well as one of the thicker $\sim$ 10 μm sides.

After ensuring intimate contact of the Nanofactory Pt probe with the specimen, STEM and EBIC images were scanned and are shown in Figure 3.13. Unfortunately, neither reverse biasing nor longer scan dwell times could enable an EBIC signal to be collected for this specimen. In 3.13c, There is a shadow image of the Pt probe, the FIB deposited Pt, and the GaN, however this was only detected on the thicker side of the FIB specimen ($\sim$ 10 μm). This is likely a specimen current instead of a true EBIC current from the Ni/GaN Schottky junction. When IV curves were taken, it was obvious that the Schottky device was shorted, most likely due to Ga ion implementation during FIB thinning, which also happened to GaN p-n diodes at Sandia National Laboratory, CA.

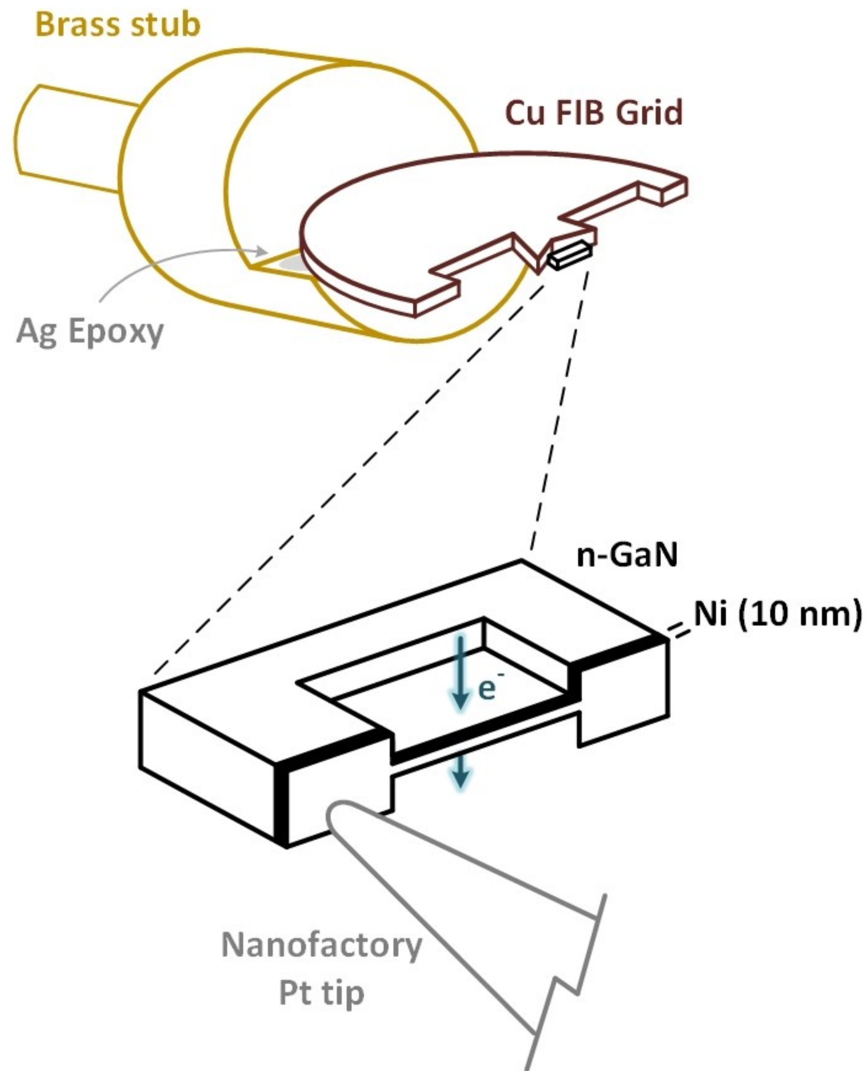

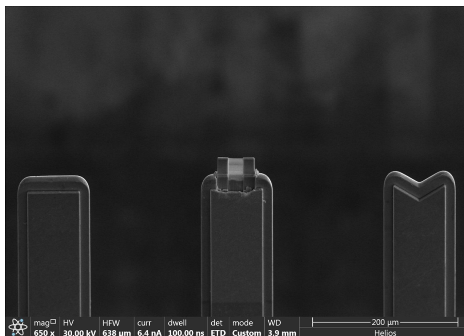

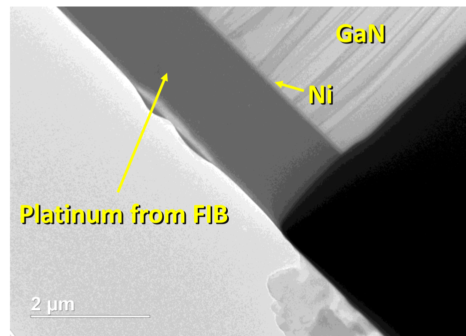

Figure 3.12: Experimental setup for thinned GaN STEM EBIC. Bottom left image is SEM micrograph of the FIB n-GaN/Ni specimen in the Cu FIB Grid. Bottom right image is TEM micrograph of specimen.

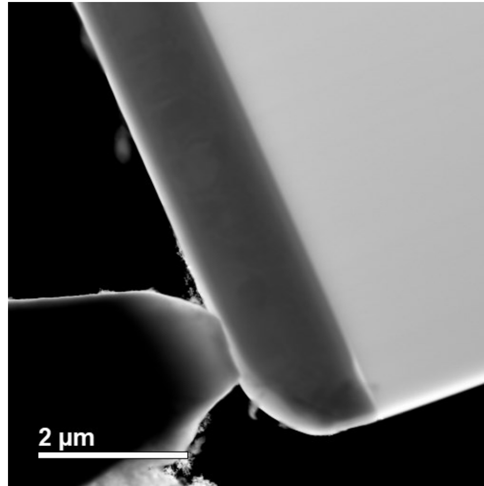

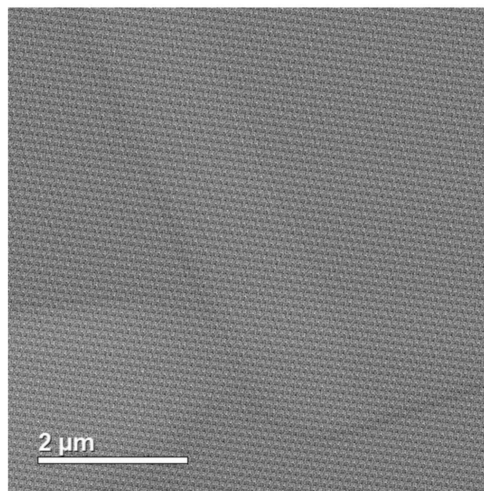

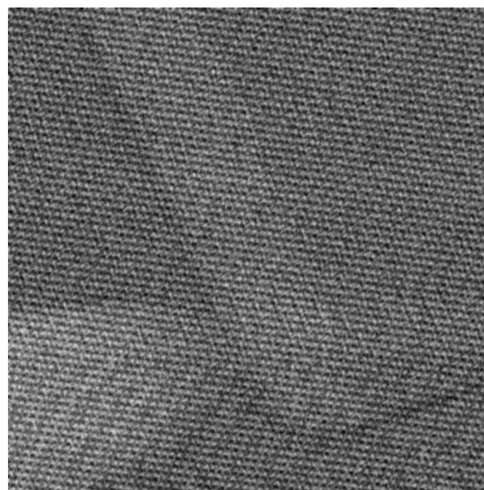

Figure 3.13: Top figure is the DF STEM image of the thick side (contrast of specimen is inverted due to extremely thick specimen). Middle image is specimen current micrograph and bottom image is after filtering. There is no apparent EBIC signal; contrast is likely due to small secondary electron current.

Chapter 4: Custom STEM Holder for In-situ Liquid Cell Electrochemistry

4.1 Liquid Cell Electron Microscopy

Since the conventional TEM is held at a high vacuum, typically $< 10^{-6}$ Pa, it was not possible to image liquids inside the TEM for most of the twentieth century, even though the scientific community was interested. Due to modern engineering advances, there are now two main techniques for imaging liquid inside the microscope. The first is to use differential pumping inside the microscope so that the sample is held at a lower vacuum than the electron gun or lenses. This is useful for gas injection experiments inside the microscope as well. The other method is to use a sealed cell which contains the liquid; this method is usually more popular since the volume of the liquid can be controlled and known. This method was pioneered by Frances Ross at IBM in 2003. [108] Since then, the field of sealed liquid cell microscopy has grown to study a wide range of physics, chemistry, and materials science research questions. A schematic of liquid cell electron microscopy in cross-section is shown in Figure 4.1. With just a sealed liquid cell in the TEM, one can obtain images and also interact with the nanocrystals or biomaterials inside the cell

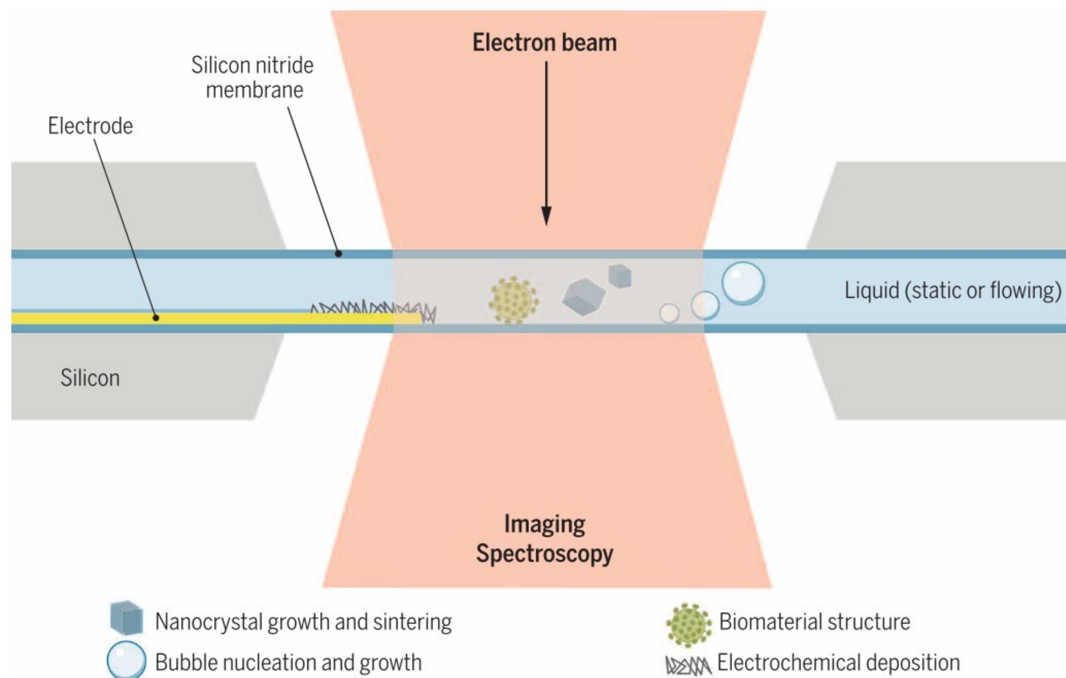

Figure 4.1: Liquid cell microscopy for a variety of applications. From [109].

with the electron beam. However, more advanced cells and holders allow the user to image while flowing liquid through the cell, applying potentials to the electrodes, or even cooling or heating the specimen. [109]

One main issue with the sealed liquid cell is the overall thickness of the liquid layer plus the top and bottom viewing windows (typically silicon nitride membranes), which can easily increase the overall thickness to several hundred nanometers. Another problem is the pressure inside the sealed cell is lower than the surrounding vacuum of the microscope, which can cause significant bowing in the cell such that the overall thickness becomes even worse. Luckily the development of microfabrication techniques have enabled researchers overcome many of these issues.

4.1.1 CINT Electrochemical Liquid Cells

The Center for Integrated Nanotechnologies (CINT) Electrochemical Cell Discovery platform at Sandia National Laboratory is a sealed liquid cell developed for in-situ electron microscopy. The cell was developed in 2009 by John Sullivan specifically for STEM studies of battery electrode materials. [53] The chip is composed of two halves which epoxy together to form the sealed liquid cell, shown in Figure 4.2b. The bottom half has masked W electrodes that are connected through vias to the outside bond pads; these electrodes can be patterned using electron lithography techniques and are compatible with a variety of electrode materials. The view port narrows to an extremely small (30 μm) window on both the top and bottom chip. These windows are comprised of SiN membrane which is extremely thin (50 nm) but overall highly robust against the vacuum because the window is so small. When filled with electrolyte through the fill ports (shown in 4.2a and d), the thickness of the liquid is approximately 100 nm, which allows for higher resolution imaging than is available in commercial liquid cells.

The main advantage of the EC liquid cell over commercial liquid cells is that is has up to ten electrodes patterned onto the silicon nitride membrane window. An example electrode geometry with ten electrodes close together is shown in 4.2d. Multiple electrodes are useful for electrochemical experiments because several working electrodes can be patterned and studied without worrying about variables such as a slightly different electrolyte or beam operating conditions.

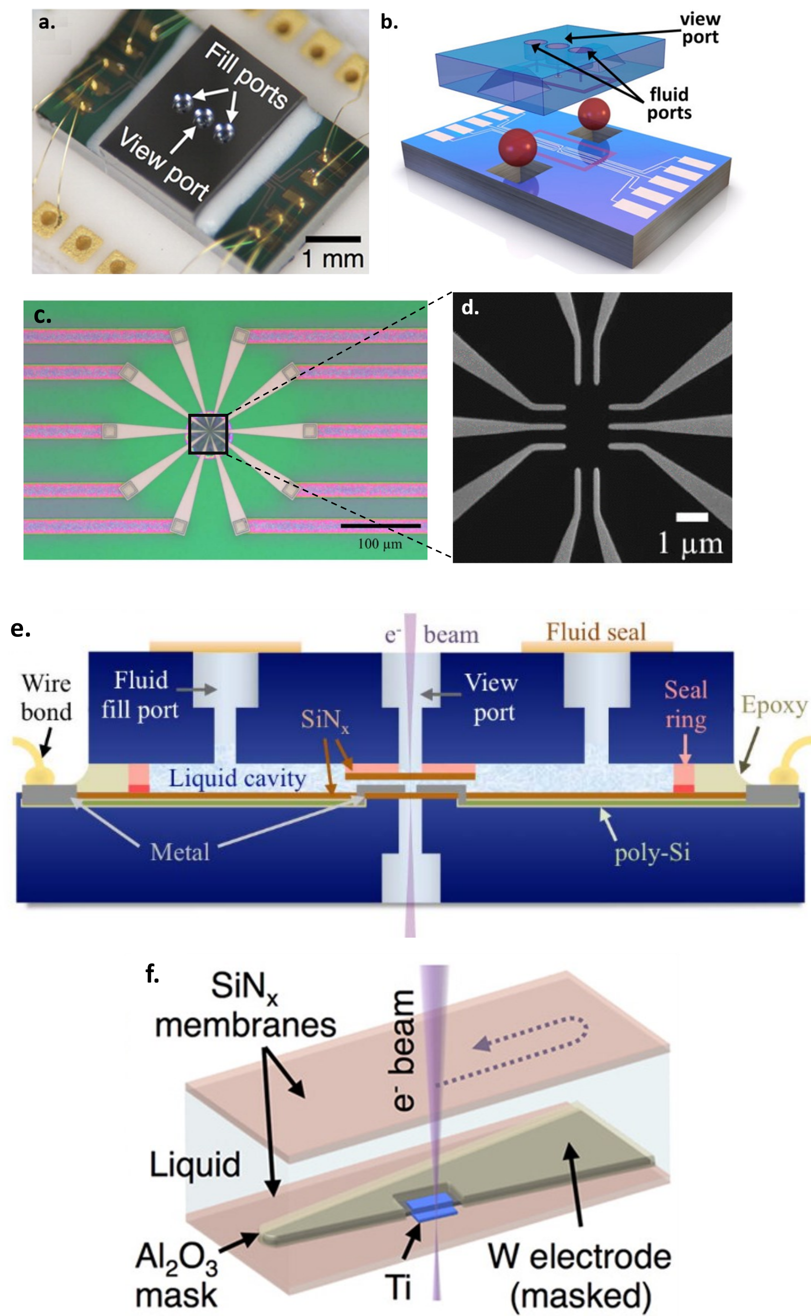

Figure 4.2: The CINT Electrochemical Discovery Platform showing (a) sealed and wire bonded cell, (b) top and bottom halves, (c) optical micrograph of the tunneled electrodes (pink) and the exposed W electrodes, (d) electron transparent center of cell, (e) cross-section of entire cell and (f) cross-section of the cell through the view port. From [53].

4.2 UMD Custom In-situ Holder

In order to fully utilize the capabilities of the CINT EC liquid cell, we have designed and built a custom JEOL 2100 in-situ holder which is compatible with the liquid cells. This holder can fit the unconventionally sized liquid cell sample into the UMD JEOL microscopes as well as make electrical connection to the holder so that in-situ electrochemical experiments can be performed inside the microscope. This holder could also be used for other in-situ EM work, providing the chip used matches the dimensions of the bottom half of the liquid cell (5 mm x 3 mm x 0.5 mm). Or, this holder could be used with a different sized device if a different chip carrier was used that could accept the device, but still fit into the front assembly and connect to the pogo-pins.

The most limiting aspect of this design was designing the front end of the holder (parts 1-7 in Figure 4.3) to fit inside the microscope. The JEOL 2100 F at University of Maryland, College Park is a UHR - ultra high resolution - microscope, which means that the objective lens is designed for high resolution imaging, as discussed in Section X. The distance between the pole pieces in the objective lens is extremely small in the JEOL 2100 F, which sets a size limitation on the thickness of the holder at the front end (nose). The extremely tight requirements are complicated by the fact that the EC liquid cell is almost 1 mm itself, after the top and bottom are sealed together. This leaves very little room for the chip carrier on which the specimen sits and which connects the sample to the holder.

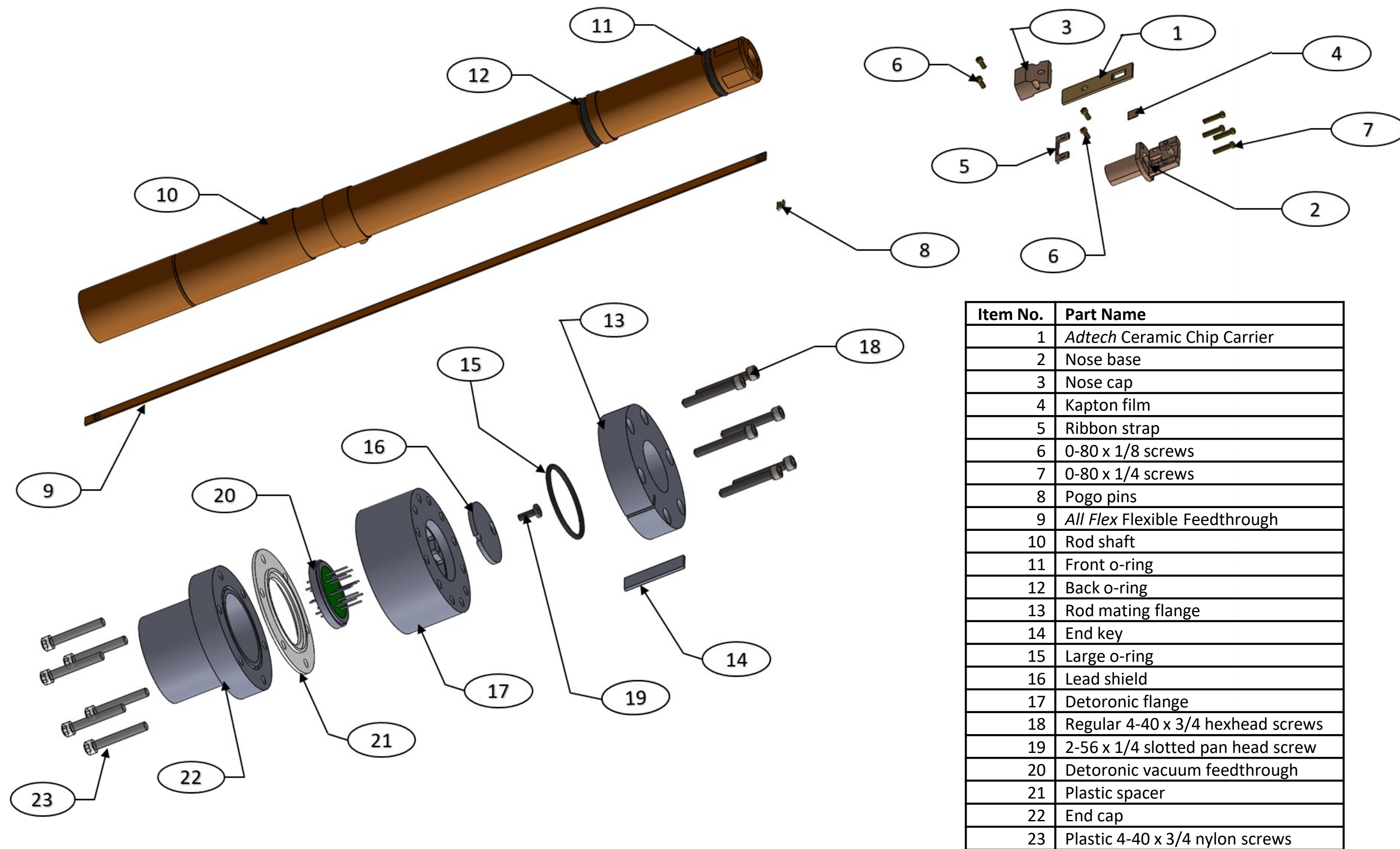

Item No.	Part Name
1	*Adtech* Ceramic Chip Carrier
2	Nose base
3	Nose cap
4	Kapton film
5	Ribbon strap
6	0-80 x 1/8 screws
7	0-80 x 1/4 screws
8	Pogo pins
9	*All Flex* Flexible Feedthrough
10	Rod shaft
11	Front o-ring
12	Back o-ring
13	Rod mating flange
14	End key
15	Large o-ring
16	Lead shield
17	Detoronic flange
18	Regular 4-40 x 3/4 hexhead screws
19	2-56 x 1/4 slotted pan head screw
20	Detoronic vacuum feedthrough
21	Plastic spacer
22	End cap
23	Plastic 4-40 x 3/4 nylon screws

Figure 4.3: CAD exploded view of the JEOL custom in-situ holder.

Another holder design consideration is to electrically isolate the specimen from the holder. The reason for this is because as the holder is inserted into the microscope, it becomes grounded to the microscope. The reason for this is that, again due to the space restrictions inside the objective lens, there are mechanical limits to how far the holder can be tilted, raised, or lowered. If the engineered limits are surpassed, for example in the case of a large nose, the holder can crash into the objective lens and damage it. To limit the damage to the microscope, there is a safety feature which is determined by the voltage difference between the holder and the objective lens. The holder is typically held at a constant potential of -4 V relative to the objective lens. If the holder or specimen touches the lens, the short will activate the safety mechanism which will prevent any continued movement of the holder. For electrochemical specimens, the holder potential can cause the unwanted movement of ions or, even worse, damage the sensitive specimens. In this case, the user would ground the holder so that the specimen is kept isolated, however this can significantly increase the chances of an undetected collision with the goniometer. Therefore, to avoide the potential risk to both the microscope and the specimen, we isolate the specimen ground from the holder, although it can be easily wire-bonded to ground to the holder if the user wishes.

The front assembly was designed for combatibility with the JEOL microscope and also for convenient loading of the liquid cell. Figure 4.4 shows the loading process, which is made easier for the user by the addition of a teflon piece which is attached to the holder base. This allows the user to gently guide the chip carrier onto the fragile pogo pins, and then secure the chip to the base by carefully placing

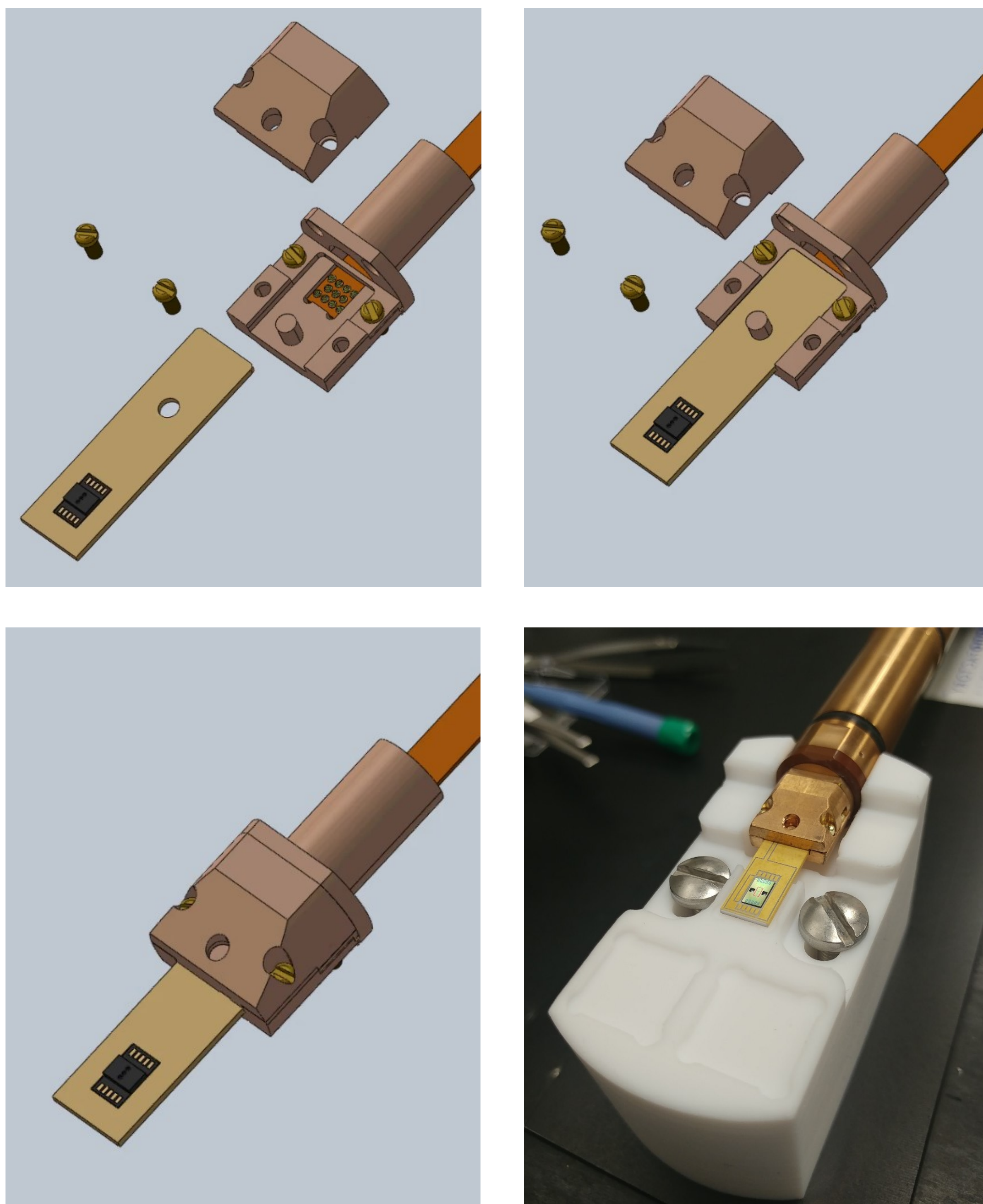

Figure 4.4: Front (nose) of custom EC lquid cell holder. CAD parts illustrate how chip carrier is secured into holder after the liquid cell has been glued and soldered. Bottom right figure shows actual holder with chip carrier.

the cap on top and screwing in the 0-80 front screws. This design is preferable to the original Nanofactory design of the holder which has a cantilevered cap which the user slides the chip inside of (similar to the JEOL single tilt holder loading mechanism). This design can cause the pogo pins to be bent or damaged during chip carrier loading or unloading.

An *All Flex* flexible feed through and *Emulation Technology* pogo pins were used to connect the chip carrier to the back end of the holder. The strip is held in place with a small strap which is held in place by 0-80 screws, which help keep the pogo pins in place during loading. Beneath the pogo pins on the front assembly is a small thin Kapton film which prevents the pins from shorting to each other. At the back end of the holder, the connections were soldered to insulated Au wires which were then soldered to the *Deteronics* hermetic multipin connector. Once on the air side, the pins were soldered to a low force LEMO multipin connector for connecting the holder to an external potentiostat.

The ceramic chip carrier (part 4) was designed at UMD and built by *Adtech Ceramics*. It is a two layer co-fired ceramic chip carrier with bond pads to connect to the EC liquid cell, gold metallic vias which are fed through the chip carrier to the backside which then connects to the pogo pins in the All Flex flexible feedthrough. The 2D CAD drawings for the ceramic layers as well as all four metal layers are included in Appendix B. Again, the main limitation to this design was the total thickness of the EC liquid cell plus the chip carrier. The chip was designed such that the liquid cell actually sits inside the chip carrier, instead of on top of it, illustrated in Figure 4.5.

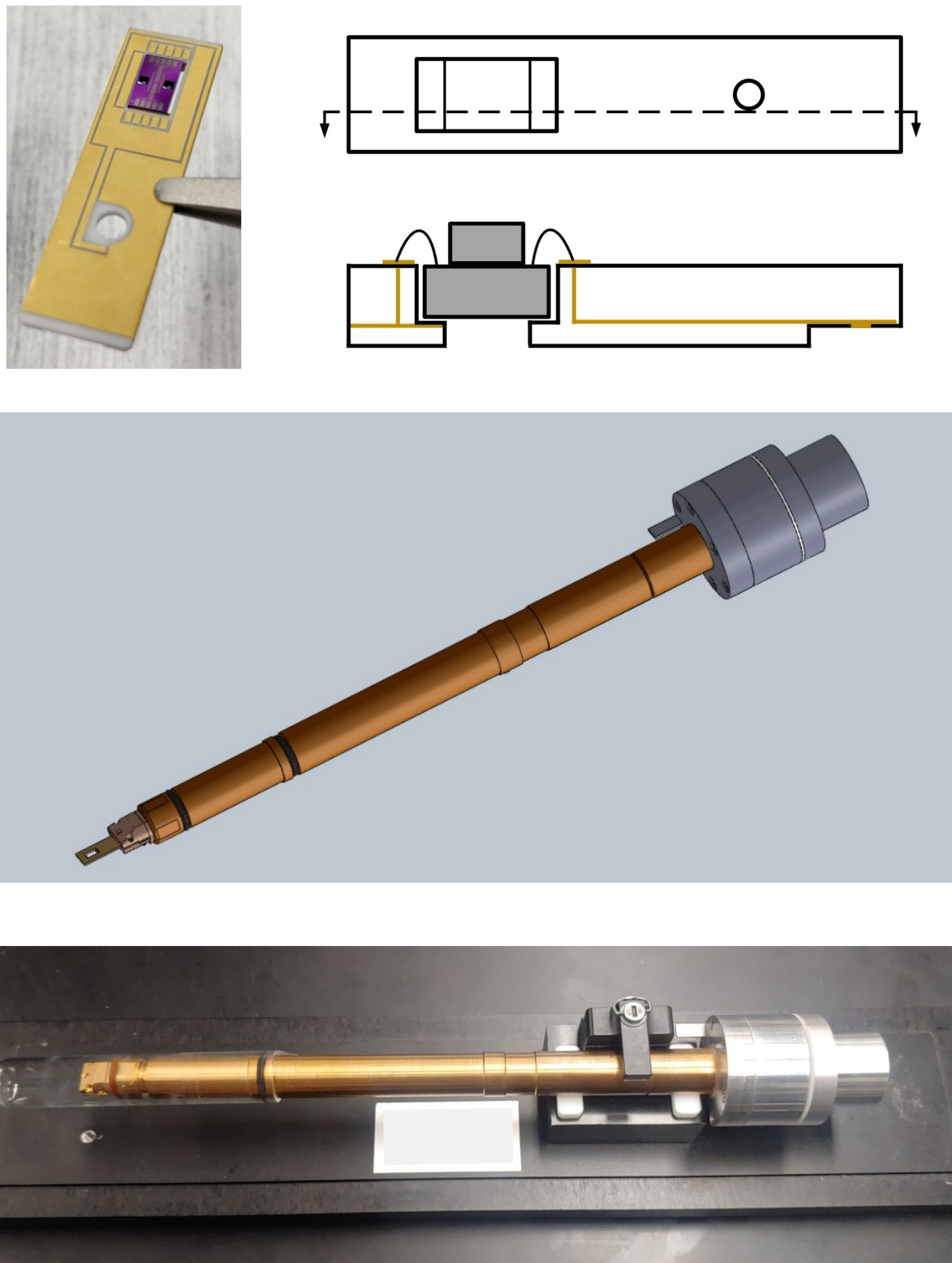

Figure 4.5: Top figures show close up of ceramic chip carrier and cartoon schematic of side view of liquid cell sitting inside the holder. Middle and bottom figures show the entire holder assembly.

The connections were tested and verified at each step. When the chip carrier is placed inside the holder, the resitivity between the bond pads on top of the chip all the way to the LEMO output connector is ~ 1 Ωm. The chip carriers are very easy to wire bond to, whereas the liquid cell bond pads are more difficult. Assuming a good wire bond to the liquid cell bond pads is formed, this will allow the user a high quality connection from the liquid cell electrodes all the way to outside the microscope, to the external potentiostat.

Chapter 5: Conclusions and Future Work

5.1 Bulk STEM EBIC

In conclusion, we have demonstrated a reproducible and compelling technique for measuring the minority carrier diffusion length in homoepitaxial n-GaN using STEM EBIC in a bulk planar geometry. The characteristic linescans which cross the Ni/GaN junction contain information about both the large interaction volume and the smaller minority carrier diffusion length. The extremely large interaction volume causes a large background signal which can be fit and subtracted reproducibly. The resulting subtracted EBIC profile can be fit with an erfc to extract the hole diffusion length, as explained by our simple model based on generation in the neutral region of n-GaN.

These conclusions are further supported by the results of both the reverse biasing studies as well as beam damage studies. In the case of reverse biasing, the growth of the depletion region under reverse biasing matches the expected behavior. This suggests that the resolution of the technique is good enough to detect small carrier lengths. Furthermore, the results from the accumulated beam damage at 200 kV suggests knock-on damage and the creation of N vacancies and interstitials.

However, despite the promising results of this technique, there still are some

questions that remain to be answered. For example, a more detailed study of the entire parameter space including beam current and sample tilting could help increase the accuracy of the technique for diffusion length measurements. Furthermore, acquring accumulative beam damage micrographs at 100 kV would be useful for developing a more complete understanding of the effect of electron irradiation in GaN.

More specifically, the results from Nichterwitz [89] and Haney [110] suggest that during bulk STEM EBIC, we may be injecting carriers into the system faster than they can diffuse away. This is known as the high injection regime, which causes a self-screening effect and non-linear behavior in the device. The equations for determing injection regime given by Haney assume that the carrier diffusion length is less than the size of the interaction volume, which menas that they can't be used for bulk STEM EBIC. From [89], the equation for estimating the density of injected carriers is given by:

$$N_{e,h} = \frac{E_b I_b \tau_{e,h}}{e E_{e,h} L_{e,h}^3} \times (1 - \Lambda) \tag{5.1}$$

Depending on the lifetime of carriers in n-GaN, $\tau_{e,h}$, and the reflection coefficient for n-GaN, Λ, the expected density of generated electrons could be between 10^{13} to 10^{18} cm^3, which, considering $N_D = 3 \times 10^{16}$ cm^{-3}, could place these experiments within the high injection regime. This question could be answered by a more detailed study of the influence of the beam current on the minority carrier diffusion length. Perhaps a cross-over point could be deduced, allowing us to determine the

beam current range which is approriate for low injection conditions.

Another question remains as to how effective this technique is at detecting differences between n-GaN samples with different diffusion lengths, for example the difference between GaN-on-GaN vs GaN-on-Si. Our initial work suggests that this technique would be able to classify the sample quality according to our EBIC measurements, but since all of our measurements were on similar (undamaged) homoepitaxial n-GaN grown on GaN, this question remains unanswered. Another question remaining is the usefulness of this technique to other materials systems, which may have different diffusion lengths, depletion widths, interaction volume sizes, etc. One potential material which has gained interest is β-Ga_2O_3, which has recently been studied via SEM EBIC diffusion length measurement technique. [111]

5.2 Custom In-situ Holder

Additionally, we have designed and built a custom in-situ holder which is compatible with the CINT EC liquid cell platform. This holder is compatible with any JEOL microscope which accepts the 2100 series holder. One of the advantages of this holder is the safe chip carrier loading mechanism which reduces the chances of bending or breaking the delicate pogo pins during loading and unloading. This holder could also be used for other in-situ electron microscopy work, providing the chip used matches the dimensions of the bottom half of the liquid cell (5 mm x 3 mm x 0.5 mm). Or, this holder could be used with a different sized device if a different chip carrier was used that could accept the device, but still fit into the

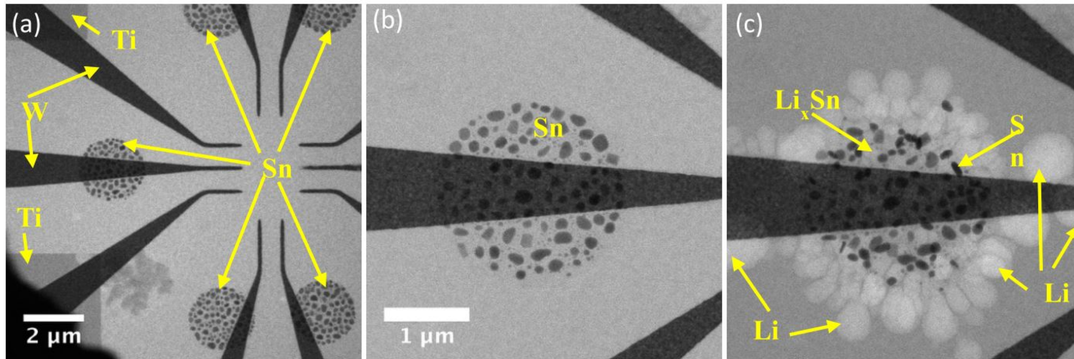

Figure 5.1: CINT EC Liquid Cell Sn alloying anode capabilities. From [112]

front assembly and connect to the pogo-pins.

The custom in-situ holder could expand upon preliminary work by Goriparti *et al.* to study the effects of [112], as shown in Figure 5.1. This initial work found that the Sn inside the liquid cell setup was electroplating Li on the surface of the Sn anode, as opposed to intercalating inside as well as undesirable gas formation in the liquid cell.

Beyond Sn alloying anodes, and even beyond liquid LIB studies, this holder could be easily adapted to study solid state LIB with in-situ EM. A similar technique as EBIC could be used to quantify the state of charge during cycling, in order to understand the solid-state electrolyte and electrode lithiation mechanisms at the nanoscale.

Appendix A: Bulk STEM Sample Preparation S.O.P.

This sample preparation method was used to prepare single crystal GaN/Ni Schottky contacts for bulk STEM EBIC imaging. Samples were acquired from Sandia National Laboratory (Alec Talin) as approximately 1 cm x 1 cm substrate with no contacts. Steps 1 and 2 can be skipped if there are already Ni and In contacts, respectively. Step 6 can be done at any time.

1. Make Nickel Schottky contact

   (a) Under microscope, align shadow mask on top of GaN substrate so that the Ni pads will deposit in the desired pattern. Tape down mask with carbon tape.

   (b) Deposit 15-30 nm of Ni via thermal or e-beam evaporation in AimLab, following standard clean lab procedures.

2. Make Indium Ohmic Contact

   (a) Take In foil or wire and a soldering gun with a clean tip (if you can't find a new tip, just clean one with sand paper and rinse with ethanol).

   (b) Heat up the gun sufficiently to melt the In ($\sim$ 160 °C).

   (c) Melt In and apply to the specimen on the GaN surface (see 5b).

3. Test Schottky contact

   (a) Use four-probe station in RM 1314. Connect two of the probes to the Keithley 236 Source Measure Unit. Set the 236 to Source Voltage/Measure Current, with current limit set to 2 mA.

   (b) Before testing sample, confirm that probes are working by touching together and verifying ohmic contact. When using non Pt coated W probes, it's best to also touch both probes to In contact and again verify ohmic contact (this also gets some In on the probe tips and makes it easier to contact to Ni).

   (c) Keeping Keithly in non-operating mode or applied voltage at 0 mV, touch one probe to the In contact and the other one to the Ni contact, sometimes the probe needs to be pressed hard into the Ni contact.

   (d) Ramp voltage in increments of 10 mV while recording voltage/current. Current should remain approx 0 nA until turn-on voltage (typically between 100-600 mV for GaN-Ni) and reach 1 mA within approximately 500-1000 mV of turn on voltage.

4. One-sided wire bond to Ni pads

   (a) Use K&S Au ball bonder in Aimlab. Create a ball using a test chip and following instructions (thread wire, pull it through, bend it. Raise the lever on the left to lock the tool head, press the mouse - referred to as chessman - to make the first bond, then lower the lever to unlock the

tool head and press the chessman to make a second bond. On the second bond the tool will lift up and perform the electric flame off (EFO) to create a ball at the tip of the ceramic tool).

(b) Choose the Ni pad you want to wire to and verify that the stage and the tool head are at the correct height. Press the chessman, adjust the stage slightly so that the ball is aligned to that pad, then release the chessman to create the first bond.

(c) Instead of creating a second bond, lift the lever on the left to raise the tool head. Then carefully cut the Au wire with a small pair of scissors (do not use EFO to cut the wire).

(d) Repeat until all desired Ni pads are wire bonded.

5. Cleave substrate

   (a) Identify which Ni pads are good Schottky contacts and which ones can be cut through.

   (b) Choose one or two Ni pads for TEM sample and make sure that the In is close to those contacts. You may have to resolder In closer to the Ni contact(s) of interest.

   (c) Use the diamond scribe to cut the GaN into approx 2 mm x 4 mm substrate, making sure to have both the Ni pad and a little bit of In on the chosen piece.

6. Make Nanofactory Holder stubs

(a) Use benchtop machining tools in RM 1314. Make sure digital microscope is set up on whichever tool you are using, angled to best observe your work.

(b) Start with 0.032" (0.81 mm) brass wire.

(c) Put wire into collet and into benchtop lathe, with about 1/16" of brass sticking out from collet (see A.1).

(d) Use benchtop lathe to face off wire and then to turn down outside diameter from 0.032" to 0.015-0.016" and about 0.02-0.03" long.

(e) Pull out brass wire from collet and use wire cutters to cut a liberal size piece (about 1/8-1/4" long).

(f) Put piece back into lathe with turned side inside collet and face off the side that was cut with the wire cutters so that it is now flat.

(g) Repeat steps c-f for as many stubs as needed.

(h) Use benchtop end mill with a slitting saw to cut a "shelf" into the flat side of the stub. Shelf height will depend on the thickness of the GaN substrate. We want the surface of the GaN to end up at the center of the Nanofactory holder. Shelf height = 0.016" − thickness of GaN substrate.

7. Clean stubs

(a) Use an ultrasonic bath to clean the stubs with three rinses of acetone, followed by three rinses of isopropyl alcohol, and three rinses of DI or RO water.

8. Mount sample in to stub

   (a) This step can either be done directly while the stub is mounted to the Nanofactory holder or in the temporary stub holder.

   (b) Place the Nanofactory holder under the go-pro/lens microscope and focus on the sample tip area.

   (c) Make sure that the Nanofactory holder is right side up (label is pointing up, multipin connector is pointing down).

   (d) Place stub into the holder, with the shelf parallel to the nose end of the holder.

   (e) Then use SilverWorks Epoxy (1:1 weight ratio of part A and B) and place a small amount on the stub shelf.

   (f) Carefully place the cleaved GaN specimen onto the shelf of the stub, making sure that some of the epoxy reaches the indium ohmic contact to ensure proper electrical connection. (see A.1)

   (g) Place holder in oven for 30-45 minutes at 90° C. Take out and let holder cool completely.

   (h) Place tip hat with Pt tip or Cu wire onto the ceramic ball, then use SilverWorks Epoxy to connect the other end of the gold wire to the tip. Again, use oven to cure epoxy.

   (i) (Note: if the gold wire breaks off of the Ni pad, a small dot of silver epoxy can be used to reattach it.)

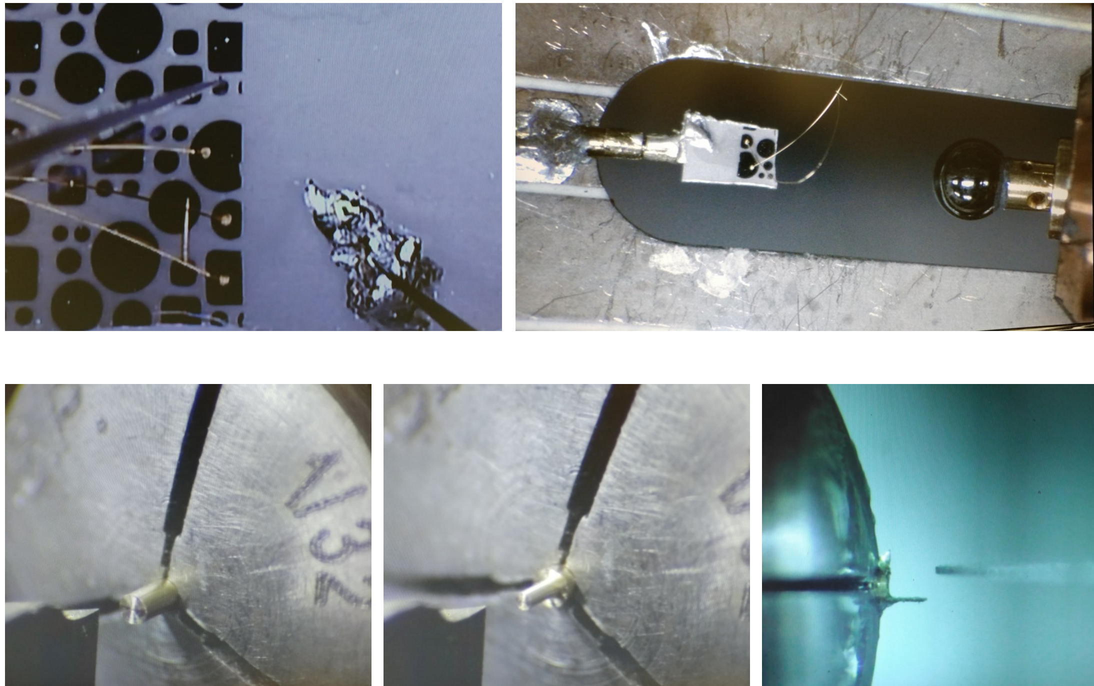

Figure A.1: Top left picture shows GaN with Ni pads and wire bonds while being tested in Keithley. Top right picture shows sample mounted to stub inside the Nanofactory holder (tip hat is not shown). Bottom images show how the Nanofactory mounting stubs are machined.

Appendix B: Bulk STEM EBIC Matlab Code

Attached below is an example of the numerical simulation used to model the bulk STEM EBIC profiles (after background subtraction). This is shown for the example of different input beam diameters, however, the script can be modified to explore the effects of changing other parameters. Furthermore, the generation volume equation (labeled beamfn) could be entirely replaced by the trajectories output file from CASINO for thick GaN (~100 μm). Since the entire interaction volume is simulated in CASINO, the subsequent numerically simulated EBIC profile would include both the short and long decay length. This would allow for direct comparison to the un-subtracted EBIC data. This has been previously explored for EBIC at SEM voltages. [94, 95] The difficulty with bulk STEM is that the interaction volume is quite large, and the typical mesh resolution of the CASINO trajectories output file is larger than the minority carrier diffusion length, thus making it unusable. Careful consideration and computational power would be needed to accurately simulate the interaction volume in CASINO with a small enough mesh resolution to then be used to replace the beamfn in the convolution.

```
%% script to simulate bulk STEM EBIC data for different diffusion
lengths and beam diameters with constant alpha and depletion region

clear all ;
close all ;

%% define mesh and depletion width and beam alpha parameters

xn = 256 ; % N pixels in x
yn = 256 ; % N pixels in y
zn = 256 ; % N pixels in z
% assume the three values above are all even, so that all (x, y, z)
% coordinate values are non-zero.

xrange = 2000 ; % nm limits (+/-) in x
yrange = 2000 ; % nm limits (+/-) in y
zrange = 2000 ; % nm limits (+/-) in z
% the size of the outer box of the data cube, for integration

xsp = xrange / xn ;  % spacing of points (half-spacing actually)
ysp = yrange / yn ;
zsp = zrange / zn ;

[X, Y, Z] = meshgrid(-(xrange-xsp):2*xsp:(xrange-xsp),-(yrange-
ysp):2*ysp:(yrange-ysp),-(zrange-zsp):2*zsp:(zrange-zsp));

depdep = 240 ; % depletion depth in nm
% beamd = 30 ; % beam diameter at surface in nm, as FWHM
beama = 0.01 ; % beam alpha parameter

zintmin = floor(zn/2 - depdep/(2*zsp)); % the index at the bottom of
the depletion depth, for bottom of integration
zintmax = ceil(zn/2); % the index at z = 0 for the top of integration.

%% loop beam diameter parameter

startbeamd = 0;

m = 7;
for beamind = 1:m  % this first for loop can be easily rearranged for
depletion width or alpha

    beamd1 = startbeamd+20*beamind;
    beamd(beamind)= beamd1;

sigb = (beamd1 + beama .* abs(Z)) ./ (2*sqrt(2*log(2))); % sigma due
to beam diameter.
beamfn = (1./((sigb.*sqrt(2*pi)).^2)) .* exp( -0.5 .* (X.^2 + Y.^2) ./
((sigb).^2)); % beam function
beamfn(:,:,(1+zn/2):zn) = 0; % No beam above z = 0. Set it to zero.
clear('sigb');
```

```
k = 20;
for dif_input1 = 1:k %iterating diffusion lengths from 20 to 400 nm
    stepsize = 20; %in nm
    dif_input = dif_input1*stepsize;
    dif_vec(dif_input1) = dif_input;
    dif_fn = (1./((dif_input.*sqrt(2*pi)).^3)) .* exp( -0.5 .* (X.^2 +
Y.^2 + Z.^2) ./ ((dif_input).^2)); % diffusion function
    holefn = ifftn(fftn(fftshift(dif_fn)) .* fftn(beamfn)); % hole
function, available for EBIC current

    for ind = 1:xn
        ebicsim(ind) =
trapz(trapz(trapz(holefn(ind:xn,:,zintmin:zintmax))));
    end
    ebicsim = ebicsim ./ max(ebicsim);

    Xtran = transpose(X(1,:,1));
    ebicsimtran = transpose(ebicsim);

    erfcfit_output =
fit(Xtran,ebicsimtran,'c+a*erfc(b*x)','StartPoint',[0.5,0.002,0.001]);
    coeffval = coeffvalues(erfcfit_output);
    difflengthfit(dif_input1) = 1./(sqrt(2)*coeffval(2));

    difflengthmat(beamind, dif_input1) = difflengthfit(dif_input1);

end

end


%% plot results of the beam convolution simulation


parameter = 'beam diameter';
str_parameter = num2str(beamd);

figure('NumberTitle', 'off', 'Name', "Bull STEM EBIC Results from " +
parameter , 'position',[400, 100, 1000, 800])

plot(dif_vec, difflengthmat(:,:), 's','MarkerSize',10, 'Linewidth', 3)
ylim([0, 450])
xlim([0,450])
legend("d_{beam} = " + beamd)

title("\fontsize{32}Effect of changing beam diameter")
xlabel("\fontsize{26} Input Diffusion Length (nm)")
ylabel('\fontsize{26} Fit Diffusion Length (nm)')
set(gca,'FontSize',20)
grid on
```

Appendix C: Custom Holder CAD Drawings

This appendix includes 2D CAD drawings for most of the parts that comprise the custom in-situ liquid cell holder. The drawings for the holder-rod itself are not included because they include proprietary information from JEOL Ltd. Our custom holder will fit into any JEOL microscope which can accept a holder for the JEOL 2100 series. The front assembly (nose) including the base, cap, and chip carrier are included. Also included are the four metal layers for the chip carrier. The end assembly, including the rod mating flange, lead shield, deteronics flange, plastic spacer, and end cap.

These drawing are meant to be used as a jumping off point for a student who wishes to build a similar in-situ holder. The exact dimensions should be checked by the student for their specific purposes. For graduate students considering building their own holder for the JEOL 2100 FEG UHR at UMD, this author suggests instead partnering with one of the four vendors: Gatan, Hummingbird Scientific, Protochips, or DENSsolutions (at the time of this publication). If eleven connections are enough, then this author recommends instead of building an entirely new holder to instead redesign the chip carrier to fit their device and still be compatible with the front assembly of this holder.

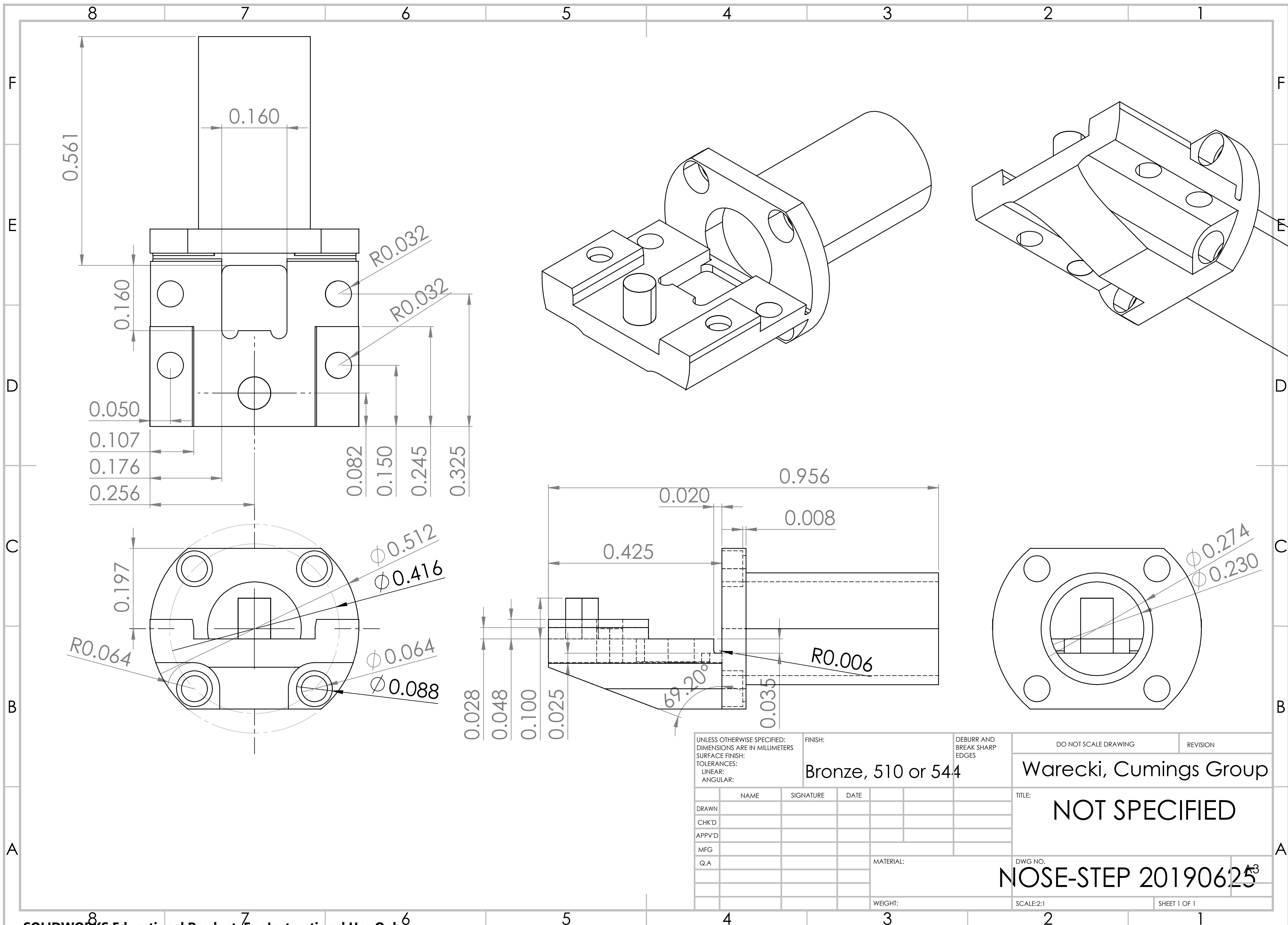

SOLIDWORKS Educational Product. For Instructional Use Only.

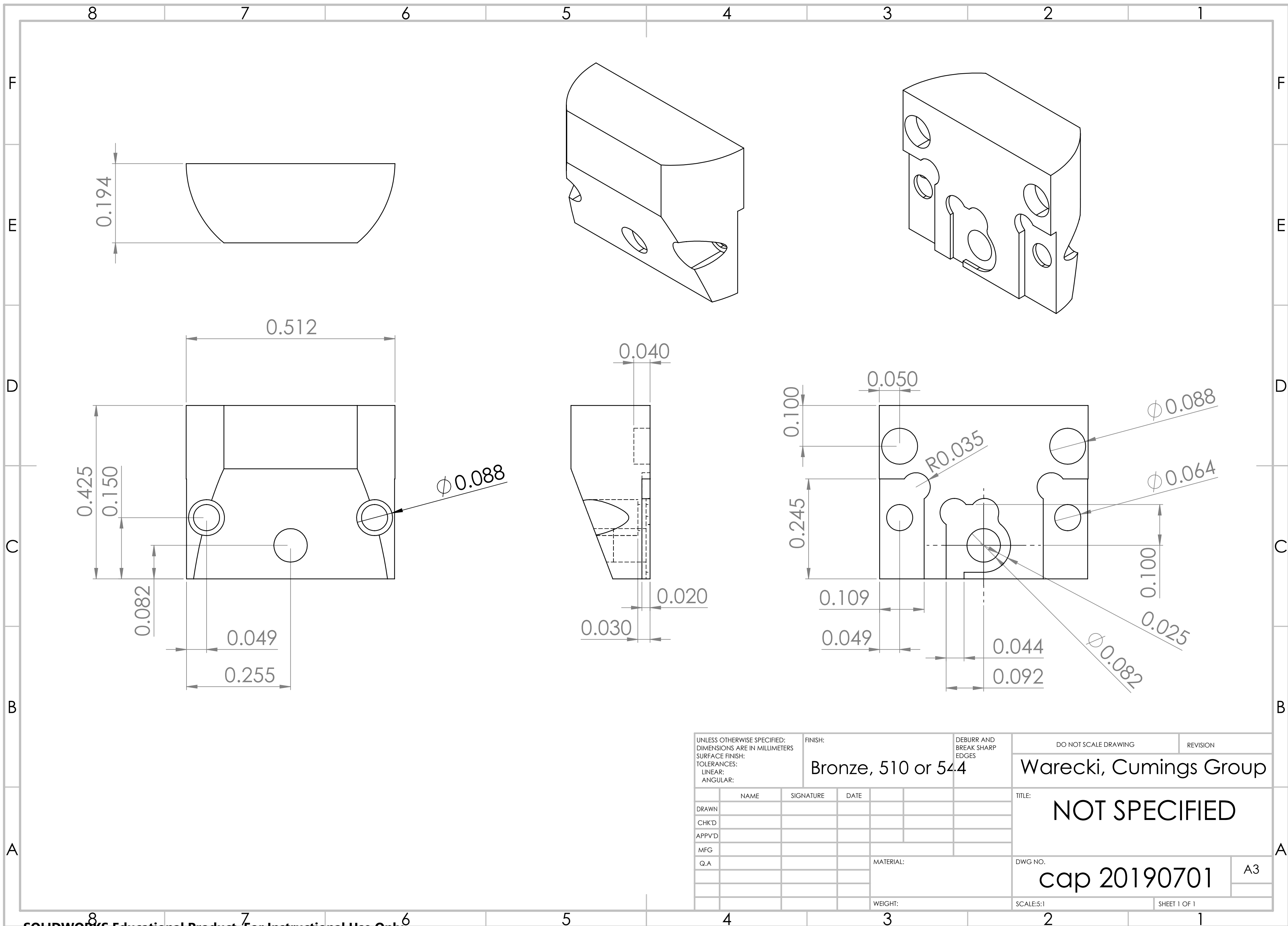

SOLIDWORKS Educational Product. For Instructional Use Only.

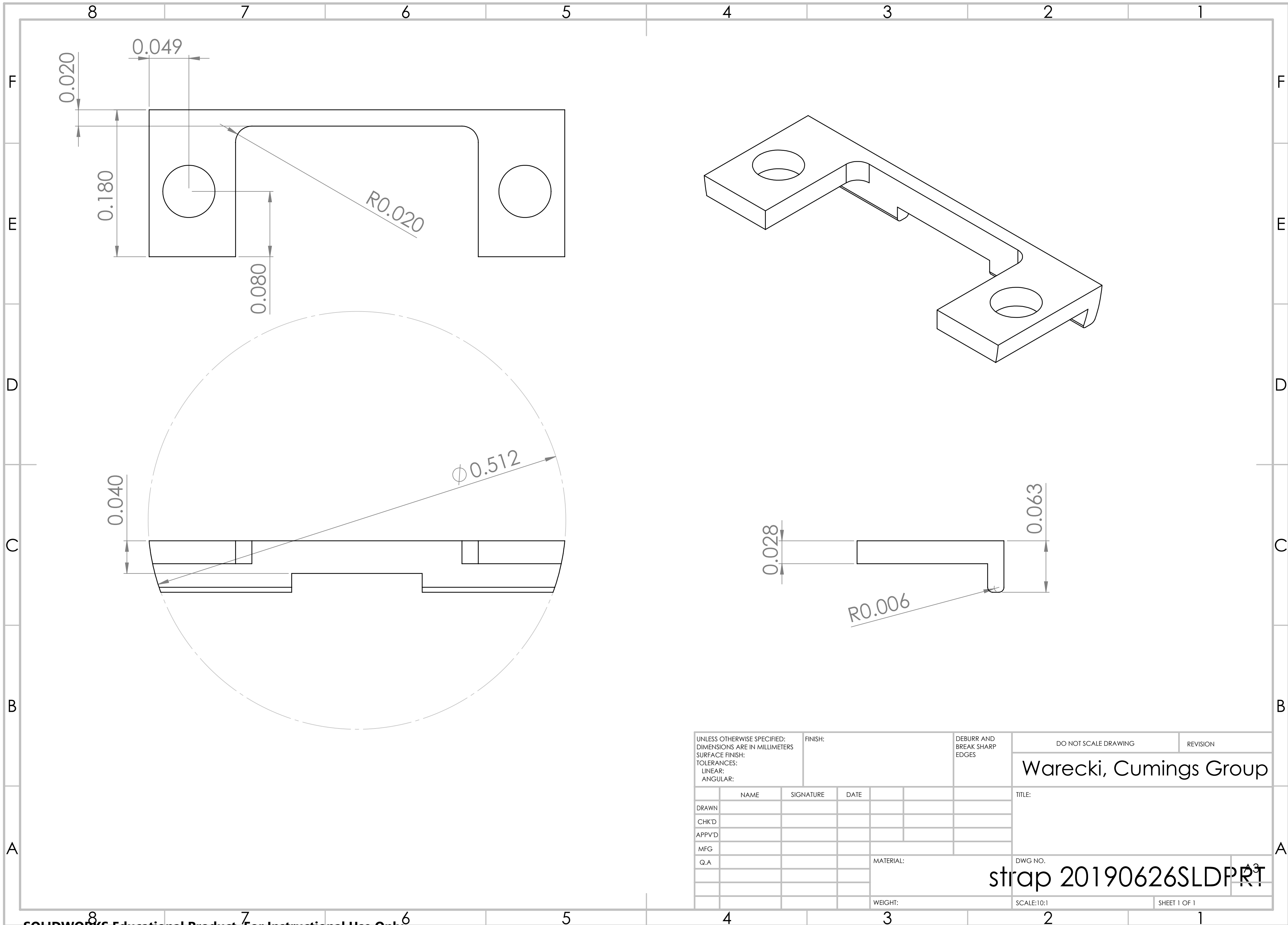

SOLIDWORKS Educational Product. For Instructional Use Only.

Tolerances:
x,y: +/- 1% NLT 0.005"
z(thickness): +/- 10%

*Piece to piece variation needs to be +/- 0.001"
preferrably expressed as +0.002" -0.000"

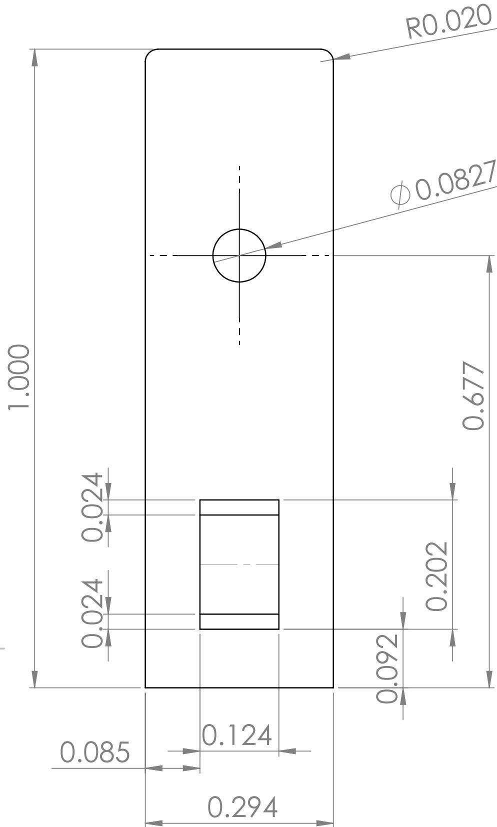

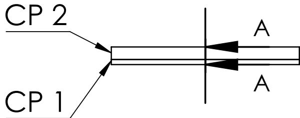

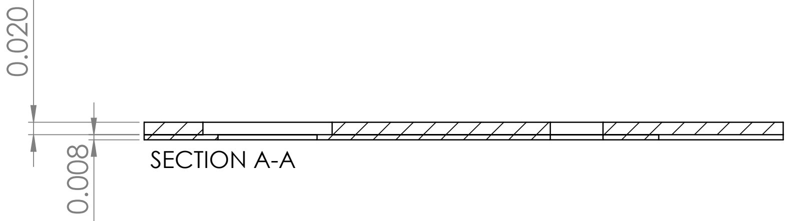

SECTION A-A

UNLESS OTHERWISE SPECIFIED: DIMENSIONS ARE IN MILLIMETERS SURFACE FINISH: TOLERANCES: LINEAR: ANGULAR:	FINISH:	DEBURR AND BREAK SHARP EDGES	DO NOT SCALE DRAWING	REVISION
			Zoey Warecki, Cumings Group	
	NAME / SIGNATURE / DATE		TITLE:	
DRAWN				
CHK'D				
APPV'D				
MFG				
Q.A		MATERIAL:	DWG NO. layered chip 20180403	A3
		WEIGHT:	SCALE:5:1	SHEET 1 OF 1

SOLIDWORKS Educational Product. For Instructional Use Only

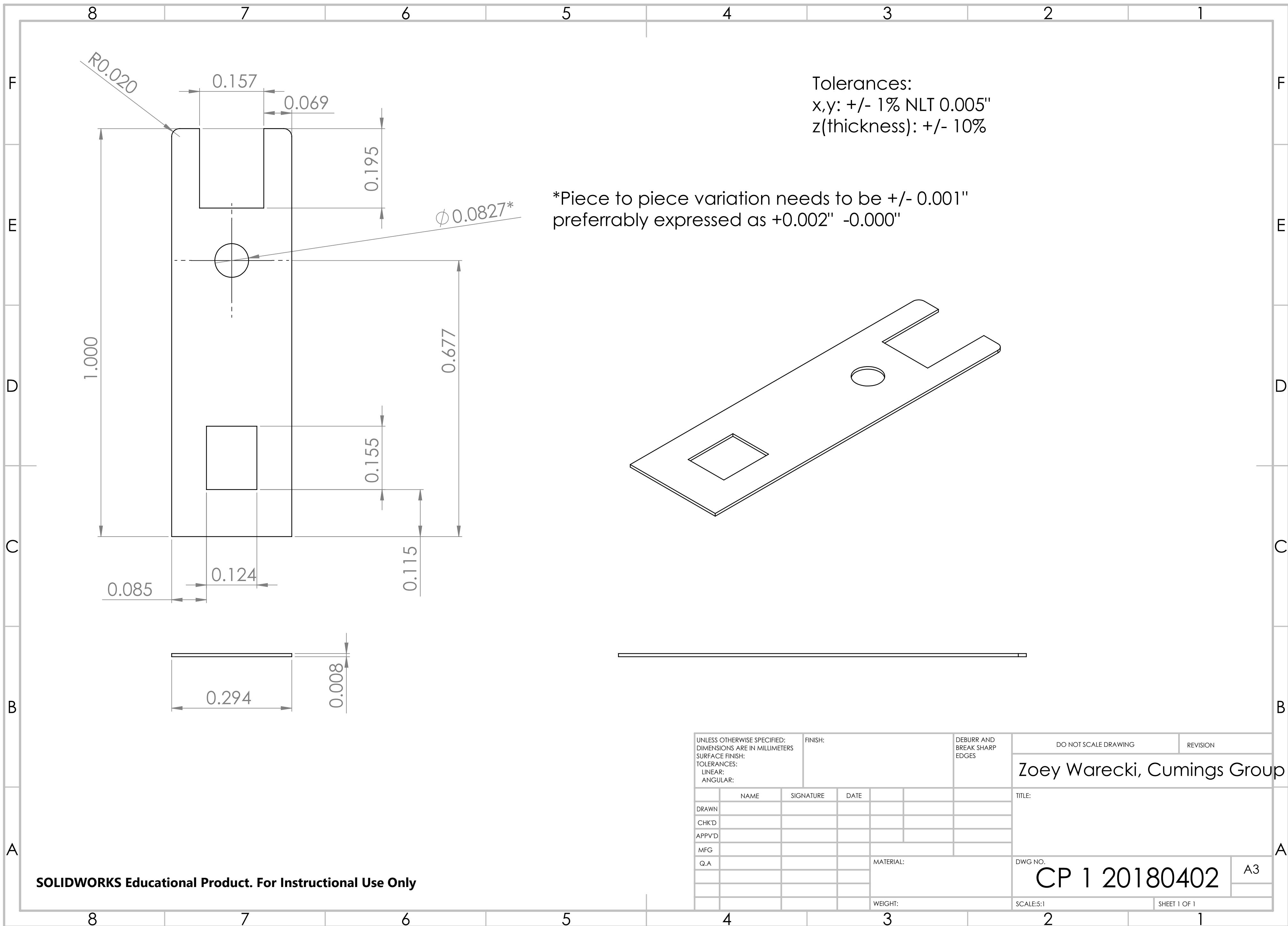
R0.020
0.157
0.069
0.195
⌀0.0827*
1.000
0.677
0.155
0.115
0.085
0.124
0.294
0.008
Tolerances:
x,y: +/- 1% NLT 0.005"
z(thickness): +/- 10%
*Piece to piece variation needs to be +/- 0.001"
preferrably expressed as +0.002" -0.000"
UNLESS OTHERWISE SPECIFIED:
DIMENSIONS ARE IN MILLIMETERS
SURFACE FINISH:
TOLERANCES:
LINEAR:
ANGULAR:
FINISH:
DEBURR AND BREAK SHARP EDGES
DO NOT SCALE DRAWING
REVISION
Zoey Warecki, Cumings Group
NAME
SIGNATURE
DATE
TITLE:
DRAWN
CHK'D
APPV'D
MFG
Q.A
MATERIAL:
DWG NO.
CP 1 20180402
A3
WEIGHT:
SCALE:5:1
SHEET 1 OF 1
SOLIDWORKS Educational Product. For Instructional Use Only

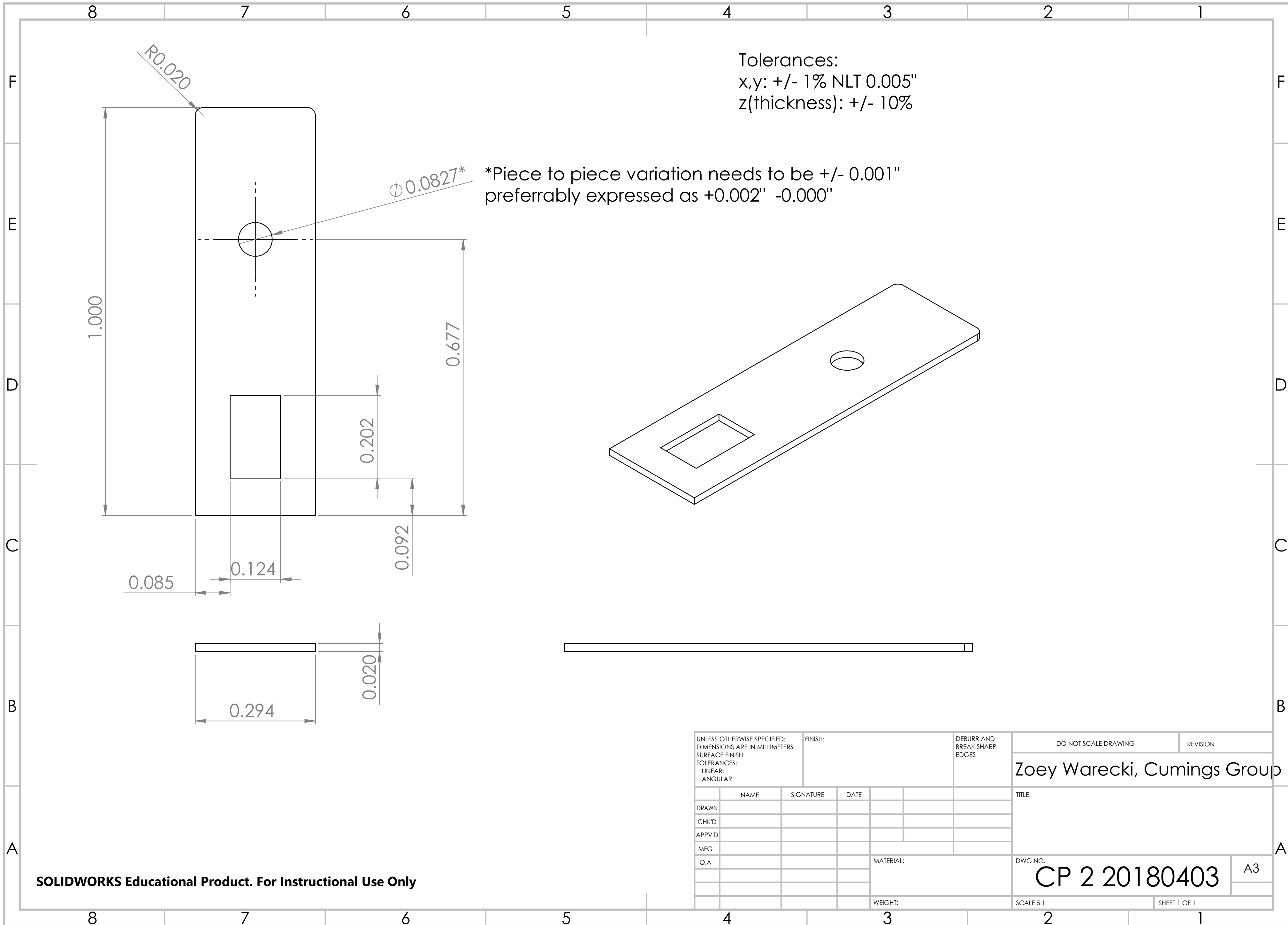
Tolerances:
x,y: +/- 1% NLT 0.005"
z(thickness): +/- 10%
*Piece to piece variation needs to be +/- 0.001"
preferrably expressed as +0.002" -0.000"
R0.020
ϕ0.0827*
1.000
0.677
0.202
0.092
0.124
0.085
0.020
0.294
UNLESS OTHERWISE SPECIFIED:
DIMENSIONS ARE IN MILLIMETERS
SURFACE FINISH:
TOLERANCES:
LINEAR:
ANGULAR:
FINISH:
DEBURR AND BREAK SHARP EDGES
DO NOT SCALE DRAWING
REVISION
Zoey Warecki, Cumings Group
NAME
SIGNATURE
DATE
DRAWN
CHK'D
APPV'D
MFG
Q.A
TITLE:
MATERIAL:
DWG NO.
CP 2 20180403
A3
WEIGHT:
SCALE:5:1
SHEET 1 OF 1
SOLIDWORKS Educational Product. For Instructional Use Only

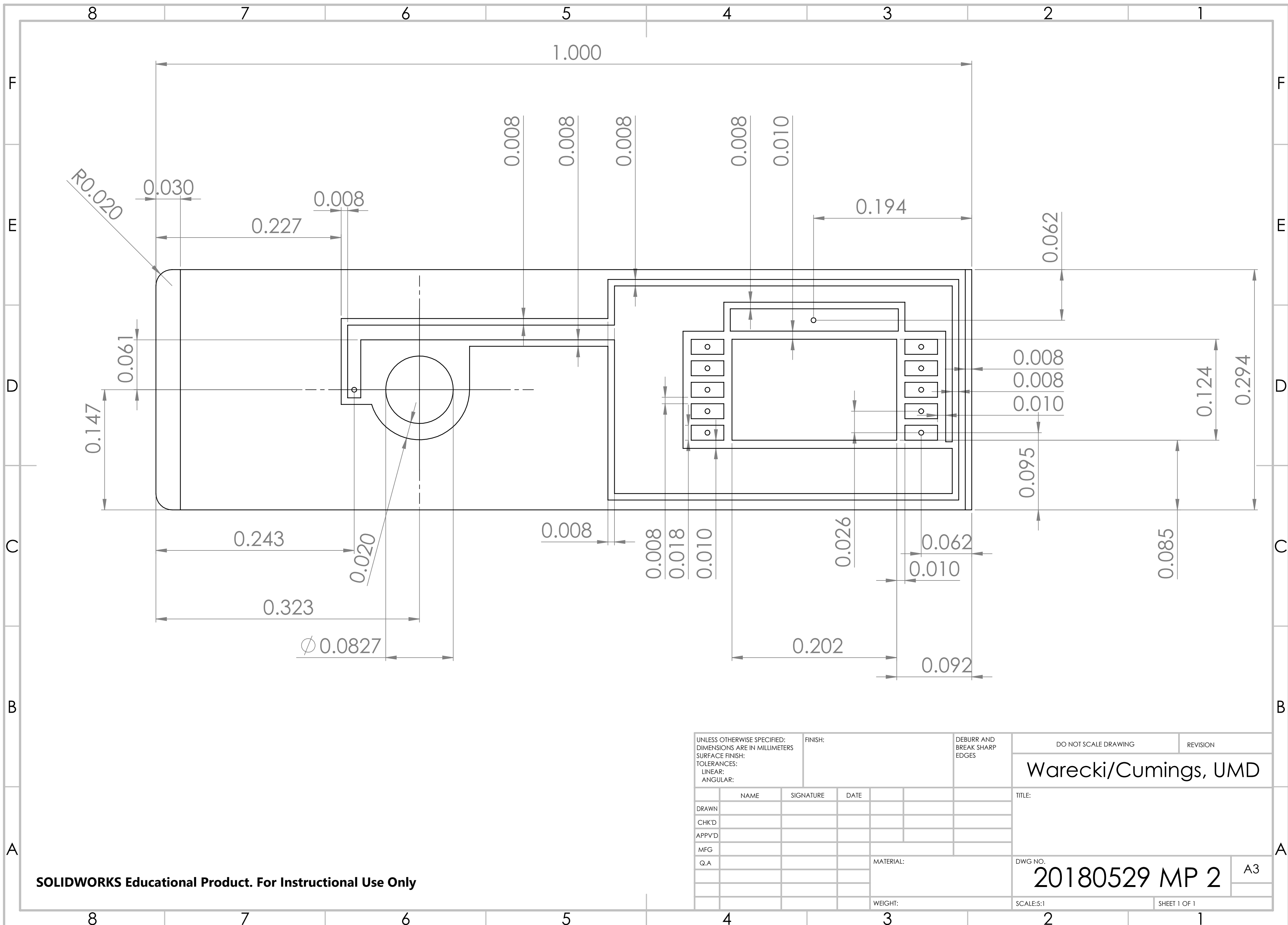

1.000
R0.020
0.030
0.008
0.227
0.008
0.008
0.008
0.008
0.010
0.194
0.062
0.061
0.147
0.008
0.008
0.010
0.124
0.294
0.095
0.243
0.020
0.008
0.008
0.018
0.010
0.026
0.062
0.010
0.085
0.323
∅0.0827
0.202
0.092
UNLESS OTHERWISE SPECIFIED:
DIMENSIONS ARE IN MILLIMETERS
SURFACE FINISH:
TOLERANCES:
LINEAR:
ANGULAR:
FINISH:
DEBURR AND BREAK SHARP EDGES
DO NOT SCALE DRAWING
REVISION
Warecki/Cumings, UMD
NAME
SIGNATURE
DATE
TITLE:
DRAWN
CHK'D
APPV'D
MFG
Q.A
MATERIAL:
DWG NO.
20180529 MP 2
A3
WEIGHT:
SCALE:5:1
SHEET 1 OF 1
SOLIDWORKS Educational Product. For Instructional Use Only

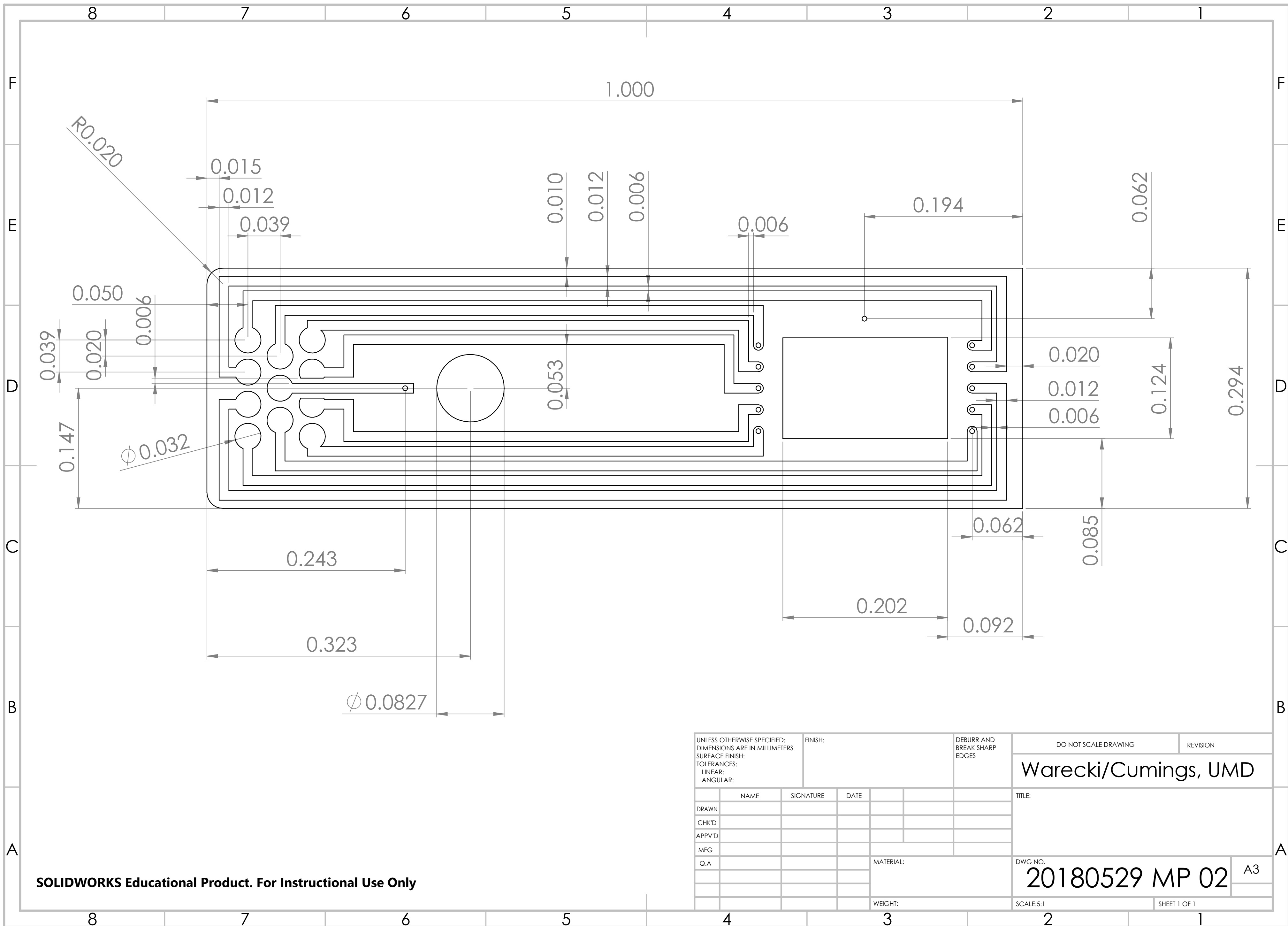
1.000
R0.020
0.015
0.012
0.039
0.010
0.012
0.006
0.006
0.194
0.062
0.050
0.006
0.039
0.020
0.053
0.020
0.012
0.006
0.124
0.294
0.147
∅0.032
0.062
0.085
0.243
0.202
0.092
0.323
∅0.0827
UNLESS OTHERWISE SPECIFIED:
DIMENSIONS ARE IN MILLIMETERS
SURFACE FINISH:
TOLERANCES:
LINEAR:
ANGULAR:
FINISH:
DEBURR AND BREAK SHARP EDGES
DO NOT SCALE DRAWING
REVISION
Warecki/Cumings, UMD
NAME
SIGNATURE
DATE
DRAWN
CHK'D
APPV'D
MFG
Q.A
TITLE:
MATERIAL:
DWG NO.
20180529 MP 02
A3
WEIGHT:
SCALE:5:1
SHEET 1 OF 1
SOLIDWORKS Educational Product. For Instructional Use Only

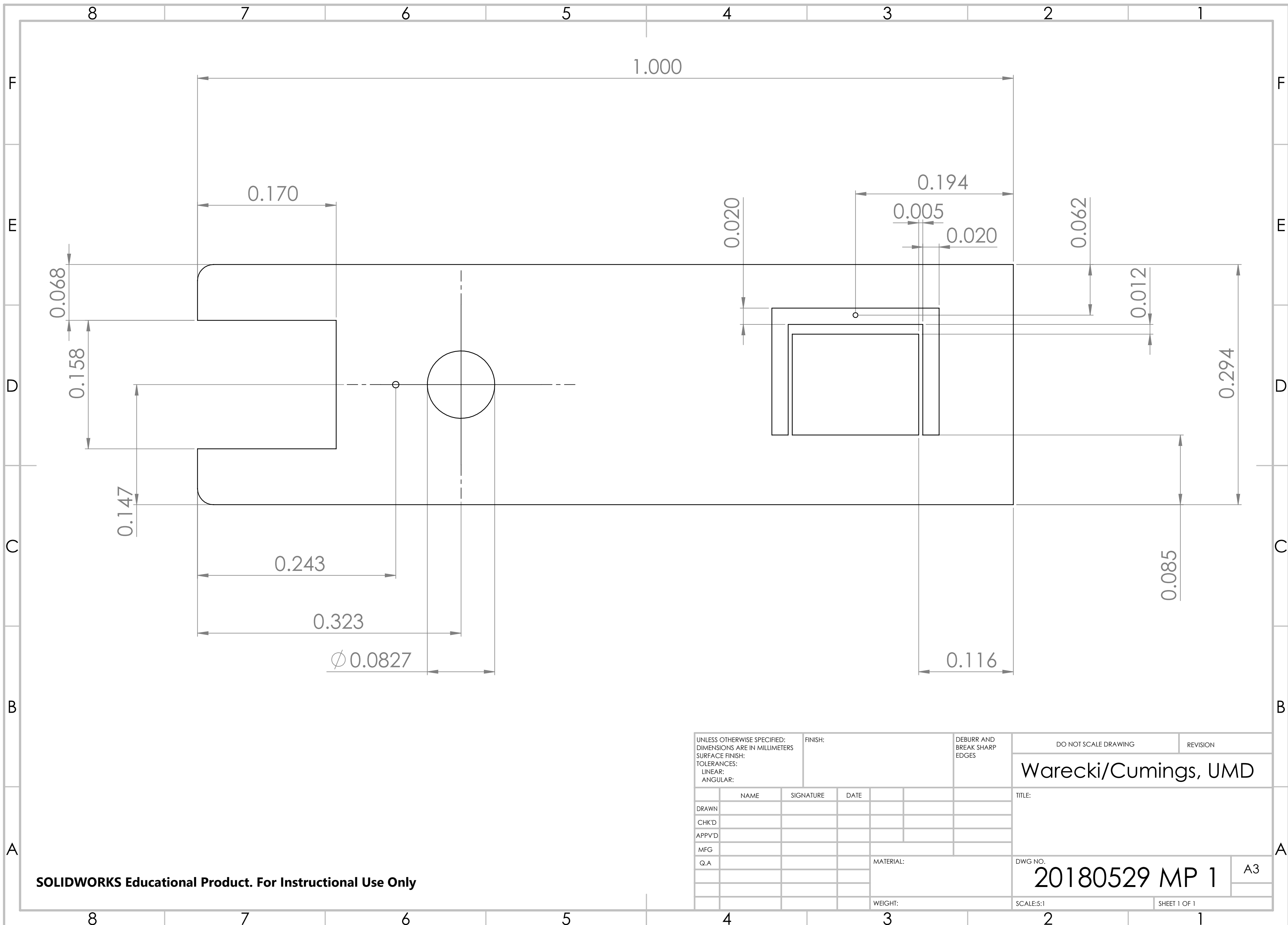
1.000
0.170
0.194
0.005
0.020
0.020
0.062
0.012
0.068
0.158
0.294
0.147
0.085
0.243
0.323
∅0.0827
0.116
UNLESS OTHERWISE SPECIFIED:
DIMENSIONS ARE IN MILLIMETERS
SURFACE FINISH:
TOLERANCES:
LINEAR:
ANGULAR:
FINISH:
DEBURR AND BREAK SHARP EDGES
DO NOT SCALE DRAWING
REVISION
Warecki/Cumings, UMD
NAME
SIGNATURE
DATE
TITLE:
DRAWN
CHK'D
APPV'D
MFG
Q.A
MATERIAL:
DWG NO.
20180529 MP 1
A3
WEIGHT:
SCALE:5:1
SHEET 1 OF 1
SOLIDWORKS Educational Product. For Instructional Use Only

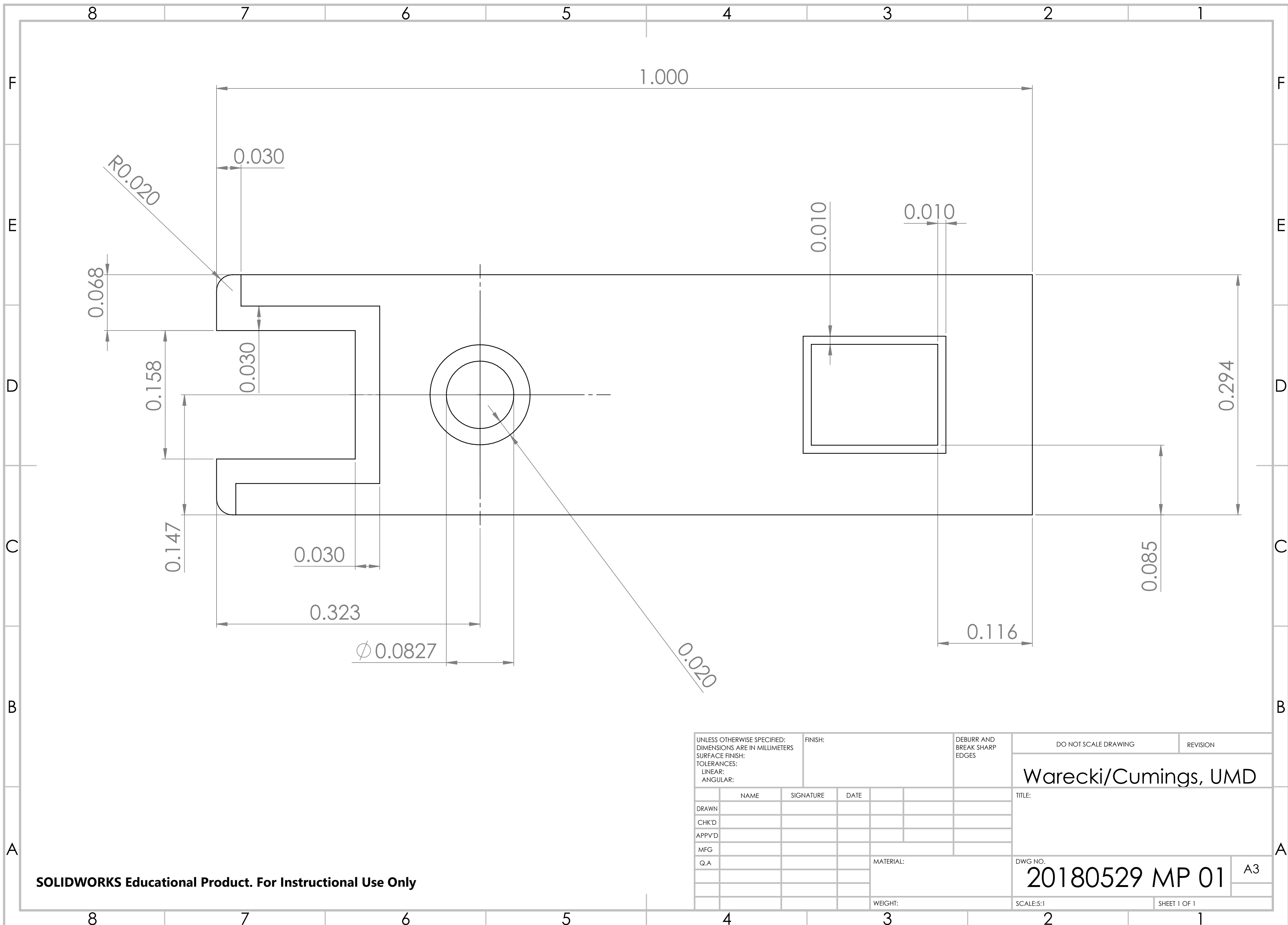
1.000
0.030
R0.020
0.010
0.010
0.068
0.030
0.158
0.294
0.147
0.030
0.085
0.323
0.116
∅0.0827
0.020
UNLESS OTHERWISE SPECIFIED:
DIMENSIONS ARE IN MILLIMETERS
SURFACE FINISH:
TOLERANCES:
LINEAR:
ANGULAR:
FINISH:
DEBURR AND BREAK SHARP EDGES
DO NOT SCALE DRAWING
REVISION
Warecki/Cumings, UMD
NAME
SIGNATURE
DATE
DRAWN
CHK'D
APPV'D
MFG
Q.A
TITLE:
MATERIAL:
DWG NO.
20180529 MP 01
A3
WEIGHT:
SCALE:5:1
SHEET 1 OF 1
SOLIDWORKS Educational Product. For Instructional Use Only

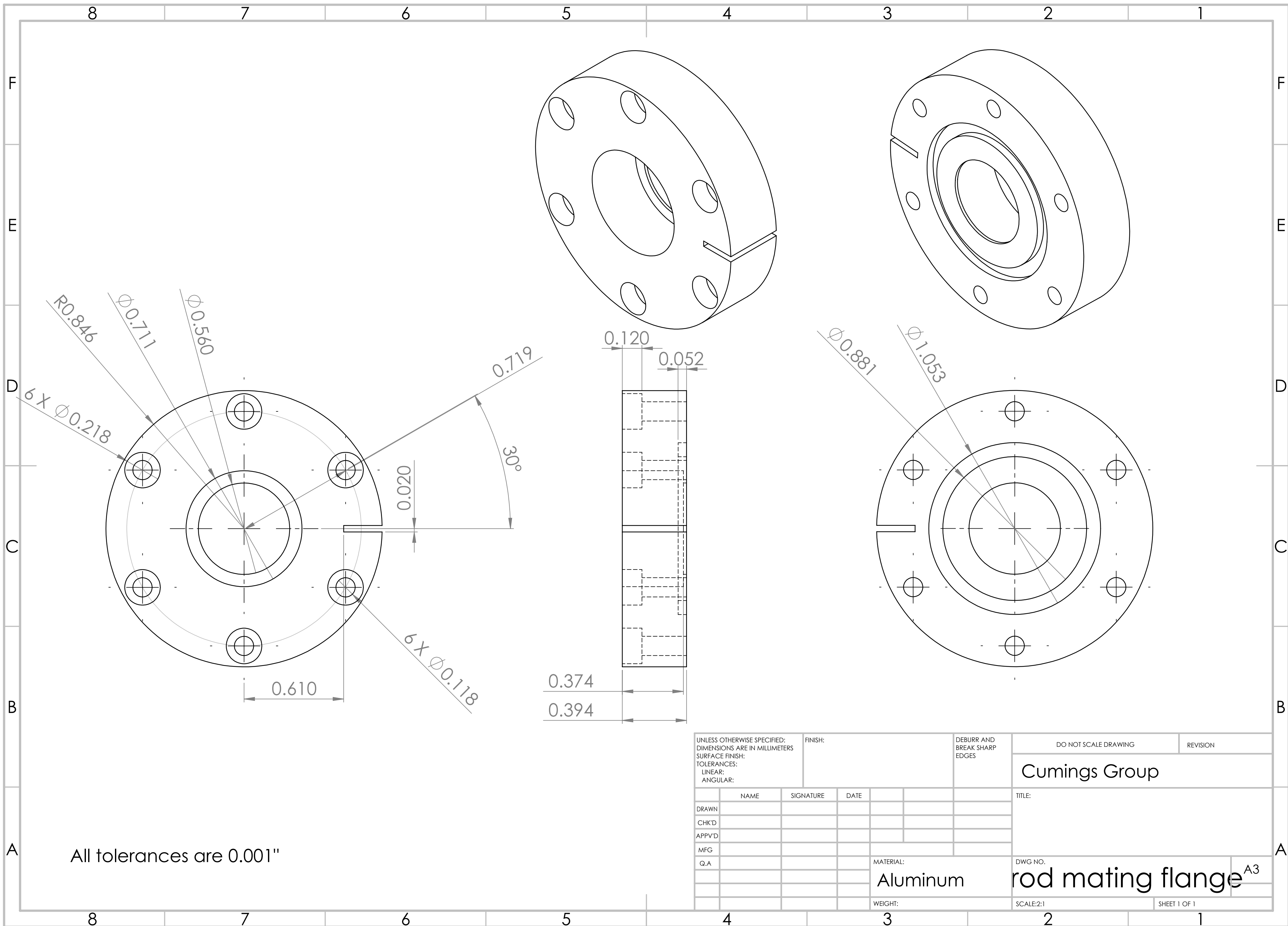

8
7
6
5
4
3
2
1
F
E
D
C
B
A
R0.846
⌀0.711
⌀0.560
6 X ⌀0.218
0.719
30°
0.020
0.610
6 X ⌀0.118
0.120
0.052
0.374
0.394
⌀0.881
⌀1.053
All tolerances are 0.001"
UNLESS OTHERWISE SPECIFIED:
DIMENSIONS ARE IN MILLIMETERS
SURFACE FINISH:
TOLERANCES:
LINEAR:
ANGULAR:
FINISH:
DEBURR AND BREAK SHARP EDGES
DO NOT SCALE DRAWING
REVISION
Cumings Group
NAME
SIGNATURE
DATE
DRAWN
CHK'D
APPV'D
MFG
Q.A
TITLE:
MATERIAL:
Aluminum
DWG NO.
rod mating flange
A3
WEIGHT:
SCALE:2:1
SHEET 1 OF 1

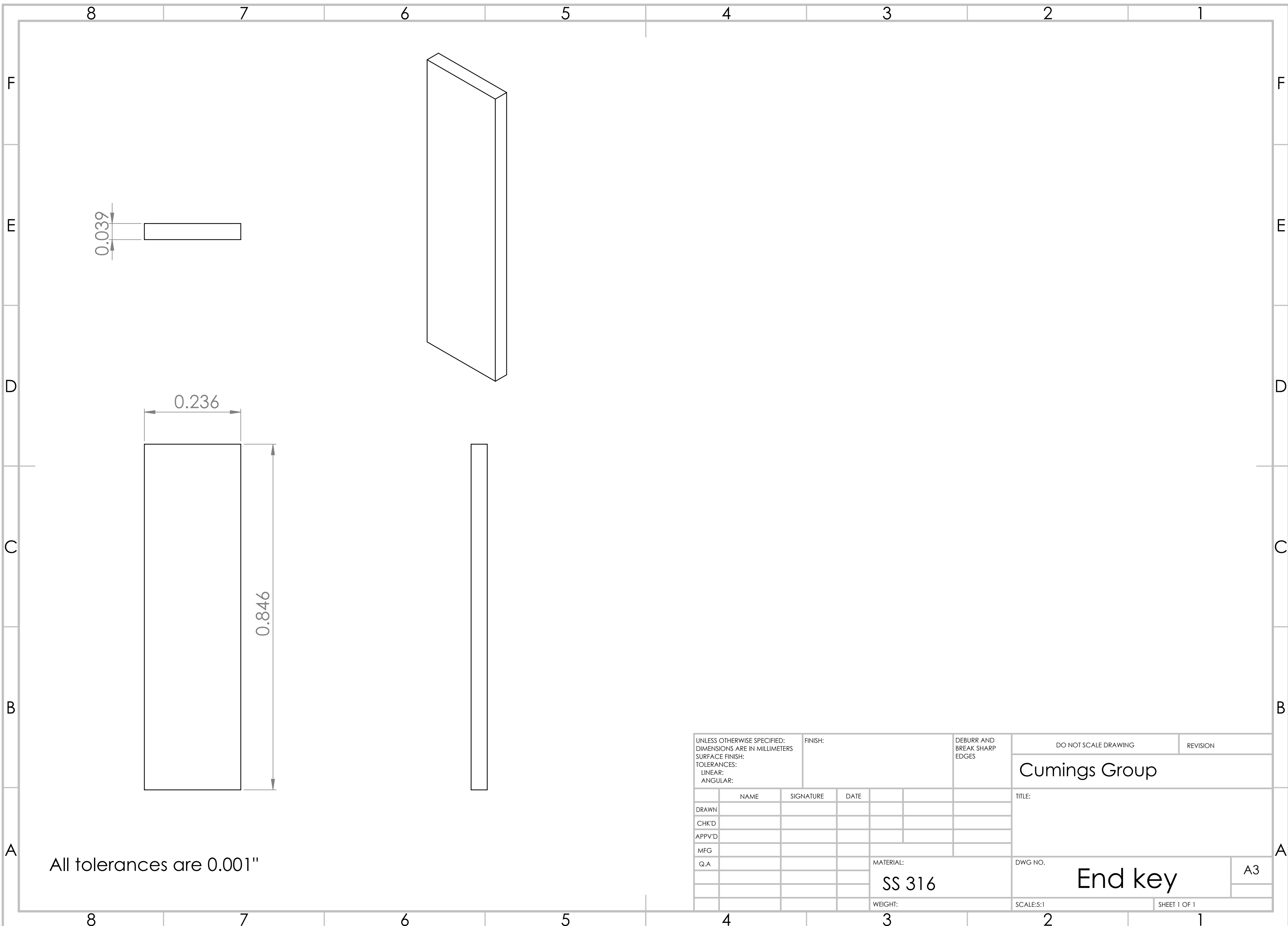
0.039
0.236
0.846
All tolerances are 0.001"
UNLESS OTHERWISE SPECIFIED:
DIMENSIONS ARE IN MILLIMETERS
SURFACE FINISH:
TOLERANCES:
LINEAR:
ANGULAR:
FINISH:
DEBURR AND BREAK SHARP EDGES
DO NOT SCALE DRAWING
REVISION
Cumings Group
NAME
SIGNATURE
DATE
DRAWN
CHK'D
APPV'D
MFG
Q.A
TITLE:
MATERIAL:
SS 316
WEIGHT:
DWG NO.
End key
A3
SCALE:5:1
SHEET 1 OF 1

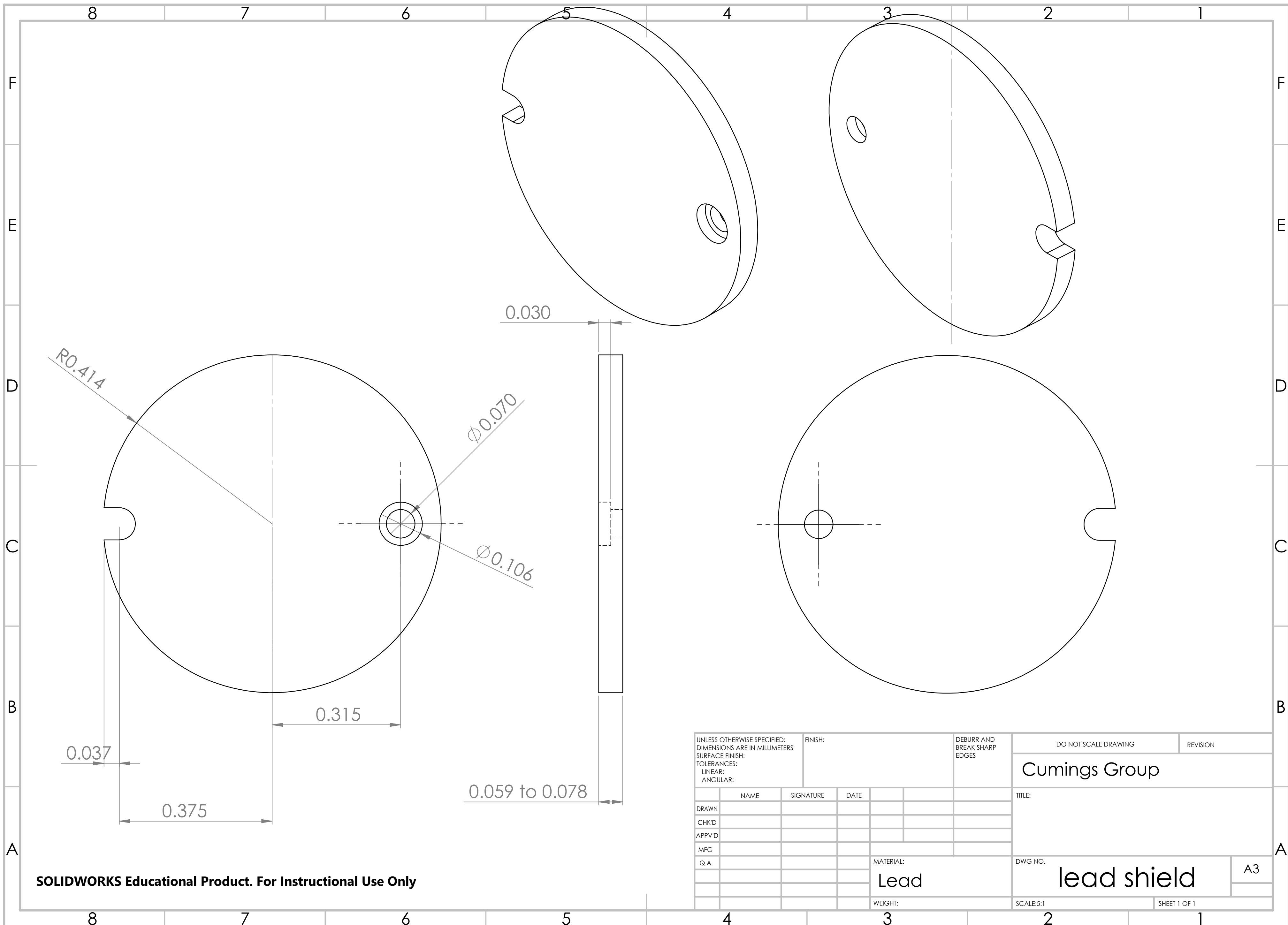
R0.414
∅0.070
∅0.106
0.315
0.037
0.375
0.030
0.059 to 0.078
UNLESS OTHERWISE SPECIFIED:
DIMENSIONS ARE IN MILLIMETERS
SURFACE FINISH:
TOLERANCES:
LINEAR:
ANGULAR:
FINISH:
DEBURR AND BREAK SHARP EDGES
DO NOT SCALE DRAWING
REVISION
Cumings Group
NAME
SIGNATURE
DATE
DRAWN
CHK'D
APPV'D
MFG
Q.A
TITLE:
MATERIAL:
Lead
WEIGHT:
DWG NO.
lead shield
A3
SCALE:5:1
SHEET 1 OF 1
SOLIDWORKS Educational Product. For Instructional Use Only

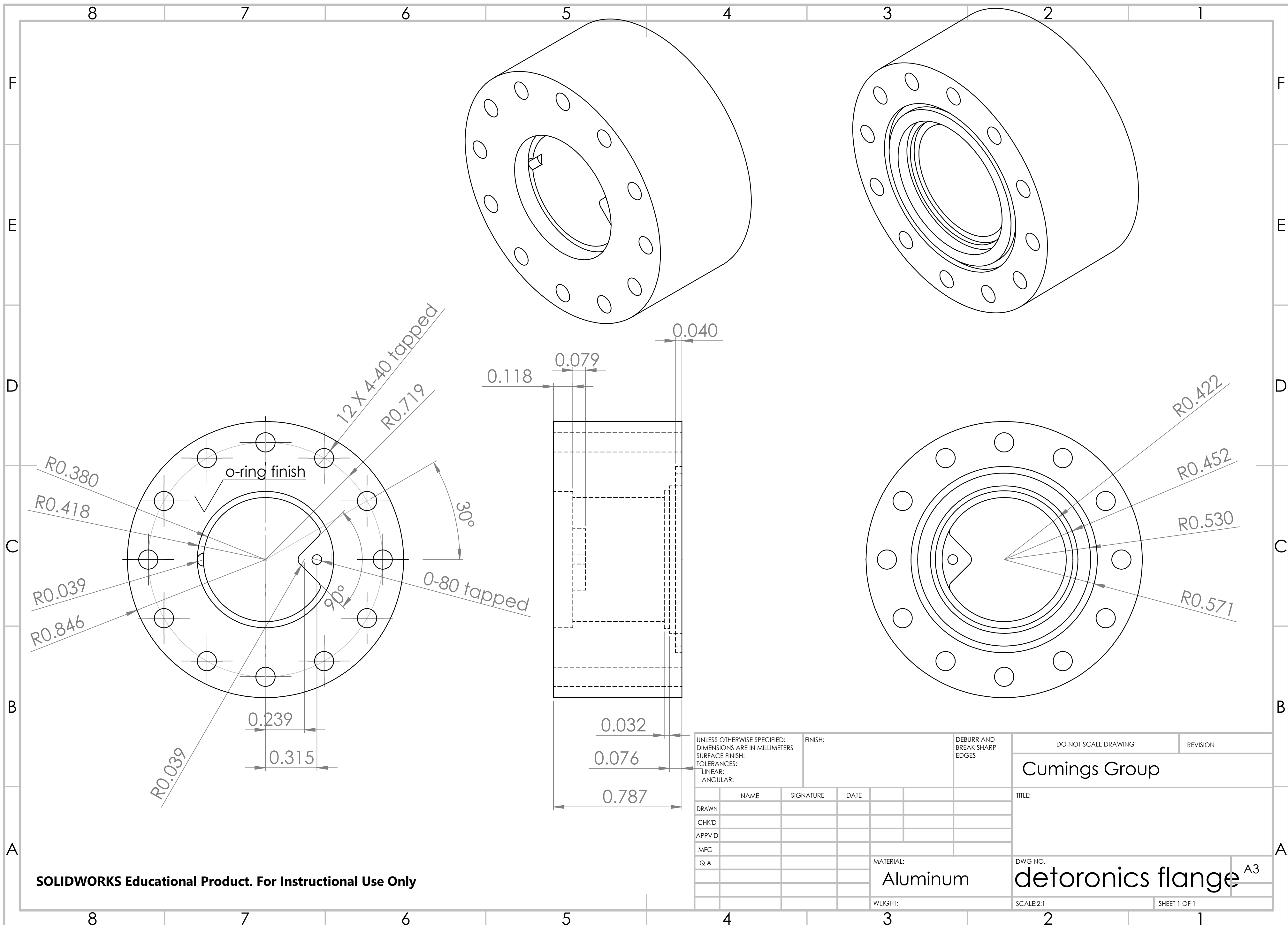

12 X 4-40 tapped
R0.719
R0.380
o-ring finish
R0.418
30°
R0.039
0-80 tapped
90°
R0.846
0.239
0.315
R0.039
0.118
0.079
0.040
0.032
0.076
0.787
R0.422
R0.452
R0.530
R0.571
UNLESS OTHERWISE SPECIFIED:
DIMENSIONS ARE IN MILLIMETERS
SURFACE FINISH:
TOLERANCES:
LINEAR:
ANGULAR:
FINISH:
DEBURR AND BREAK SHARP EDGES
DO NOT SCALE DRAWING
REVISION
Cumings Group
NAME
SIGNATURE
DATE
DRAWN
CHK'D
APPV'D
MFG
Q.A
TITLE:
MATERIAL:
Aluminum
DWG NO.
detoronics flange
A3
WEIGHT:
SCALE:2:1
SHEET 1 OF 1
SOLIDWORKS Educational Product. For Instructional Use Only

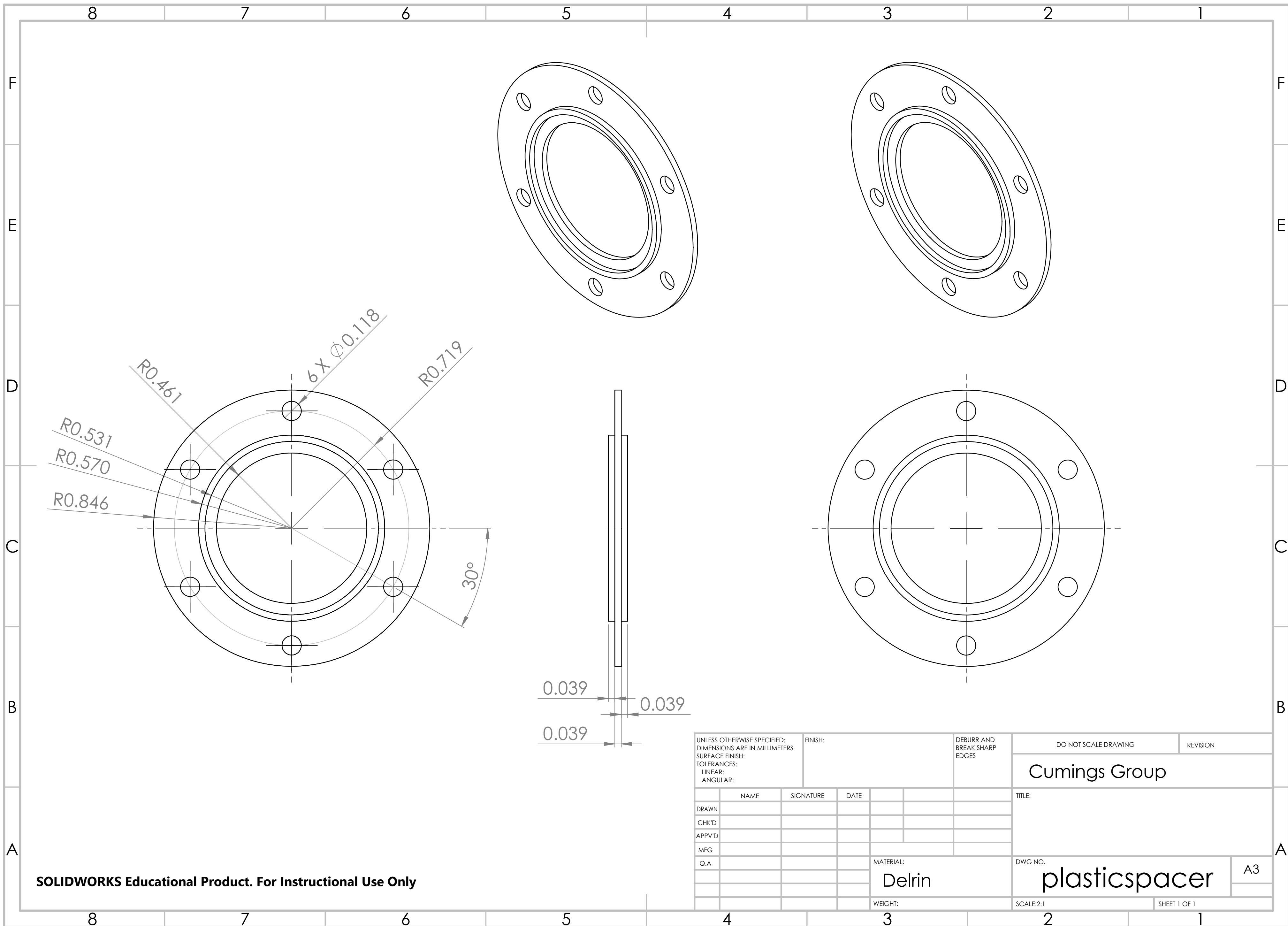

R0.461
6 X ∅0.118
R0.719
R0.531
R0.570
R0.846
30°
0.039
0.039
0.039
UNLESS OTHERWISE SPECIFIED:
DIMENSIONS ARE IN MILLIMETERS
SURFACE FINISH:
TOLERANCES:
LINEAR:
ANGULAR:
FINISH:
DEBURR AND BREAK SHARP EDGES
DO NOT SCALE DRAWING
REVISION
Cumings Group
NAME
SIGNATURE
DATE
TITLE:
DRAWN
CHK'D
APPV'D
MFG
Q.A
MATERIAL:
Delrin
DWG NO.
plasticspacer
A3
WEIGHT:
SCALE:2:1
SHEET 1 OF 1
SOLIDWORKS Educational Product. For Instructional Use Only

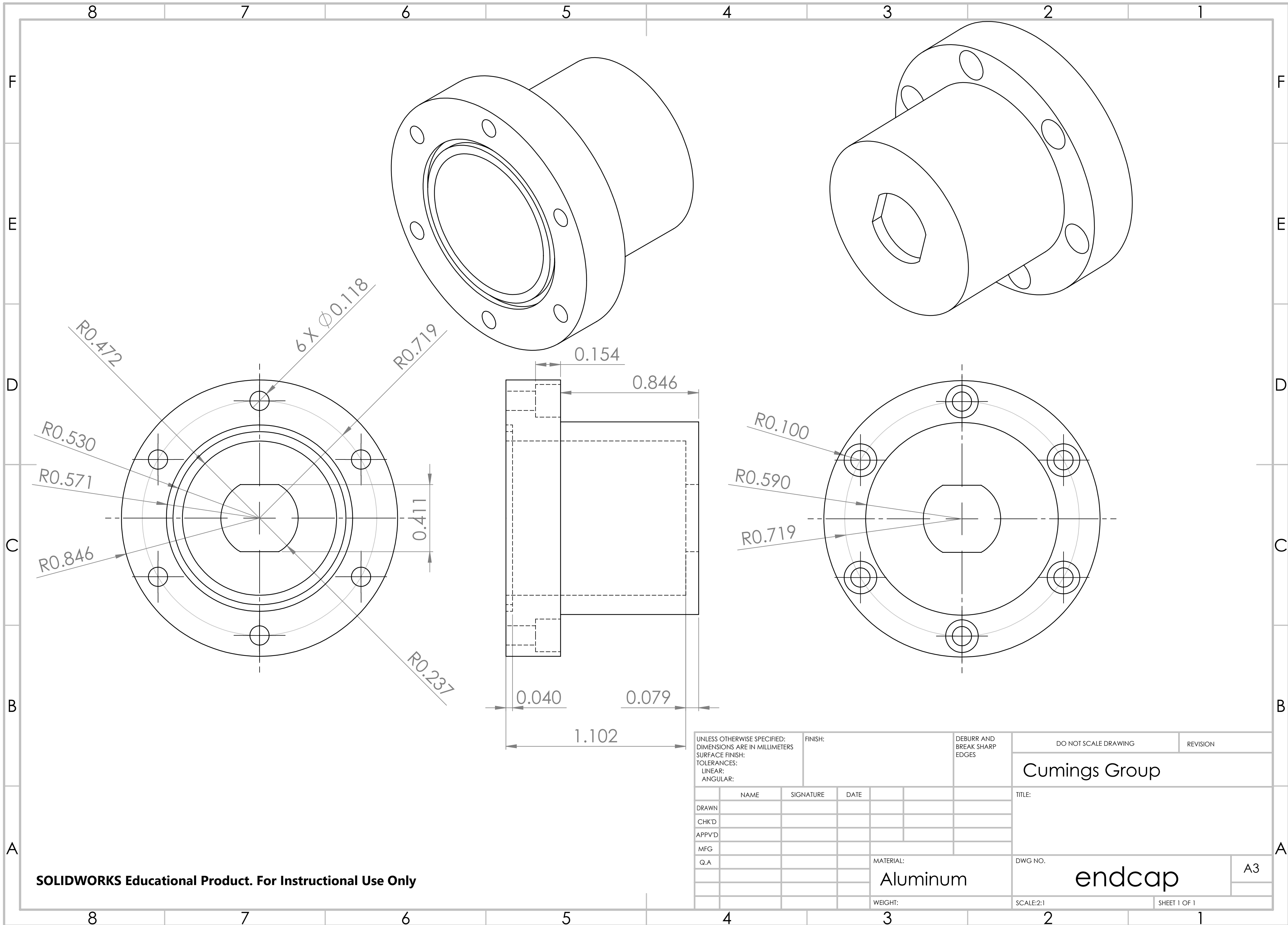

6 X ⌀0.118
R0.472
R0.719
R0.530
R0.571
R0.846
R0.237
0.411
0.154
0.846
0.040
0.079
1.102
R0.100
R0.590
R0.719
UNLESS OTHERWISE SPECIFIED:
DIMENSIONS ARE IN MILLIMETERS
SURFACE FINISH:
TOLERANCES:
LINEAR:
ANGULAR:
FINISH:
DEBURR AND BREAK SHARP EDGES
DO NOT SCALE DRAWING
REVISION
Cumings Group
NAME
SIGNATURE
DATE
TITLE:
DRAWN
CHK'D
APPV'D
MFG
Q.A
MATERIAL:
Aluminum
DWG NO.
endcap
A3
WEIGHT:
SCALE:2:1
SHEET 1 OF 1
SOLIDWORKS Educational Product. For Instructional Use Only

Bibliography

[1] Intergovernmental Panel on Climate Change. Fifth Climate Change Assesment Report. Technical report, 2014.

[2] Fabrizio Roccaforte, Patrick Fiorenza, Giuseppe Greco, Raffaella Lo Nigro, Filippo Giannazzo, Ferdinando Iucolano, and Mario Saggio. Emerging trends in wide band gap semiconductors (SiC and GaN) technology for power devices. *Microelectronic Engineering*, 187-188:66–77, 2018.

[3] Matteo Meneghini, Gaudenzio Meneghesso, and Enrico Znoni. *Power GaN Devices*. Springer, 2017.

[4] Yuhao Zhang, Armin Dadgar, and Tomas Palacios. Gallium nitride vertical power devices on foreign substrates: a review and outlook. *Journal of Physics D: Applied Physics*, 51:273001, 2018.

[5] S.M. Sze. *Semiconductor Devices, Physics and Technology*. John Wiley & Sons, Inc., 2nd edition, 2002.

[6] Gerold W. Neudeck and Robert F. Pierret. *Semiconductor Fundamentals*. Addison Wesley Publishing Company, 2nd edition, 1989.

[7] Philip G Neudeck, Robert S. Okojie, and Liang-Yu Chen. High-temperature Electronics - A Role for Wide Bandgap Semiconductors? *Proceedings of the IEEE*, 90, 2002.

[8] G. Longobardi. GaN for power devices: Benefits, applications, and normally-off technologies. In *Proceedings of the International Semiconductor Conference, CAS*, pages 11–18, 2017.

[9] Nariaki Ikeda, Syuusuke Kaya, Jiang Li, Yoshihiro Sato, Sadahiro Kato, and Seikoh Yoshida. High power AlGaN/GaN HFET with a high breakdown voltage of over 1.8 kV on 4 inch Si substrates and the suppression of current collapse. *Proceedings of the International Symposium on Power Semiconductor Devices and ICs*, pages 287–290, 2008.

[10] Allan H. Johnston. Radiation effects in optoelectronic devices. *IEEE Transactions on Nuclear Science*, 60(3):2054–2073, 2013.

[11] E.G. Stassinopoulos and James P. Raymond. The space radiation environment. *IEEE Transactions on Nuclear Science*, 12(5):1–17, 1988.

[12] Stephen J Pearton, Richard Deist, Fan Ren, Lu Liu, Alexander Y Polyakov, and Jihyun Kim. Review of radiation damage in GaN-based materials and devices. *J. Vac. Sci. Technol. A*, 31:50801, 2013.

[13] S. J. Pearton, F. Ren, Erin Patrick, M. E. Law, and Alexander Y. Polyakov. Review—Ionizing Radiation Damage Effects on GaN Devices. *ECS Journal of Solid State Science and Technology*, 5(2):Q35–Q60, 2016.

[14] A. Ionascut-Nedelcescu, C. Carlone, A. Houdayer, H. J. Von Bardeleben, J. L. Cantin, and S. Raymond. Radiation hardness of gallium nitride. *IEEE Transactions on Nuclear Science*, 49 I(6):2733–2738, 2002.

[15] D. F. Storm, M. T. Hardy, D. S. Katzer, N. Nepal, B. P. Downey, D. J. Meyer, Thomas O. McConkie, Lin Zhou, and David J. Smith. Critical issues for homoepitaxial GaN growth by molecular beam epitaxy on hydride vapor-phase epitaxy-grown GaN substrates. *Journal of Crystal Growth*, 456:121–132, 2016.

[16] Atsunori Tanaka, Woojin Choi, Renjie Chen, Ren Liu, William M. Mook, Katherine L. Jungjohann, Paul K.L. Yu, and Shadi A. Dayeh. Structural and electrical characterization of thick GaN layers on Si, GaN, and engineered substrates. *Journal of Applied Physics*, 125(8), 2019.

[17] Tanya Paskova and Keith R Evans. GaN Substrates — Progress , Status , and Prospects. *IEEE Journal of Selected Topics in Quantum Electronics*, 15(4):1041–1052, 2009.

[18] Houqiang Fu, Xuanqi Huang, Hong Chen, Zhijian Lu, Xiaodong Zhang, and Yuji Zhao. Effect of buffer layer design on vertical GaN-on-GaN p-n and schottky power diodes. *IEEE Electron Device Letters*, 38(6):763–766, 2017.

[19] Y Cao, R Chu, R Li, M Chen, R Chang, and B Hughes. High-voltage vertical GaN Schottky diode enabled by low-carbon metal-organic chemical vapor deposition growth. *Appl. Phys. Lett*, 108:62103, 2016.

[20] A. M. Armstrong, A. A. Allerman, A. J. Fischer, M. P. King, M. S. Van Heukelom, M. W. Moseley, R. J. Kaplar, J. J. Wierer, M. H. Crawford, and J. R. Dickerson. High voltage and high current density vertical GaN power diodes. *Electronics Letters*, 52(13):1170–1171, 2016.

[21] Jonathan J. Wierer, Jeramy R. DIckerson, Andrew A. Allerman, Andrew M. Armstrong, Mary H. Crawford, and Robert J. Kaplar. Simulations of Junction

Termination Extensions in Vertical GaN Power Diodes. *IEEE Transactions on Electron Devices*, 64(5):2291–2297, 2017.

[22] Leonid Chernyak, Andrei Osinsky, Henryk Temkin, J W Yang, Q Chen, and M Asif Khan. Electron beam induced current measurements of minority carrier diffusion length in gallium nitride. *Citation: Appl. Phys. Lett*, 69:2531, 1996.

[23] E. B. Yakimov. What is the real value of diffusion length in GaN? *Journal of Alloys and Compounds*, 627:344–351, 2015.

[24] J.-M. Tarascon and M. Armand. Issues and challenges facing rechargeable lithium batteries. *Nature*, 414:359–367, 2001.

[25] M.S. Whittingham. Electrical Energy Storage and Intercalation Chemistry. *Science*, 192, 1976.

[26] K. Mizushima, P.C. Jones, P.J. Wiseman, and J.B. Goodenough. LixCoO2: A New Cathode Material for Batteries of High Energy Density. *Solid State Ionics*, 3-4:171–174, 1981.

[27] Jürgen Janek and Wolfgang G. Zeier. A solid future for battery development. *Nature Energy*, 1(9):1–4, 2016.

[28] Nitin A. Kaskhedikar and Joachim Maier. Lithium storage in carbon nanostructures. *Advanced Materials*, 21(25-26):2664–2680, 2009.

[29] Guangyuan Zheng, Seok Woo Lee, Zheng Liang, Hyun Wook Lee, Kai Yan, Hongbin Yao, Haotian Wang, Weiyang Li, Steven Chu, and Yi Cui. Interconnected hollow carbon nanospheres for stable lithium metal anodes. *Nature Nanotechnology*, 9(8):618–623, 2014.

[30] Jordi Cabana, Laure Monconduit, Dominique Larcher, and M. Rosa Palacín. Beyond intercalation-based Li-ion batteries: The state of the art and challenges of electrode materials reacting through conversion reactions. *Advanced Materials*, 22(35):170–192, 2010.

[31] Matthew T. McDowell, Seok Woo Lee, William D. Nix, and Yi Cui. 25th anniversary article: Understanding the lithiation of silicon and other alloying anodes for lithium-ion batteries. *Advanced Materials*, 25(36):4966–4985, 2013.

[32] Bin Wang, Bin Luo, Xianglong Li, and Linjie Zhi. The dimensionality of Sn anodes in Li-ion batteries. *Materials Today*, 15(12):544–552, 2012.

[33] Peter G. Bruce, Bruno Scrosati, and Jean-Marie Tarascon. Nanomaterials for rechargeable lithium batteries. *Angewandte Chemie*, 47(16):2930–46, 2008.

[34] Subrahmanyam Goriparti, Ermanno Miele, Francesco De Angelis, Enzo Di, Remo Proietti, and Claudio Capiglia. Review on recent progress of nanostructured anode materials for Li-ion batteries. *Journal of Power Sources*, 257:421–443, 2014.

[35] Gary W. Rubloff, Alexander C. Kozen, and Sang Bok Lee. From nanoscience to solutions in electrochemical energy storage. *Journal of Vacuum Science & Technology A: Vacuum, Surfaces, and Films*, 31(5):058503, 2013.

[36] Khim Karki, Yujie Zhu, Yihang Liu, Chuan Fu Sun, Liangbing Hu, Yuhuang Wang, Chunsheng Wang, and John Cumings. Hoop-strong nanotubes for battery electrodes. *ACS Nano*, 7(9):8295–8302, 2013.

[37] Jinyun Liu, Nan Li, Matthew D. Goodman, Hui Gang Zhang, Eric S. Epstein, Bo Huang, Zeng Pan, Jinwoo Kim, Jun Hee Choi, Xingjiu Huang, Jinhuai Liu, K. Jimmy Hsia, Shen J. Dillon, and Paul V. Braun. Mechanically and chemically robust sandwich-structured C@Si@C nanotube array Li-ion battery anodes. *ACS Nano*, 9(2):1985–1994, 2015.

[38] Chuan Fu Sun, Khim Karki, Zheng Jia, Hongwei Liao, Yin Zhang, Teng Li, Yue Qi, John Cumings, Gary W. Rubloff, and Yuhuang Wang. A beaded-string silicon anode. *ACS Nano*, 7(3):2717–2724, 2013.

[39] Hui Wu, Gerentt Chan, Jang Wook Choi, Ill Ryu, Yan Yao, Matthew T. Mcdowell, Seok Woo Lee, Ariel Jackson, Yuan Yang, Liangbing Hu, and Yi Cui. Stable cycling of double-walled silicon nanotube battery anodes through solid-electrolyte interphase control. *Nature Nanotechnology*, 7(5):310–315, 2012.

[40] Sung Yup Kim, Alireza Ostadhossein, Adri C.T. Van Duin, Xingcheng Xiao, Huajian Gao, and Yue Qi. Self-generated concentration and modulus gradient coating design to protect Si nano-wire electrodes during lithiation. *Physical Chemistry Chemical Physics*, 18(5):3706–3715, 2016.

[41] Jian Yu Huang, Li Zhong, Chong Min Wang, John P Sullivan, Wu Xu, Li Qiang Zhang, Scott X Mao, Nicholas S Hudak, Xiao Hua Liu, Arunkumar Subramanian, Hongyou Fan, Liang Qi, Akihiro Kushima, and Ju Li. In situ observation of the electrochemical lithiation of a single SnO2 nanowire electrode. *Science*, 330(December):1515–1520, 2010.

[42] Zhen Zhang and John T Yates. Band Bending in Semiconductors: Chemical and Physical Consequences at Surfaces and Interfaces. *Chemical Reviews*, 112, 2012.

[43] Zhi Li, Jia Ding, and David Mitlin. Tin and Tin Compounds for Sodium Ion Battery Anodes: Phase Transformations and Performance. *Accounts of Chemical Research*, 48(6):1657–1665, 2015.

[44] L. D. Ellis, T. D. Hatchard, and M. N. Obrovac. Reversible Insertion of Sodium in Tin. *Journal of The Electrochemical Society*, 159(11):A1801–A1805, 2012.

[45] Jiang Wei Wang, Xiao Hua Liu, Scott X. Mao, and Jian Yu Huang. Microstructural evolution of tin nanoparticles during in situ sodium insertion and extraction. *Nano Letters*, 12(11):5897–5902, 2012.

[46] Dawei Su, Chengyin Wang, Hyojun Ahn, and Guoxiu Wang. Octahedral tin dioxide nanocrystals as high capacity anode materials for Na-ion batteries. *Physical chemistry chemical physics : PCCP*, 15(30):12543–50, 2013.

[47] Dawei Su, Shixue Dou, and Guoxiu Wang. SnO2-graphene nanocomposites as anode materials for Na-ion batteries with enhanced electrochemical performances. *Chemical communications (Cambridge, England)*, 50(32):4192–5, 2014.

[48] J. R.Dahn I. A. Courtney. Electrochemical and In Situ X-Ray Diffraction Studies of the Reaction of Lithium with Tin Oxide Composites. *J. Electrochem. Soc.*, 144(6):2045–2052, 1997.

[49] Sung-Chieh Chao, Yu-Chan Yen, Yen-Fang Song, Yi-Ming Chen, Hung-Chun Wu, and Nae-Lih Wu. A study on the interior microstructures of working Sn particle electrode of Li-ion batteries by in situ X-ray transmission microscopy. *Electrochemistry Communications*, 12:234–237, 2010.

[50] J. Wang, F. Fan, Y. Liu, K. L. Jungjohann, S. W. Lee, S. X. Mao, X. Liu, and T. Zhu. Structural Evolution and Pulverization of Tin Nanoparticles during Lithiation-Delithiation Cycling. *Journal of the Electrochemical Society*, 161(11):F3019–F3024, 2014.

[51] Qianqian Li, Peng Wang, Qiong Feng, Minmin Mao, Jiabin Liu, Scott X. Mao, and Hongtao Wang. In Situ TEM on the reversibility of nanosized Sn anodes during the electrochemical reaction. *Chemistry of Materials*, 26(14):4102–4108, 2014.

[52] Matthew T. Janish, David T. Mackay, Yang Liu, Katherine L. Jungjohann, C. Barry Carter, and M. Grant Norton. TEM in situ lithiation of tin nanoneedles for battery applications. *Journal of Materials Science*, 51(1):589–602, 2015.

[53] Andrew J. A.J. Leenheer, John P. Sullivan, Michael J. Shaw, and C. Thomas Harris. A Sealed Liquid Cell for In Situ Transmission Electron Micorsocpy of Controlled Electrochemical Processes. *Journal of Microelectromechnical systems*, 24(4):1061–1068, 2015.

[54] Andrew J. Leenheer, Katherine L. Jungjohann, Kevin R. Zavadil, John P. Sullivan, and C. Thomas Harris. Lithium Electrodeposition Dynamics in Aprotic Electrolyte Observed ¡i¿in Situ¡/i¿ ¡i¿via¡/i¿ Transmission Electron Microscopy. *ACS Nano*, 9(4):4379–4389, 4 2015.

[55] P. G. Balakrishnan, R. Ramesh, and T. Prem Kumar. Safety mechanisms in lithium-ion batteries. *Journal of Power Sources*, 155(2):401–414, 2006.

[56] Joy Chao and Zoey Warecki. ConTEMplating Atomic Resolution, 2019.

[57] Lord Rayleigh. XXXI. Investigations in Optics, witlt special reference to tl˜e Spectroscope. *The London, Edinburgh, and Dublin Philosophical Magazine and Journal of Science*, 8, 1879.

[58] R. F. Egerton. Choice of operating voltage for a transmission electron microscope. *Ultramicroscopy*, 145:85–93, 2014.

[59] Brent Fultz and James M. Howe. *Transmission Electron Microscopy and Diffractometry of Materials*. Springer, 2008.

[60] David B Williams and Barry C. Carter. *Transmission Electron Microscopes*. Springer, 2nd ed edition, 2009.

[61] G. McMullan, A. R. Faruqi, and R. Henderson. *Direct Electron Detectors*, volume 579. Elsevier Inc., 1 edition, 2016.

[62] Jeremy Ticey. *CARBON-SULFUR NANOCOMPOSITES FOR LITHIUM-SULFUR BATTERIES*. PhD thesis, University of Maryland, College Park, 2015.

[63] H. J. Leamy. Charge collection scanning electron microscopy. *Journal of Applied Physics*, 53(6), 1982.

[64] M. A. Falkenberg, H. Schuhmann, M. Seibt, and V. Radisch. Localization and preparation of recombination-active extended defects for transmission electron microscopy analysis. *Review of Scientific Instruments*, 81(6):063705, 6 2010.

[65] M Tchernycheva, V Neplokh, H Zhang, P Lavenus, L Rigutti, F Bayle, F H Julien, A Babichev, G Jacopin, L Largeau, R Ciechonski, G Vescovi, and O Kryliouk. Core-shell InGaN/GaN nanowire light emitting diodes analyzed by electron beam induced current microscopy and cathodoluminescence mapping. *Nanoscale*, 7:11692, 2015.

[66] Z. Z. Bandić, P. M. Bridger, E. C. Piquette, and T. C. McGill. The values of minority carrier diffusion lengths and lifetimes in GaN and their implications for bipolar devices. *Solid-State Electronics*, 44(2):221–228, 2000.

[67] D.E. Ioannou and C.A. Dimitriadis. A SEM-EBIC minority-carrier diffusion-length measurement technique. *IEEE Transactions on Electron Devices*, 29(3), 1982.

[68] D.E. Ioannou and C.A. Dimitriadis. A SEM-EBIC minority-carrier diffusion-length measurement technique. *IEEE Transactions on Electron Devices*, 29(3):445–450, 3 1982.

[69] F. Berz and H. K. Kuiken. Theory of life time measurements with the scanning electron microscope: Steady state. *Solid State Electronics*, 19:437–445, 1976.

[70] S. P. Shea, L. D. Partain, and P. J. Warter. Resolution Limits of the EBIC Technique in the Determination of Diffusion Lengths in Semiconductors. In *Scanning Electron Microscopy*, volume Vol 1, pages 435–444. Scanning Electron Microsc, Inc, AMF, 1978.

[71] Keung L Luke, Von Roos, and Li-Jen Cheng. Quantification of the effects of generation volume, surface recombination velocity, and diffusion length on the electron-beam-induced current and its derivative: Determination of diffusion lengths in the low micron and submicron ranges. *Journal of Applied Physics*, 57:1978, 1985.

[72] Keung L. Luke. Evaluation of diffusion length from a planar-collector-geometry electron-beam-induced current profile. *Journal of Applied Physics*, 80(10):5775–5785, 11 1996.

[73] Paul M. Haney, Heayoung P. Yoon, Benoit Gaury, and Nikolai B. Zhitenev. Depletion region surface effects in electron beam induced current measurements. *Journal of Applied Physics*, 120(9), 2016.

[74] J Boersma, Jje Indenkleef, and HK Kuiken. A diffusion problem in semiconductor technology. *Journal of Engineering Mathematics*, 18:315–333, 1984.

[75] Pierre Hovington, Dominique Drouin, and Raynald Gauvin. CASINO: A new Monte Carlo code in C language for electron beam interaction - Part I: Description of the program. *Scanning*, 19(1):1–14, 1997.

[76] Pierre Hovington, Dominique Drouin, Raynald Gauvin, David C. Joy, and Neal Evans. CASINO: A new Monte Carlo code in C language for electron beam interactions - Part III: Stopping power at low energies. *Scanning*, 19(1):29–35, 1997.

[77] Dominique Drouin, Pierre Hovington, and Raynald Gauvin. CASINO: A new Monte Carlo code in C language for electron beam interactions - Part II: Tabulated values of the mott cross section. *Scanning*, 19(1):20–28, 1997.

[78] H. Demers, N. Poirier-Demers, N. de Jonge, and D. Drouin. CASINO Monte Carlo Simulations of Scanning Transmission Electron Microscopy. *Microscopy and Microanalysis*, 16:1400–1401, 2010.

[79] DL Instruments LLC. Model 1211 Current Preamplifier.

[80] Dave Mitchell. Dave Mitchell's DigitalMicrograph™ Scripting Website.

[81] A. E. Grün. Lumineszenz-photometrische Messungen der Energieabsorption im Strahlungsfeld von Elektronenquellen Eindimensionaler Fall in Luft. *Zeitschrift fur Naturforschung - Section A Journal of Physical Sciences*, 12(2):89–95, 1957.

[82] T E Everhart and P H Hoff. Determination of Kilovolt Electron Energy Dissipation vs Penetration Distance in Solid Materials. *Journal of Applied Physics*, 42:5837, 1971.

[83] K Kanaya and S Okayama. Penetration and energy-loss theory of electrons in solid targets. *Journal of Physics D: Applied Physics*, 5(5), 1972.

[84] Mihir Parikh. Corrections to proximity effects in electron beam lithography. I. Theory. *Journal of Applied Physics*, 50:4371, 1979.

[85] Mihir Parikh and David F Kyser. Energy deposition functions in electron resist films on substrates. *Journal of Applied Physics*, 50:1104, 1979.

[86] C Donolato. A reciprocity theorem for charge collection. *Appl. Phys. Lett*, 46, 1985.

[87] C Donolato. An alternative proof of the generalized reciprocity theorem for charge collection. *J. Appl. Phys*, 66:4524, 1989.

[88] Eugene B Yakimov, Pavel S Vergeles, Alexander Y Polyakov, and Al . Diffusion length measurements in GaN. *Japanese Journal of Applied Physics*, 55, 2016.

[89] Melanie Nichterwitz and Thomas Unold. Numerical simulation of cross section electron-beam induced current in thin-film solar-cells for low and high injection conditions. *J. Appl. Phys*, 114:134504, 2013.

[90] W Van Roosbroeck. Injected Current Carrier Transport in a Semi-Infinite Semiconductor and the Determination of Lifetimes and Surface Recombination Velocities. *Journal of Applied Physics*, 26:380, 1955.

[91] H K Kuiken. Theory of Lifetime Measurements with the Scanning Electron Microscope: Transient Analysis. *Solid State Electronics*, 19:447–450, 1976.

[92] C J Wu and D B Wittry. Investigation of minority-carrier diffusion lengths by electron bombardment of Schottky barriers. *Journal of Applied Physics*, 49:2827, 1978.

[93] Paul G. Shewmon. *Diffusion in Solids.* 1963.

[94] C M Parish and P E Russell. On the use of Monte Carlo modeling in the mathematical analysis of scanning electron microscopy–electron beam induced current data. *Appl. Phys. Lett*, 89:192108, 2006.

[95] Oka Kurniawan and Vincent K.S. Ong. Choice of generation volume models for electron beam induced current computation. *IEEE Transactions on Electron Devices*, 56(5):1094–1099, 2009.

[96] C. Donolato. An Analytical Model of SEM and STEM Charge Collection Images of Dislocations in Thin Semiconductor Layers I. Minority Carrier Generation, Diffusion, and Collection. *Phys. Stat. Sol. (a)*, 65:649–658, 1981.

[97] Jean-Marc Bonard and Jean-Daniel Ganière. Quantitative analysis of electron-beam-induced current profiles across p–n junctions in GaAs/Al0.4Ga0.6As heterostructures. *Journal of Applied Physics*, 79(9):6987–6994, 5 1996.

[98] K. C. Collins, A. M. Armstrong, A. A. Allerman, G. Vizkelethy, S. B. Van Deusen, F. Léonard, and A. A. Talin. Proton irradiation effects on minority carrier diffusion length and defect introduction in homoepitaxial and heteroepitaxial n-GaN. *Journal of Applied Physics*, 122(23):235705, 12 2017.

[99] James B. Langworthy. Depletion Region Geometry Analysis Applied to Single Event Sensitivity. *IEEE Transactions on Nuclear Science*, 36(6):2427–2434, 1989.

[100] K. L. Brown and G. W. Tautfest. Faraday-cup monitors for high-energy electron beams. *Review of Scientific Instruments*, 27(9):696–702, 1956.

[101] David R.G. Mitchell and Mitchell J.B. Nancarrow. Probe current determination in analytical TEM/STEM and its application to the characterization of large area EDS detectors. *Microscopy Research and Technique*, 78(10):886–893, 2015.

[102] D C Look, D C Reynolds, J W Hemsky, J R Sizelove, R L Jones, and R J Molnar. Defect Donor and Acceptor in GaN. *Physical Review Letters*, 79(12), 1997.

[103] R. F. Egerton. Radiation damage to organic and inorganic specimens in the TEM, 4 2019.

[104] George C Messenger. A Two Level Model for Lifetime Reduction Processes in Neutron Irradiated Silicon and Germanium. *IEEE Transactions on Nuclear Science*, 14(6), 1967.

[105] Hayata Fukushima, Shigeyoshi Usami, Masaya Ogura, Yuto Ando, Atsushi Tanaka, Manato Deki, Maki Kushimoto, Shugo Nitta, Yoshio Honda, and Hiroshi Amano. Deeply and vertically etched butte structure of vertical GaN p-n diode with avalanche capability. *Japanese Jounal of Applied Physics*, 58, 2019.

[106] C. L. Progl, C. M. Parish, J. P. Vitarelli, and P. E. Russell. Analysis of v defects in GaN-based light emitting diodes by scanning transmission electron microscopy and electron beam induced current. *Applied Physics Letters*, 92(24):1–4, 2008.

[107] Myung Geun Han, Yimei Zhu, Katsuhiro Sasaki, Takeharu Kato, Craig A.J. Fisher, and Tsukasa Hirayama. Direct measurement of electron beam induced currents in p-type silicon. *Solid-State Electronics*, 54(8):777–780, 2010.

[108] M J Williamson, R M Tromp, P M Vereecken, R Hull, and F M Ross. Dynamic microscopy of nanoscale cluster growth at the solid-liquid interface. *Nature materials*, 2(8):532–6, 2003.

[109] F. M. Ross. Opportunities and challenges in liquid cell electron microscopy. *Science*, 350(6267):aaa9886, 12 2015.

[110] Paul M. Haney, Heayoung P. Yoon, Prakash Koirala, Robert W. Collins, and Nikolai B. Zhitenev. Electron beam induced current in the high injection regime. *Nanotechnology*, 26(29), 2015.

[111] E. B. Yakimov, A. Y. Polyakov, N. B. Smirnov, I. V. Shchemerov, Jiancheng Yang, F. Ren, Gwangseok Yang, Jihyun Kim, and S. J. Pearton. Diffusion length of non-equilibrium minority charge carriers in β-Ga2O3 measured by electron beam induced current. *Journal of Applied Physics*, 123(18), 2018.

[112] Subrahmanyam Goriparti, Zoey Warecki, Katharine L. Harrison, Andrew Leenheer, John Cumings, and Katherine L. Jungjohann. Liquid-Cell TEM Observations of Sn Lithiation reactions: A Temperature Case Study. *Microscopy and Microanalysis*, 23(S1):1966–1967, 2017.